Università Politecnica delle Marche
Scuola di Dottorato di Ricerca in Scienze dell'Ingegneria
Corso di Dottorato in Ingegneria Civile, Ambientale, Edile e Architettura

---

# Sediment transport processes in harbour settings: investigation of the effects induced by natural and anthropogenic forcing

Ph.D. Dissertation of:
**Carola Colangeli**

Supervisor:
**Prof. Maurizio Brocchini**

Ph.D. Course coordinator:
**Prof. Francesco Fatone**

XXXVI edition - New series

Università Politecnica delle Marche
Dipartimento di Ingegneria Civile, Edile e Architettura (DICEA)
Via Brecce Bianche - 60131 - Ancona, Italy

# Acknowledgements

First of all, I would like to express my gratitude to my supervisor, Prof. Brocchini, who assisted and guided me throughout this project. I also want to thank the rest of my colleagues and professors of the Hydraulic Department for welcoming me in their group and for the and the useful advice provided along this study. A special mention goes to Agnese for her patience and help in finalizing the first part of this thesis.

I would like to thank the Italian Navy for giving me this wonderful opportunity. In particular, I want to thank my superiors, C.F. Patrono and C.F. Pignotti, who supported me in all the aspects of this journey and C.F. Di Michele for giving me all the time I needed to complete this work.

My gratitude goes to my Prof. Dimas, my supervisor during the internship in Greece. I want to express all my gratitude to my collague George for his unwavering support and belief in me.

I wish to acknowledge Prof. Shi, for providing a huge improvement in this work, but also for your kindness during the days spent at the University of Delaware.

Lastly, I would also like to thank my family and Gianluigi, whom without this would have not been possible.

I am grateful to all of you.

# Abstract

In this work an investigation of the sediment transport processes induced by natural and anthropogenic forcings is presented.

Through a numerical modelling approach, the contribution to the sediment transport phenomena due to natural meteomarine forcing first and then caused by ship propellers has been evaluated respectively using the Delft3D suite and the FUNWAVE model. Firstly, a parametric and scenarios-based analysis has been provided to gain knowledge on the hydro-morphodynamics and the possible siltation induced by extreme meteo-marine conditions (100-year return period) and freshwater discharges by rivers debouching into the La Spezia military harbour (Liguria, Italy). To do this, numerical simulations of three different scenarios have been performed, taking into account, respectively, the contribution of the waves and the tide (first scenario), the river discharges and the tide (second scenario) and the superposition of all forcings, i.e. waves, tide and river discharges (third scenario). All scenarios have been performed using a uniform wind field from the typical directions blowing on the La Spezia Gulf (north-northeast and south-southeast winds). Results have revealed that, in this peculiar configuration, sheltered by the presence of the islands and the outer main breakwater, the hydro-morphodynamics circulation is strongly influenced by the wind and river discharges. In fact, the wind direction determines the sense of rotation of the circulation cell inside the basin, modified by the freshwater streams. The latter ones, according to the wind direction, contribute to enhance the existing flow field or to generate an additional minor eddy interacting with the main cell. The morphodynamics, instead, is largely controlled by the river discharges, fundamental in supplying and resuspending sediments into the harbour, while the sediment transport is mainly due to the wind forcing. However, both sedimentation and erosion rates are low, confirming that no significant siltation can occur due to natural forcings over the time scale of a storm.

Therefore, much attention has been given to anthropogenic contributions, in particular to the impact of ship propellers. For this purpose, the depth-averaged open source Boussinesq FUNWAVE-TVD model has been used and extended to describe the ship-propeller-induced sediment transport. The propeller-induced effect on the sediment transport has been implemented as an additional velocity field on the seabed, resulting in a supplementary contribution to the shear velocity and the bed shear stress, consequently used to compute the suspended load-induced and the bedload-induced morphological changes. Numerical results have confirmed the capability of the new code to qualitatively describe complex morphodynamic patterns, in good agreement with the literature. Precisely, significant similarities have been found in the development of the scour process and in the longitudinal profile, characterized by the presence of two scour holes, a small one directly beneath the propeller and the primary scour hole behind the propeller, followed by a deposition mound downstream. However, some modifications need to be made for the overall improvement of the code, like the addition of the propeller wash momentum flux in the hydrodynamic computation and the coupling of the hydro-morphodynamics. Moreover, further numerical and experimental tests will be fundamental for a proper validation of the numerical model, which might therefore provide a useful tool in predicting scour processes, crucial issues in the design and management of ports, navigation channels and maritime structures.

# Contents

# List of symbols

| | |
|---|---|
| $\alpha_1, \alpha_2, \beta$ | Shape coefficients of the ship |
| $\bar{c}$ | Non-dimensional depth-averaged concentration |
| $\bar{u_2}$ | Depth-averaged $O(\mu^2)$ contribution to the depth-averaged velocity |
| $\Delta$ | Submerged specific gravity |
| $\Delta_r$ | Wave-induced ripple height |
| $\epsilon_s$ | Sediment eddy diffusivity |
| $\eta$ | Water level with respect to the mean sea level |
| $\nu$ | Kinematic viscosity of water |
| $\nu_H$ | Horizontal eddy viscosity |
| $\phi$ | Repose angle of the sediment |
| $\rho_s$ | Sediment density |
| $\rho_w$ | Water density |
| $\tau_p$ | Bed shear stress propeller-induced |
| $\tau_{cr,d}$ | Critical deposition shear stress |
| $\tau_{cr,e}$ | Critical erosion shear stress |
| $\tau_{cr}$ | Critical shear stress for bedload |
| $\tau_{wc}$ | Maximum bed shear stress due to current and waves |
| $\theta_p$ | Wave peak direction |
| $\theta_{cr}$ | Shields parameter |
| $a$ | Van Rijn reference height |
| $A_0$ | Propeller disk area |
| $A_e$ | Propeller expanded area |
| $A_p$ | Propeller area |
| $BAR$ | Blade Area Ratio |
| $C$ | Chézy coefficient |
| $c$ | Depth-averaged concentration |
| $C_f$ | Friction coefficient |
| $c_p$ | Propeller coefficient |
| $C_t$ | Thrust coefficient |

| | |
|---|---|
| $c_b$ | Average sediment concentration in the near bottom computational layer |
| $c_{eq}$ | Equilibrium depth-averaged concentration |
| $CFL$ | Courant-Friedrichs-Levy number |
| $D$ | Deposition flux |
| $d^*$ | Non-dimensional grain size |
| $D_h$ | Propeller hub diameter |
| $D_p$ | Propeller diameter |
| $dZ_b$ | Time-averaged depth changes |
| $E$ | Erosion flux |
| $E_0$ | Efflux coefficient |
| $F_0$ | Densimetric Froude number |
| $g$ | Gravity acceleration |
| $H$ | Total water depth |
| $h$ | Water depth |
| $H_s$ | Significant wave height |
| $J_a$ | Advance coefficient |
| $k_s$ | Nikuradse roughness coefficient |
| $L$ | Lenght of the ship |
| $M$ | Erosion parameter |
| $M_e$ | Excess sediment mobility number |
| $M_s$ | Sediment mobility number due to waves and currents |
| $n$ | Revolution speed |
| $n_M$ | Manning coefficient |
| $n_s$ | Sediment porosity |
| $P$ | Draught of the ship |
| $q_b$ | Bedload transport |
| $R$ | Riemann variable |
| $R_h$ | Hub radius |
| $R_p$ | Propeller radius |
| $Re$ | Reynolds number of the propeller flow |
| $S$ | Source/sink term |
| $s$ | Density ratio |
| $S(\tau_{wc}, \tau_{cr,d})$ | Step function for deposition |
| $S(\tau_{wc}, \tau_{cr,e})$ | Step function for erosion |
| $S_b$ | Magnitude of the bedload transport |
| $t$ | Time |

$T_p$ Wave peak period

$U_b$ Maximum efflux velocity on the seabed

$U_c$ Depth-averaged total velocity

$u_c$ Friction velocity

$U_n$ Normal-to-boundary velocity component

$U_p$ Propeller-induced velocity on the seabed

$u_{*cp}$ Friction velocity propeller-induced

$u_\alpha$ Velocity at the reference level

$V_0$ Efflux velocity

$v_a$ Advance speed

$W$ Beam of the ship

$w_s$ Hindered settling velocity

$(M_x, M_y)$ External source/sink of momentum in x- and y-directions

$(u, v)$ Flow velocity components in x- and y-directions

$(x, y, z)$ Cartesian coordinates

# List of Figures

# List of Tables

# Chapter 1

# Introduction

## 1.1 Context of the Thesis

The present study, prompted by the needs of the Italian Navy, was motivated by the primary wish to understand whether the sediment transport evolving at the inlets and inside the semi-enclosed La Spezia Arsenale military basin in La Spezia (Italy), mainly due to natural forcings, could lead to harbour siltation. In this perspective, this work aims at identifying which are the principle mechanisms dominating the sediment transport processes in order to provide support for the definition of the measures that might be implemented to control this phenomenon and mitigate its impacts. Harbour siltation, in fact, could compromise the port operativity, which implies for a military harbour like that in La Spezia, undermining Italy's maritime defense and security system.

## 1.2 Objectives and Layout of the Thesis

The main aim of this work is the investigation of the sediment transport processes and the occurrence of the siltation evolving in harbour settings due to impulsive forcings. Such phenomena can be induced by multiple factors, both natural and anthropogenic, each of which has been investigated numerically.

In particular, for the first part of the Thesis, the principle purpose is an in-depth analysis of all the extreme meteomarine forcings, i.e. waves, tide, rivers' discharges and wind, acting on the area of interest, over a time scale of a storm. Through a numerical approach, it has been inspected the contribution given by each forcing in the hydro-morphodynamics. Similarly, for the second part of the Thesis, the attention has been drawn to the anthropogenic factors inducing sediment transport, in particular to ships' propellers.

Among all the anthropogenic causes, the influence of the ship propellers plays an important role and might have severe implications for the navigation and the maintenance of port infrastructure. This work focuses on providing a useful and user-friendly tool to investigate this effect, by presenting, although at an early stage, a new numerical model of the propeller scour.

Both forcings, natural and anthropogenic, have been investigated as characterized by a short duration and a limited spatial distribution. The extreme actions used to force the model, waves and rivers' discharges associated to a 100-years return period, are representive of a storm, occuring in a very restricted area, i.e. the La Spezia military harbour. Likewise, the effect of the ship propeller is exerted during the brief passage of the ship and it is stricly limited to the areas close to the vessel.

The study area is the military harbour in La Spezia, called as Arsenale, pivotal harbour of the Italian Navy. This is a peculiar site, being a semi-enclosed basin in a microtidal setting, sheltered by an outer large breakwater and characterized by the presence of two freshwater streams, the Lagora River (LR hereinafter) and the Caporacca River (CR hereinafter), respectively debouching close and directly into the Arsenale. Such configuration has made this study particularly interesting for the

sediment transport processes, since it could not be properly classified in a specific type of environment, with reference to those proposed by [75].

Both the unusual site and the phenomena to be studied have required many data, not always easy to collect, also considering that the study area is protected by military secrecy. Therefore, data related to the Arsenale (bathymetric surveys, geometry, bed stratigraphy) were provided by the Navy, in particular by the Istituto Idrografico della Marina and the Direzione del Genio Militare per la Marina di La Spezia. Other data related to the forcing terms, instead, were provided by the Municipality of La Spezia and Liguria Region (as the rivers' discharges), the Italian institute for Environmental Protection and Research (ISPRA for the tidal elevation and the wind field), the Copernicus Marine Service (for the waves).

This thesis is structured into seven chapters as follows:

Chapter 1 (*Introduction*) defines the principal aspects and provides a literature review of the processes investigated, with reference to the novelties introduced by this work.

Chapter 2 (*The study area*) describes the hydrodynamic and morphodynamic characteristics of the observed area.

Chapter 3 (*Study of the sediment transport in the Arsenale*) relates the analysis of the sediment transport processes evolving within the Arsenale. Section 3.1.1 concerns the Delf3D numerical solver, while Section 3.1.4 clarifies the numerical simulations carried out. In Section 3.2 results are presented.

Chapter 4 (*Study of the ship's propeller sediment transport*) focuses on the sediment transport induced by the ships' propeller. Section 4.2.1.1 provides a general description of the sediment transport and ship wakes modules in FUNWAVE-TVD, while Section 4.2.2 focuses on the innovations introduced in the solver to implement the ship propeller induced sediment transport. Section 4.3 gives an overview of the numerical runs assessed. Section 4.4 presents the results obtained.

In Chapters 5 (*Discussion on the sediment transport induced by natural forcings*) and 6 (*Discussion on the sediment transport induced by ship propellers*) a discussion of the results is given. Firstly, in Chapter 5 a comprehensive investigation of the sediment transport mechanisms in the Arsenale is presented, also comparing the modelled results to the field data available. Secondly, Chapter 6 provides a critical analysis of the numerical runs results, with comparisons to similar examples in the literature, highlighting the pros and cons of the ship propeller implementation in the FUNWAVE-TVD model.

Finally, Chapter 7 (*Conclusions*) summarizes the main findings of both the topics analyzed in the present work.

## 1.3 Sediment transport in harbours and harbour siltation

In the last decades, ports have played a significant role in the worldwide economic system, being crucial nodes for the international trade and in the transportation network. Therefore, the correct management and maintenance, with constant dredging campaigns, of harbours are vital for the modern global economy. These aspects in harbours facilities can be largely influenced by sedimentation processes, for which detailed knowledge is essential [68], in order to guarantee port functionality and safe navigation. The filling of a harbour entrance due to fine sediment is usually referred to as harbour siltation, a problem that predominantly affects the fundamental function of the facility, which is to create a sheltered environment [65]. The sediment processes can influence the depth of both navigation channels and harbour entrances [65]. In fact, sediment resuspended from the bed by the action of waves and currents can be transported into the harbours, where the transport capacity rapidly reduces due to a decrease in wave height; this causes local deposition and siltation. The siltation is mainly due to net sediment transport through the entrance and into the harbour. Hence, many studies were conducted to investigate all the possible processes which can induce the water exchange between the harbour and the open sea, responsible to

move the sediments within the basin area.

In accordance with the literature [65, 75], the mechanisms through which the fluid can enter and leave a basin are essentially generated by: (1) horizontal entrainment; (2) tidal filling and emptying; and (3) density currents; these are better described in the following paragraphs. The horizontal entrainment is the main mechanism that occurs in harbours placed along water streams, like rivers and channels. It is caused by the horizontal shear between the river flow and the basin. The river flow separates at the upstream corner of the basin, generating an eddy between the harbour basin and the river itself. The strength of the turbulence is governed by the geometry of the upstream corner and the stagnation behaviour at the downstream corner. The amount of exchanged water depends on the river velocity, the cross-sectional area of the harbour entrance, and the angle between the river and the harbour entrance [5, 38]. As far as the tidal filling and emptying is concerned, the water exchange flow rate caused by the tidal action is such that the water can be effectively advected into the basin entrance at rising tide (tidal filling) and advected outside the basin at falling tide, leading to tidal emptying. In tide-dominated environments, these mechanisms also trigger the intake and removal of sediment [10]. Regarding the third mechanism, density currents can be generated by either salinity or temperature gradients and can cause significant flow exchange. Furthermore, Winterwerp stated that strong density currents can also be induced by low suspended sediment concentration. Such currents increase the sediment fluxes into the harbours and significantly augment the trapping efficiency within them. In addition to the above-mentioned mechanisms, other authors e.g. [12, 49], noted that in particular configurations, like microtidal shallow basins, the interaction of tidal currents with the wind- and wave-induced currents could make an important contribution to erosion processes. Obviously, all these mechanisms can act simultaneously or one of them can dominate the others, depending on the forcings and the environments in which the basins are placed. In this regard, a valuable classification of the different water exchange mechanisms that can occur in harbours was provided by Winterwerp [75]. With reference to the processes, Winterwerp identified those that could take place in stagnant water and riverine, tidal, and estuarine systems. This distinction is useful for a preliminary prediction of the main processes responsible for the water exchanges in a specific location.

More detailed investigations of the flow patterns generated by such mechanisms, which evolve both inside and outside of the harbours, can be conducted by means of both laboratory (scaled-down) and numerical models. On the one hand, laboratory tests are an appropriate when analysing the turbulence at the entrance of a basin, but on the other hand, they are extremely expensive and useful to provide easily qualitatively informations in terms of siltation, mainly due to cohesive sediment scaling issues. Therefore, numerical modelling (e.g., MIKE21, Delft3D) has been extensively used in recent years for the investigation of hydro-morphodynamical processes, thanks to the reasonable computational time and effort required for studying wide and complex areas under multiple scenarios. Many numerical models considering port areas and sedimentation issues have been developed, due to the relevance of such infrastructures in the trading system and the costs associated with their maintenance through dredging operations. Some interesting examples of peculiar sites are reported here. The numerical modelling for the Marine Wharf in the Saint John Harbour, proposed by Leys [40], is characterized by a very large tidal range and strong river discharge. Also, the study conducted by Carniello et al. [10] examined the morphodynamics induced by the combined action of the tidal currents and wind waves in the shallow microtidal basin of the Venice Lagoon. An interesting numerical modelling set up by means of Delft3D was presented by Lojek et al. [41]; it provided a useful study of the design of a harbour, showing the impacts of some modifications in the layout of the harbour itself on the sedimentation rates. A study performed with the MIKE package on the Nowshahr port in the Caspian Sea [44] confirmed the capabilities of numerical modelling in capturing the hydro-morphodynamic mechanisms; the study identified the fact that wind-induced circulation was responsible for the carrying of sediments at the port entrance. As for the works reported before, considering the particular configuration of the Arsenale and all the forcings involved, we had chosen a

numerical-modelling approach, described in detail in Chapter 3.

## 1.4 Ship-forced sediment transport: the propeller jet flow effects

In addition to the natural forcings, there are anthropogenic reasons for the harbour siltation. For example, dredging campaigns are required for the maintenance of harbours, ports and navigable waterways to ensure their depth and accessibility, but can also alter sediment transport and deposition patterns. However, dredging, appropriately planned and carefully managed in consideration of its environmental impact, is a valuable tool for managing sedimentation in water bodies. Another cause of the human-induced harbour siltation can be recognized in ship propellers.

In harbor environments and navigation channels, where the ship-to-bed clearance is minimal, it is important to focus on the effects caused by ship's propeller jet, the traditional propulsion system for ships. The ship rotating propeller, generally characterized by three or more blades, provides a thrust drawing in water, accelerating and discharging it downstream, resulting in a jet or a wash, this causing multiple effects. First, the jet can erode the seabed, generating significant bed scour. Secondly, it enhances the resuspension and transport of the sediments on the seabed, which can accumulate and eventually reduce the required draught for the navigation and affect the port functionality. In addition, if scouring occurs close to marine structures, it can also affect and compromise their stability. Therefore, for a proper design of harbours it is necessary to evaluate the velocities at the bed induced by ship propellers, especially in the last years when the evolution of the ships' size has required the use of more powerful propulsion systems, leading to potential more severe damages.

A large number of studies has been conducted to estimate the velocity profile within the jet, this representing the initial step for the prediction of the propeller-induced bed shear stress and scour. The prediction of velocity field is essentially based on the magnitude of the efflux velocity. The efflux velocity is the maximum axial velocity at the face of the propeller, from which it is possible to evaluate the maximum velocity at different sections. Therefore, on the basis of experimental works, several equations have been proposed to properly define the velocity distribution within the wash. A comprehensive review of all the main formulations is provided by [36].

Regarding the scour prediction, at present, simple equations, based on the definition of the efflux velocity, are available and used in practical engineering case studies. However, for more accurate analyses on the seabed sediment dynamic processes, also over different timescales, numerical modeling represents an useful tool for port authorities and operators to garantuee the operational activities and the correct management of the port. In the following, some examples are listed. An existing example is that proposed by Wang et al. [73]. The numerical approach proposed in his work, though useful, is limited by the fact that the mass of the propeller wash–induced, resuspended sediments at a specific area is computed manually using empirical expressions and ship traffic information. Moreover, the contribution of the wash–induced, resuspended sediments is added as a source term into an uncoupled model simulation to predict the far-field movements of the resuspended sediments in the water, without modifying neither the hydrodynamics (e.g., flow velocities) nor the morphological evolution of the seabed. (e.g., bed scour). In addition, this method might be extremely difficult to apply in wide areas where the ship traffic is continuous and massive. Other numerical methods, like those proposed by the US Army Engineer Research and Development Center [23], [29], are capable to simulate a coupled representation of both propeller wash effects and sediment transport processes, including the formulation of ship-generated bed shear stress [47] into the computational codes of sediment transport. In the work of Hammack et al. [29], both the effects induced by the bow and by the propeller on the bed shear stress are considered. Results clearly underlined the primary role of the propeller, confirming the necessity to conduct deeper analyses on this contribution. Albeit the propeller jet sediment transport processes are coupled, also these modeling efforts are still incomplete since

they do not take into account the impacts of propeller wash–induced momentum in the hydrodynamic computation. As a result, the movements of resuspended sediments in the water column were simulated based only on ambient currents, which would show less advection and dispersion of the resuspended sediments than occurs with the actual propeller wash–induced flow field.

Recently, due to the increasing computational efficiency of computers, Computational Fluid Dynamics (CFD) is gaining more traction for studying complex fluid dynamics problems. However, the application of CFD models is on a case-by-case basis and it is recommended to choose the appropriate solver according to the problem to investigate [46]. Regarging the scour induced by the propeller wash, the CFD Fluent package and OpenFOAM have been recently applied by researchers, the former for determining the velocities and the turbulence within the wash [37], the latter for predicting the scour depth and extent [61]. In both cases, CFD solvers have provided results in good agreement with the experimental tests with reduced costs in terms of computational time. Another example of the use of the CFD is has been proposed by Guarnieri et al. [25] to study the seabed impact of marine traffic in the port of Genoa has combining the circulation model with the sediment transport model, assessed both by MIKE 3 FM. This study analysed the influence of a single vessel from each dock of the port, then weighted according to the annual number of passages. By the superposition of the effects of single vessels, the annual cumulative erosion/deposition map has been obtained and compared with bathymetric surveys for the same period, showing accurate results.

It is worth mentioning that all the numerical models mentioned before are not freely available. Therefore, the aim of this work is to lay the foundations to implement a new module in the open-source FUNWAVE-TVD package, dedicated to predict the propeller-induced scour. As part of the FUNWAVE Boussinesq model, the propeller-module will enable investigators to conduct an in-depth analysis of all the hydro-morphodynamic phenomena occurring in harbour settings. Then, it will be possible to account for the waves and the ships interactions, simulate multiple vessels and evaluate their effects on the sediment transport processes and the morphological evolution of the seabed, with accuracy and acceptable computational costs.

# Chapter 2

# The study area

## 2.1 The field site: the Arsenale

The La Spezia harbour (see Figure 2.1), located in the gulf of the same name within the Ligurian Sea, is one of the most important ports in northern Italy. Sheltered by a very large, main breakwater, it hosts a shipping area and the "Arsenale" military harbour of the Italian Navy in the northwest and northeast regions of the harbour, respectively. The Arsenale covers an area of 2 $km^2$, extending 1.5 km in the northern direction and 1.2 km in the eastern direction. It is delimited by breakwaters and connected to the rest of the gulf through two entrances. The southern main entrance (yellow circle in Figure 2.1) is characterized by a water depth of about 12 m and a width of around 120 m, and it is reserved for military vessels. The northeastern mouth (magenta circle in Figure 2.1), which is about 60 m wide and 6 m deep, connects the Arsenale to the shipping area. Here, the passing by of ships is not allowed. The average water depth inside the Arsenale is about 12 m. The La Spezia gulf is located in a microtidal environment, characterized by tidal ranges smaller than 1 m in winter and even lower ranges, about 0.30–0.40 m, in summer and spring (https://www.mareografico.it).

Figure 2.2a and Figure 2.2b show respectively the wave (right panel) and wind roses (left panel) for the study site for last year (2022). The prevailing wind, i.e., the most frequent one, is from the NNE, while the dominant wind, which is the one with the highest speed, comes from the SSE. The yearly and directional average wind velocity is 3.02 m/s. The wave climate over the gulf is characterized by waves from the SW, forced by the Libeccio wind, which is prevailing and dominant. The mean annual significant height is 0.68 m, while the mean annual peak period is 6.2 s. In situ samplings showed that the bed stratigraphy in the La Spezia area is predominantly composed of silt and sand [56]. Inside the basin, the sediment mixture consists mainly of cohesive material, mainly silt and clay (about 42% and 28%, respectively), with a lower amount of sand (nearly 30%). The harbour is characterized by the presence of two main freshwater streams, the Lagora and the Caporacca (hereinafter, LR and CR, respectively). The hydrographic basin areas are, respectively, 17 $km^2$ for the LR and 2.95 $km^2$ for the CR. The last stretch of the LR (green line in 2.1) flows between the Arsenale and the shipping area before debouching into the sea in the area of the northeastern mouth. Here, the LR width and the depth are, respectively, around 35 m and 8 m. The CR is buried in its final reach, which is around 12 m wide and around 3.5 m deep, and flows directly into the Arsenale (cyan line in Figure 2.1). The water discharges associated with the return periods of 50, 200, and 500 years are, respectively, 171.02 $m^3/s$, 247.41 $m^3/s$, and 297.98 $m^3/s$ for the LR, while they are 52.78 $m^3/s$, 76.36 $m^3/s$, and 91.88 $m^3/s$ for the CR [55]. The sediment concentrations were computed from the annual average sediment load and the annual average water discharge. The annual average sediment loads are equal to 4022 kg $yr^{-1}$ and 1200 kg $yr^{-1}$, respectively, for the LR and CR, while the annual average water discharges are 0.2476 $m^3/s$ for the LR and 0.038 $m^3/s$ for the CR [55].

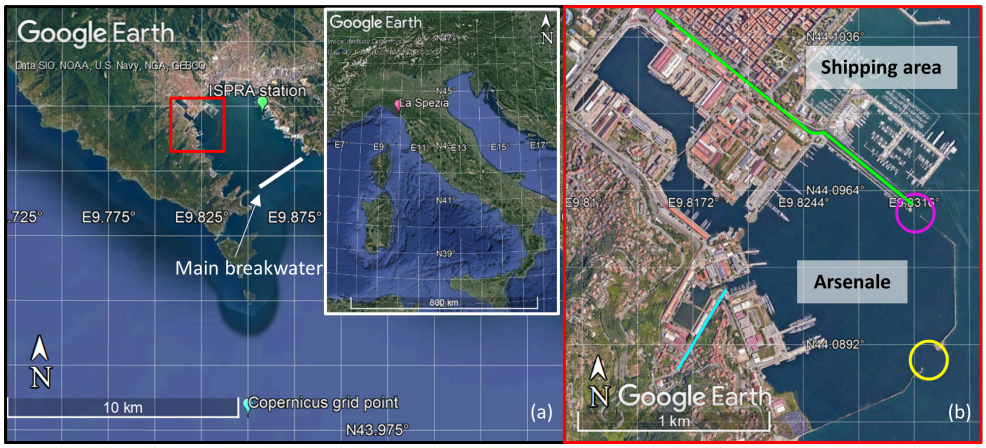


Figure 2.1: (a) La Spezia gulf with the following indicated: the Copernicus grid point for wave data (cyan pin); the ISPRA station for tide and wind data (green pin); the Arsenale and the shipping area (red square) and the main breakwater. The box in the top-right corner shows the location of La Spezia in Italy. (b) Close-up view of the Arsenale and the shipping area, with the yellow and magenta circles identifying the southern and northeastern entrances, respectively, and the green and cyan lines representing the Lagora and Caporacca rivers.

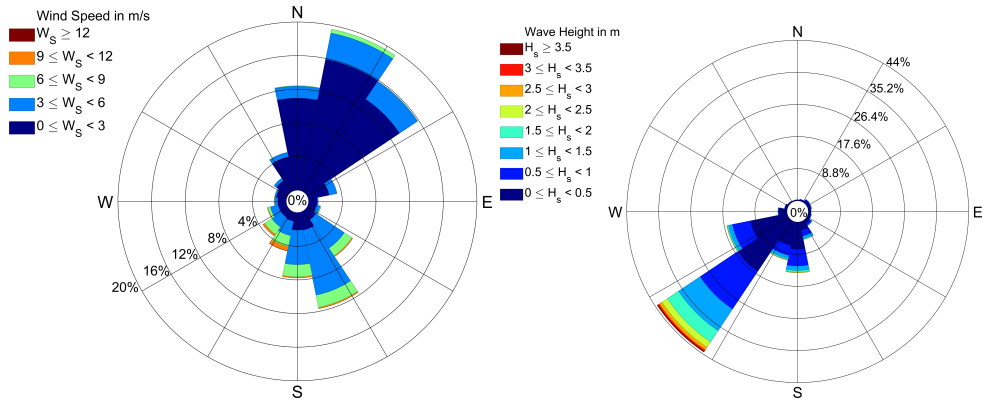


Figure 2.2: Wave rose for the significant wave height (left panel) and wind rose (right panel)

## 2.2 Data collection

For the purposes of this study, an extreme value analysis was conducted to define the wave and wind parameters associated with a 100-year return period. The wave data, i.e., significant wave height, peak period, and direction, covering a 26-year-long period from 1993 to 2019, were provided by the multiyear wave product of the Mediterranean Sea Waves forecasting system [35], downloadable from the Copernicus Marine Service. The dataset spatial and temporal resolutions are, respectively, 1/24° and 1 h. We extracted data for the location at the coordinates 43.98° N, 9.85° E, as shown in Figure 2.1. Both the seawater level and the wind speed and direction, with a temporal resolution of 10 min, were derived from the ISPRA station of La Spezia, managed by the Rete Mareografica Nazionale (https://www.mareografico.it), whose location is shown in Figure 2.1. The data related to the bed stratigraphy were obtained from a geophysical survey, commissioned by the "Direzione del Genio Militare per la Marina di La Spezia" [56] and the studies of the Molo Ravano by DHI Italia [17]. As reported above, the sediment load data and the CR and LR flood discharges, associated with different return periods, were derived from the analyses by Hydrodata [55], while the annual average water discharges were downloaded from the online geoportal of Liguria Region (https://geoportal.regione.liguria.it/catalogo/mappe.html).

# Chapter 3

# Study of the sediment transport in the Arsenale

## 3.1 Numerical simulations

Several numerical simulations, which provided the support for a scenario-based parametric analysis, were run to properly define the forcing affecting the hydrodynamic and the sediment transport inside the Arsenale when stressed with extreme conditions. For this case study, in the persepective of defining the dominant mechanisms of the sediment transport processes in the Arsenale, 100-years return period forcings were implemented in the numerical simulations. It is worth mentioning that this study should not regarded as a design analysis for which more frequent events, associated to shorter return periods, should be referred to, nor it should be understood to focus on the definition of local or mean annual siltation rate of the basin. Instead, the overarching approach aims at representing a comprehensive investigation of the overall hydro-morphodynamics of the area.

First, the offshore wave propagation (Copernicus point in Figure 2.1) toward the military harbour was computed using the widely used wave-resolving, Boussinesq-type model FUNWAVE [58] to appropriately model the interactions of the waves with obstacles, i.e., the main breakwater (see Figure 2.1).

The results obtained from FUNWAVE, in terms of water level and velocity time series, were used as one of the forcings of a more refined Delft3D simulation. Delft3D was chosen because, unlike FUNWAVE, it is flexible enough to allow for the inclusion of a number of point sources, used here to describe riverine inputs (e.g., the LR and CR freshwater discharges). Tide and wind were also accounted for among the forcing actions, and three different scenarios were simulated to understand the role of the waves (W), tide (T), rivers' discharges (R), and winds on the hydrodynamics and sediment transport inside the Arsenale.

### 3.1.1 Delft3D numerical solver

Delft3D, developed by WL|Delft Hydraulics, is a modeling suite, widely used for simulations in coastal, riverine and estuarine environments. The Delft3D package consists of several integrated modules that allow for the simulation of hydrodynamic flow (under the shallow water assumption), computation of the transport of constituents (e.g., salinity and heat), short wave generation and propagation, sediment transport and morphology and the modeling of ecological processes and water quality parameters [39]. The FLOW module is a multi-dimensional hydrodynamic simulation programme that computes unsteady flows resulting from tidal and meteorological forcing on a curvilinear, boundary fitted grid or spherical coordinates. The calculation of the transport of water-borne constituents and sediment and the computation of morphological changes are performed simultaneously within the FLOW module, this bringing many advantages. For example, i) sediment transport and morphological simulations are simpler to perform and do not require a large communication data file to share results between

different modules, and ii) changes in bathymetry can be immediately fed back to the hydrodynamic calculations. The coupled sediment module allows one to compute the morphological changes due to the transport, erosion, and deposition of both cohesive and non-cohesive sediments, this making it suitable for investigating sedimentation and erosion problems in complex hydrodynamic situations.

The Delft3D-FLOW module is suitable for predicting the flow in shallow seas, coastal areas, estuaries, lagoons, rivers, and lakes. It solves the unsteady shallow-water equations in two (depth-averaged) or three dimensions. The horizontal momentum equations, the continuity equation, the transport equation, and a turbulence closure model form the system of equations. The vertical momentum equation is reduced to the hydrostatic pressure relation as vertical accelerations are assumed to be small compared to gravitational acceleration and are neglected. For depth-averaged simulations, such as those performed in this work, the continuity and horizontal momentum equations are [39]:

$$\frac{\partial \eta}{\partial t} + \frac{\partial hu}{\partial x} + \frac{\partial hv}{\partial y} = S \tag{3.1}$$

$$\frac{\partial u}{\partial t} + u\frac{\partial u}{\partial x} + v\frac{\partial u}{\partial y} = -g\frac{\partial \eta}{\partial x} + M_x + g\frac{u\sqrt{u^2+v^2}}{C_u^2 h} + \nu_H\left(\frac{\partial^2 u}{\partial x^2} + \frac{\partial^2 u}{\partial y^2}\right) \tag{3.2}$$

$$\frac{\partial v}{\partial t} + u\frac{\partial v}{\partial x} + v\frac{\partial v}{\partial y} = -g\frac{\partial \eta}{\partial y} + M_y + g\frac{v\sqrt{u^2+v^2}}{C_v^2 h} + \nu_H\left(\frac{\partial^2 v}{\partial x^2} + \frac{\partial^2 v}{\partial y^2}\right) \tag{3.3}$$

where $\eta$ is the water level with respect to the mean sea level, $t$ is time, $h$ is the water depth, $u$ and $v$ are the flow velocity components in the $x$ and $y$ directions, respectively, $S$ represents the source/sink of water mass and $g$ is gravity acceleration. $C_u^2$ and $C_v^2$ are the Chézy roughness coefficients in the $x$ and $y$ directions, respectively, and are related with the Manning coefficient $n_M$ using $C = \frac{h^{1/6}}{n_M}$. $M_x$ and $M_y$ represent the external sources or sink of momentum, whereas the last term in equations 3.2 and 3.3 represents the horizontal Reynold's stresses, in which $\epsilon_H$ is the horizontal eddy viscosity defined by the user. For more details on such equations, the reader is referred to [15, 39].

Regarding the sediment transport and morphology, Delft3D computes both bedload and suspended load transport of non-cohesive sediments and suspended load of cohesive sediments. It allows to define different sediment fractions, classified as *mud*, used for the cohesive suspended load transport, *sand*, for which both non-cohesive bedload and suspended load transport are evaluated, and *bedload*, included in the non-cohesive bedload computation only or in the total load transport. Therefore, the advection-diffusion equation is not solved for the *bedload* fraction. Several formulations are proposed for the bed-exchange and settling velocity of these different types of sediment, as better described in [15].

For the suspended-sediment transport, the 2D advection-diffusion equation is used:

$$\frac{\partial Hc}{\partial t} + \frac{\partial Huc}{\partial x} + \frac{\partial Hvc}{\partial y} = H\left[\frac{\partial}{\partial x}(\epsilon_s\frac{\partial c}{\partial x}) + \frac{\partial}{\partial y}(\epsilon_s\frac{\partial c}{\partial y})\right] + HS \tag{3.4}$$

where $c$ is the sediment concentration, $\epsilon_s$ is the sediment eddy diffusivity and $S$ is the source/sink term modeling the exchange between the water column and the bed and $H$ is the total water depth. The local flow velocities and eddy diffusivity are derived from the results of the hydrodynamic computations (for more details, the reader is referred to [15]).

The erosion ($E$) and deposition ($D$) fluxes for the cohesive sediment are calculated with the Partheniades-Krone formulations [51]:

$$E = MS(\tau_{wc}, \tau_{cr,e}) \tag{3.5}$$

$$D = w_s c_b S(\tau_{wc}, \tau_{cr,d}) \tag{3.6}$$

where $M$ is the erosion parameter, defined by the user. $S(\tau_{wc}, \tau_{cr,e})$ and $S(\tau_{wc}, \tau_{cr,d})$ are the erosion/deposition step functions, while $w_s$ is the hindered settling velocity

and $c_b$ is the average sediment concentration in the near bottom computational layer (or the average sediment concentration in case of a uniformly mixed bed layer).
The step functions are defined as follows:

$$S(\tau_{wc}, \tau_{cr,e}) = \begin{cases} (\frac{\tau_{cw}}{\tau_{cr,e}} - 1), & \text{when } \tau_{cw} > \tau_{cr,e} \\ 0, & \text{when } \tau_{cw} \leq \tau_{cr,e} \end{cases} \tag{3.7}$$

$$S(\tau_{wc}, \tau_{cr,d}) = \begin{cases} (1 - \frac{\tau_{cw}}{\tau_{cr,d}}), & \text{when } \tau_{cw} < \tau_{cr,d} \\ 0, & \text{when } \tau_{cw} \geq \tau_{cr,d} \end{cases} \tag{3.8}$$

$\tau_{cw}$ is defined as the maximum bed shear stress due to current and waves, while $\tau_{cr,e}$ and $\tau_{cr,d}$ represents respectively the user-defined critical erosion and deposition shear stresses. Consequently, the erosion of cohesive sediments occurs if $\tau_{cw} > \tau_{cr,e}$, while deposition when $\tau_{cw} < \tau_{cr,d}$.

For non-cohesive sediments (e.g.,sand) transport, the approach of Van Rijn [69] is the followed by default, although other formulations are available. The Van Rijn formulation is based on the definition of a reference height $a$ [67]:

$$a = min \left[ max \left\{ k_s, \frac{\Delta_r}{2}, 0.01h \right\}, 0.2h \right] \tag{3.9}$$

where $k_s$ is the current-related effective roughness height as determined in the Delft3D-FLOW module and $\Delta_r$ is the wave-induced ripple height, set to a constant value of 0.025 m. Below the reference height the sediment transport is treated as bedload, while above is treated as suspended load. Sediment is entrained in the water column by imposing a reference concentration at the reference height. The volumetric concentration is computed according to Van Rijn et al. formula [69]. Multiplying the volumetric reference concentration by the specific density $\rho_s$ is possible to get the mass concentration at the reference height. The settling velocity is evaluated according to the sediment diameter in suspension. In 2D the entrainment and the deposition are expressed as follow:

$$S = \frac{c_{eq} - c}{T} \tag{3.10}$$

where $S$ is the total net source and sink, $c$ is the depth-averaged concentration and $c_{eq}$ is the equilibrium depth-averaged concentration based on the selected transport formula. $T$, instead, is given by the ratio of the settling velocity $w_s$ over the water depth $h$ multiplied by a dimensionless time scale derived by the work of Galapatti [22]. Further explainations on the 3D equations and on all the sediment transport formulations are available in the Delft3D-FLOW Manual [15].

Bedload transport is calculated for sediment fractions classified as *sand* and *bedload*. Firstly, the magnitude and direction of the bedload transport at the cell centres is computed using the transport formula adopted. Then, the transport rates at the cell interfaces are determined, corrected for bed-slope effect and upwind bed composition and sediment availability.

According to Van Rijn formula, the transport components can be classified as bedload due to currents, bedload due to waves and suspended load due to waves. When included waves, the magnitude and the direction of the bedload transport on an horizontal bed are computed by the Van Rijn formulation [70].

$$q_b = 0.006 \rho_s w_s d_{50} M_s^{0.5} M_e^{0.7} \tag{3.11}$$

where $\rho_s$ is the sediment density, $M_s$ is the sediment mobility number due to waves and currents and $M_e$ is the excess sediment mobility number, for which the reader is referred to [15]. The direction of the bedload is determined considering the two components due to currents and waves: the former acting in the direction of the currents, the latter acting in the direction of the wave propagation. The bedload transport takes place when the shear stress at the bottom exceeds the critical shear stress:

$$\tau_{cr} = (\rho_s - \rho_w) g D_{50} \theta_{cr} \tag{3.12}$$

whit threshold parameter $\theta_{cr}$ calculated according to the classical Shields curve and modelled by van Rijn [69] as a function of the non-dimensional grain size $d^* = d_{50}(\frac{\Delta g}{\nu^2})^{1/3}$. In the latter equation, $\Delta = \frac{\rho_s - \rho_w}{\rho_w}$ is the submerged specific gravity of a sediment with density $\rho_s$, $\rho_w$ is the water density and $\nu$ is the kinematic viscosity of water.

The bed can be modeled as a unique, uniformly mixed bed layer (a single sediment layer) or as a stratigraphy (multiple sediment layers). In the former case, it is not specified the order of the deposited sediments and all sediments are available for erosion. In the latter case, the composition of each layer must be properly defined by the user. All the deposited sediments are initially added to the top-most layer, where they are mixed, before being pushed towards the layers beneath it. Once the user-defined thickness is exceeded, a new layer is created until the number of layers reaches the maximum defined; otherwise, layers at the bottom of the stratigraphy are merged. For more details on the sediment and morphology computations, the reader is sent back to [15, 39]. In the case of multiple sediment layers, only those in the top-most layer are available for erosion. After erosion, sediments in the top-most layer are replaced by those below.

When modeling complex geometries, as the one of the Arsenale, the setting-up of an accurate and efficient model grid can be quite difficult due to the irregular domain boundaries. Moreover, in order to reduce the computational time without losing accuracy in some areas of the domain, the user may want to refine the grid gradually for gaining the appropriate resolution to adequately simulate physical processes in such areas. In Delft3D-FLOW, this can be achieved by using the domain decomposition approach, which consists in the subdivision of the model into non-overlapping domains, each covered by its own structured grid. Then, computations can be carried out separately on these domains that communicate through internal boundaries, the DD-boundaries, acronym for Domain Decomposition. According to Deltares [15], such technique is the numerical approach that meets best the demands of efficiency, accuracy and general applicability. Domain decomposition uses a direct iterative solver, comparable to the single domain implementation, for the continuity equation; whilst the additive Schwarz method, which allows for parallelism over the domains, is used for the momentum equations, the transport equation and the turbulence equations. This implementation has allowed the domain decomposition to have a similar robustness as the single domain Delft3D-FLOW code.

### 3.1.2 FUNWAVE-TVD numerical solver

FUNWAVE-TVD is the Total Variation Diminishing (TVD) version of the fully nonlinear Boussinesq wave model proposed by Shi et al. [58]. The FUNWAVE model was initially developed by Kirby et al [34]. The development of the present version was due to the need for modelling of surfzone–scale flow processes in a Boussinesq model framework, and modeling of Tsunami waves in both a global/coastal scale for prediction of coastal inundation and a basin scale for wave propagation. This version provides many theoretical and numerical improvements, including:

- A more complete set of fully nonlinear Boussinesq equations;
- Monotonic Upwind Scheme for Conservation Laws (MUSCL) – TVD solver with adaptive Runge–Kutta time stepping;
- Shock–capturing wave breaking scheme;
- Wetting–drying moving boundary condition with incorporation of Harten-Lax-van Leer (HLL) construction method into the scheme;
- Lagrangian tracking;
- Option for parallel computation.

For a more complete description of the governing equations, the reader can refer to FUNWAVE Documentation (https://fengyanshi.github.io). Subsections 4.2.1.1 and

4.2.1.2 will provide more information about the sediment trasport and the ship-wakes modules.

### 3.1.3 Wave propagation

An extreme value analysis was conducted, using the Copernicus data, to define the 100-year return period wave characteristics (wave height, period, and direction), to force the FUNWAVE model, and to observe the wave propagation within the La Spezia gulf. More details are available in the Appendix A.

Local wind waves were not taken into account in the numerical simulations due to their negligible contribution in the hydro-morphodynamics of the Arsenale. The wave growth is strongly limited by the length of the fetch inside the Arsenale, about 1.5 km. A brief computation of the wind-driven waves generation, based on the JONSWAP approach [31] and revised by the Shore Protection Manual [1], revealed that the most intense wind from SSE, characterized by a speed of 20 m/s (38.87 kn), blowing for 48 hours over the Arsenale basin, could generate wave heights of 0.56 m, having a peak period of 2.16 s. Although wave heights would not be negligible, small periods would entails reduced wave energy, i.e. small relevance for the circulation and sediment transport processes investigated in this work.

Wave propagation was performed by preferring the use of a wave-resolving model to wave-averaging approaches; the former provides, by construction, better performances than the latter in relation to those processes that characterize the evolution of the wave field over a complex topography. In particular, the Boussinesq-type FUNWAVE model was chosen because of its good handling of wave–wave interactions, refraction, diffraction, wave–structure interaction, and wave breaking. Diffraction and reflection, which are usually poorly resolved by wave-averaging models, become particularly important when approaching coastal structures and harbour basins. The use of FUNWAVE for the wave propagation is also supported by the values of the frequency dispersion parameter kh, which vary from 0.66 (offshore region of the domain) to 0.76 (Arsenale area), i.e., the standard range of applicability of Boussinesq-type models (e.g., [8]).

Two computational domains were set up. The first (outer) domain, as shown in Figure 3.1, was characterized by a spatial resolution of 5 m $\times$ 5 m and extended 30 km in the longshore direction and 25 km in the cross-shore direction, from Riomaggiore (north) to Forte dei Marmi (south). It was used to run a large-scale simulation to propagate the waves from a 30 m water depth (red line in Figure 3.1, where the input waves were forced) to the La Spezia gulf. The model was forced with a Jonswap-type spectrum characterized by a wave of significant height $H_s$ = 6.93 m, peak period $T_p$ = 13 s, and peak direction $\theta_p$ = 230° N.

Then, a second inner model, as shown in Figure 3.1, was realized to define the wave agitation inside the basin. This domain extended from the area immediately shoreward of the main breakwater to the Arsenale and had a finer spatial resolution, about 2.5 m $\times$ 2.5 m. It was forced with the results provided by the outer model with a Jonswap spectrum, characterized by $H_s$ = 0.25 m and the same peak period of the previous spectrum, i.e., $T_p$ = 13 s. Regarding the direction, the waves for the inner model were input perpendicularly to the boundary. Observe that the wave parameters for the inner model are far smaller than those for the outer model due to the significant wave refraction from the wave generation (wave direction $\theta_p$ = 230° N) to the main breakwater of the La Spezia harbour (normal direction of 146° N); to the diffraction induced by the islands; and to the strong damping of offshore waves by the main breakwater. In both models, the breakwaters at the entrance of La Spezia gulf and those delimiting the Arsenale were modelled as impermeable and reflective structures.

### 3.1.4 Hydrodynamic and sediment transport modelling

Hydrodynamic and sediment transport modelling within the Arsenale was conducted with Delft3D, described in 3.1.1. The numerical simulations were performed in 2D by the FLOW module of the Delft3D suite [15], which solves the Navier–Stokes equations

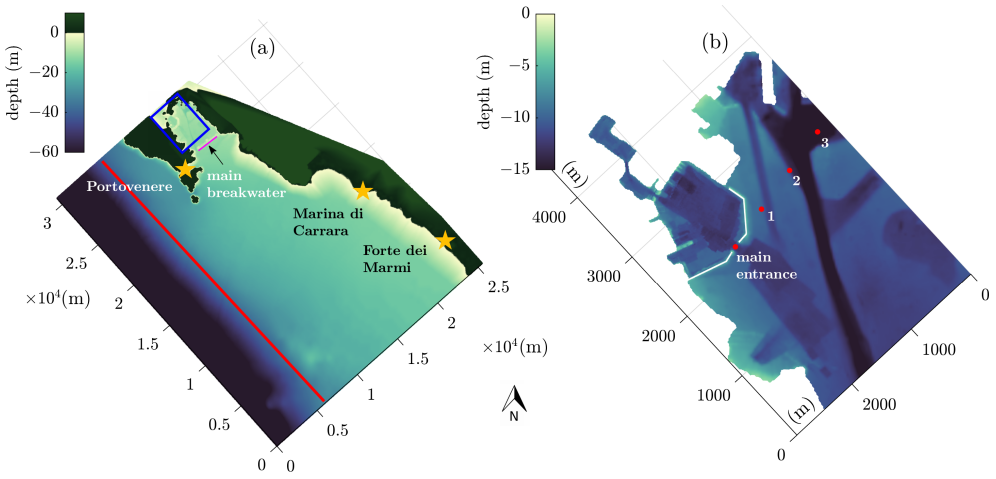


Figure 3.1: (a) Outer FUNWAVE domain; the red line represents the boundary where the waves were imposed; the blue rectangle highlights the inner domain shown in panel (b). The red dots represent the probes at which local modelled wave time series were extracted.

under shallow water and the Boussinesq assumptions and provides depth-averaged quantities.

For this specific case study, for which we are interested in the overall hydro-morphodynamics of the basin, rather than on local details about sediment transport and deposition, we resorted to a 2D, depth-averaged approach. The validity of this approach is confirmed by our results, which show how short waves have little influence on the hydro-morphodynamics: the water currents within the Arsenale can be effectively described by 2D models. Finally, our choice was also due to the lack of field data, due to the fact that Arsenale is a military area. However, the aim of this preliminary study was mainly to gain an in-depth knowledge on the processes governing the hydro-morphodynamics; therefore, we preferred to limit the assumptions on the missing data and to further improve the numerical modelling when more accurate measurements become available.

The regular grid, created with the Delft3D-RGFGRID module and shown in Figure 3.2, covered both the military and the shipping areas. It extended about 2.3 km in the offshore direction and 3.5 km in the alongshore direction, with a spatial resolution between 5 and 10 m. The grid, in WGS 84—UTM 32N coordinates, was rotated about 45° to better adapt to the orientation of the gulf. The grid lines were curved along the land boundaries, obstacles, and channels so that the "staircase boundary effect" [13], which could induce artificial diffusion, was avoided. The chosen domain setup allowed us to bypass the notorious problems that Delft3D encounters when resolving wave diffraction. In fact, we used FUNWAVE to bring the wave signal directly to the Arsenale main entrance (red line in Figure 3.2) so that it was not necessary to model the wave diffraction with the Delft3D-WAVE module (phase-averaged model) [16]. By using the Riemann boundary condition on the main entrance (explained in 3.1.5), waves could propagate within the basin without encountering any other obstacles, avoiding Delft3D-WAVE issues in modelling the wave diffraction pattern.

It is worth mentioning that at the LR Arsenale entrance the wind waves are so small that they can be assumed to be negligible. Figure 3.2 also shows all the boundaries, in different colours; these are detailed below in the descriptions of the scenarios.

The bathymetries of the Arsenale and surrounding areas shown in Figure 3.1 were created using a bathymetric survey carried out in 2016 by the Istituto Idrografico della Marina for the areas up to the main breakwater, while the outside depth values from the EMODnet bathymetry domain were interpolated at the grid cell corners. The survey has a spatial resolution of 2 m for the Arsenale and 25 m for the rest of the domain, which involves the coastal region of the La Spezia gulf up to the main breakwater, while the EMODnet dataset has a resolution of about 80 m.

Based on data from in situ samplings, the seabed was modelled as one single

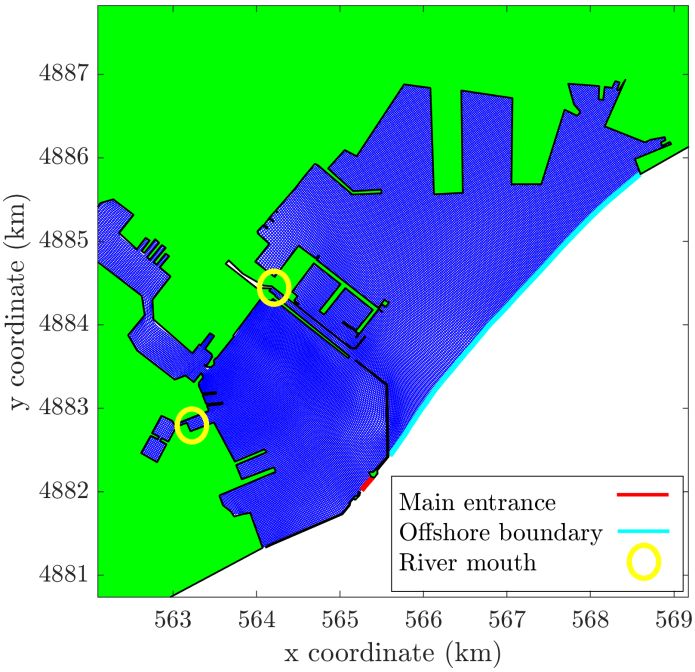


Figure 3.2: The computational domain of the Arsenale and shipping areas, used for the Delft3D simulations.

Table 3.1: Parameters used for the simulations.

| **Parameter(Unit Measure)** | **Range** | **Used Value** |
|---|---|---|
| $CDryB$ (kg/m$^3$) | 200 – 500 | 500 |
| $M$ (kg/m$^2$/s) | $10^-5$ – $10^-2$ | $10^-4$ |
| $\tau_{cr,e}$ (N/m$^2$) | 0.1 – 0.97 | 0.97 |
| $\tau_{cr,d}$ (N/m$^2$) | 0.01-100 | 0.1 |
| $w_s$ (mm/s) | 0.025 – 0.25 | 0.25 |

layer, uniformly mixed and characterized by both cohesive (mixture of clay and silt) and non-cohesive (sands with median diameter of 200 µm) sediments in different percentages, inside and outside the Arsenale. The sand distribution was assumed to be about 30% and 70%, respectively, within and outside the Arsenale, and vice versa for the cohesive fraction. The initial, space-varying sediment thickness was defined in terms of the dry bed densities and volume fractions of the sediments implemented.

For the characterization of the cohesive sediment inside the Arsenale area, no field or laboratory data were available. Therefore, we performed a sensitivity analysis to assess the effect of the main calibration parameters on the sedimentation inside the Arsenale. The most dominant calibration coefficients are the dry bed density ($CDryB$), the erosion parameter M, the critical erosion/deposition shear stresses ($\tau_{cr,e}$,$\tau_{cr,d}$), and the settling velocity $w_s$ [63]. Table 3.1 reports the ranges within which the parameters were varied and the values used in the simulations. Sensitivity tests revealed that the factors most affecting the sedimentation inside the basin were the dry bed density, the critical shear stress for deposition, and the settling velocity. Although the relative deposition changes between the tested values were significant, the absolute difference was of the order of a few centimetres, with a maximum amount of sedimentation that remained smaller than 1 dm. The effects of the erosion parameter and the critical shear stress for erosion were manifested almost only along the rivers, without altering the deposition inside the Arsenale. Considering the obtained results, we chose reasonable values according to what were generally used in previous modelling studies [24], [41], [42], [43] and to the Van Rijn formulation for mud–sand mixtures [71].

Table 3.2: Overview of three scenarios and forcings actions activated in each.

| | **Tide(T)** | **Waves (W)** | **Rivers' Discharges (R)** | **Wind** |
|---|---|---|---|---|
| **Scenario1 (TW)** | Time series | Time series | | From 30°N V=15 m/s and from 150°N V=20 m/s |
| **Scenario2 (TR)** | Time series | | Time series | From 30°N V=15 m/s and from 150°N V=20 m/s |
| **Scenario3 (TWR)** | Time series | Time series | Time series | From 30°N V=15 m/s and from 150°N V=20 m/s |

Numerical simulations were undertaken to evaluate the overall Arsenale hydrodynamic circulation and related sedimentation mechanisms. Such information is of fundamental importance for managing purposes (e.g., mitigation of sedimentation processes, localized dredging, etc.). As mentioned above, we ran three scenarios, characterized by different flow – sediment transport forcing, to inspect the role of various forcing combinations (Table 3.2). For the present analysis of the main characteristics of the hydro-morphodynamic circulation, we neglected the effects induced by temperature and salinity, assuming a negligible difference between the freshwater streams and the water inside the basin. The duration of each simulation was 48 h.

### 3.1.5 Scenario 1 (TW): Tide, Waves, and Wind Implementation

The first scenario was run to understand the effect of waves and tide on the Arsenale dynamics, while neglecting the contribution of riverine flows (Table 3.2). Two simulations were performed to account for two different uniform wind fields, with speeds of 15 m/s from 30° N (NNE wind) and 20 m/s from 150° N (SSE wind), respectively. These values are associated with a return period of 100 years, derived from an extreme value analysis of the available data extracted from the La Spezia ISPRA station.
We imposed a Riemann-type condition at the offshore boundary and at the main entrance of the Arsenale to account for both wave and tide actions. The incoming Riemann variable is $R = (U_n \pm 2\sqrt{gH})$, where $U_n$ is the normal-to-boundary velocity component of the flow, while $H$ is the total water depth, and $g$ is gravity acceleration. The Riemann boundary condition was implemented by Delft3D through the following linearized relation:

$$f(t) = U_n(t) + \zeta(t)\sqrt{\frac{g}{h}} \tag{3.13}$$

where $\zeta$ is the water level, $h$ is the water depth, and $t$ is time. The velocity component of the flow and the water level due to the waves were extracted from the 2 h FUNWAVE simulation at the locations depicted in red in Figure 3.1, with a time resolution of 1 s. The FUNWAVE time series were repeated to match the duration of the Delft3D simulations of 48 h. The water level time series $\zeta(t)$ was obtained by adding the water level due to the wave propagation, as modelled by FUNWAVE and described in 3.1.3, to the water level recorded by the La Spezia tide gauge during a spring tide (the maximum tidal excursion was equal to 0.3 m) so that the effect of the tide was enhanced. The mean value of water depth for each section of the boundary was derived from the bathymetry and kept constant since no significant changes in the seabed were expected at the offshore boundary.

To better implement the Riemann-type boundary condition, we discretized the offshore boundary (cyan line in Figure 3.2) into 3 sections, centred at the probes 1, 2, and 3 (see Figure 3.1). For each boundary section, a Riemann time series was computed with wave input coming from the respective FUNWAVE probe and then imposed on the initial and last part of the respective section, linearly interpolating the intermediate values along the stretch.

### 3.1.6 Scenario 2 (TR): Tide, Rivers' Discharges, and Wind Implementation

In the second scenario, we neglected the influence of the waves to analyse the effect of the freshwater streams and the tide on the hydrodynamics and the sediment transport processes. To model the rivers' discharges, total discharge boundary conditions were

applied at the points representing the rivers' mouths (shown as yellow circles in Figure 3.2). Both discharge and sediment concentration time series were required; for this purpose, a triangular hydrograph lasting 24 h was created to represent the time evolution of the water discharges, with peaks of 209.48 $m^3/s$ and 64.64 $m^3/s$ for the LR and CR, respectively. Such values represent the 100-year return period of the rivers' discharges. Sediment concentrations were taken as constant and equal to 2.65 $kg/m^3$ for the LR and 1.36 $kg/m^3$ for the CR, respectively. To complete the analysis, the offshore boundary was forced with a water level time series of tidal oscillations only, and the wind field was implemented as already described in Section 3.1.5.

### 3.1.7 Scenario 3 (TWR): Tide, Rivers' Discharges, Waves and Wind Implementation

In the third scenario, we superposed the forces implemented in Scenarios 1 and 2, i.e., the tide, the wave action, the wind, and the freshwater streams, to account for all the possible forcing acting at the Arsenale.

The boundary conditions were applied in a similar manner to those of the previous scenarios. Again, two total discharge boundary conditions were applied at the rivers' sections, and the sediment flux time series were the same as those of Scenario 2. The Riemann-type boundary condition imposed at the offshore boundary was modified to let the rivers' discharges leave the domain at the open boundaries.

## 3.2 Results from the study of the sediment transport in the Arsenale

### 3.2.1 Wave propagation results

The results of the numerical simulations of the wave propagation with FUNWAVE showed that the offshore waves were significantly reduced due to the presence of the Portovenere and Palmaria and Tino Islands, which protected the gulf area. The maximum values of the wave height were found to be about 1.5 m close to the main breakwater (left panel of Figure 3.3). The waves were slightly rotated by diffraction and refraction and approached the main breakwater almost perpendicularly. Such a structure strongly damped the waves, with the wave height being reduced to 0.25 m inshore of the breakwater. Then, the waves propagated inside the Arsenale, being further reduced by the emerged breakwaters surrounding it. As shown in the right panel of Figure 3.3, the resulting wave agitation inside the military harbour was very mild, with water elevations smaller than 0.03 m.

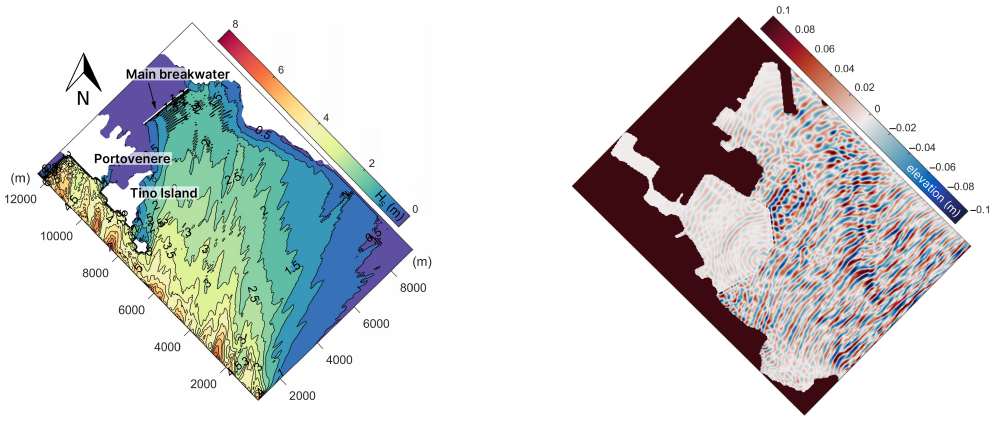


Figure 3.3: Wave propagation in the outer FUNWAVE model (left panel); water elevation in the inner FUNWAVE model (right panel).

### 3.2.2 Hydrodynamic and Sediment Transport Modelling

#### 3.2.2.1 Scenario 1 (TW): Tide, Waves, and Wind Implementation

In Scenario 1, the actions of tide, waves, and wind were simultaneously activated. The results showed that the overall water level oscillation inside the Arsenale was similar to that of the tidal range, around 0.35 m, confirming that the wave effect was not relevant due to very small wave heights (right panel of Figure 3.3). The tide was thus the main actor in defining the flow patterns, determining the fluctuations of both the water level and the velocities. During the flood phase, the water entered the Arsenale through the mouths, while tidal emptying occurred during the ebb phase. The maximum velocities were reached in the area of the LR entrance, due to the narrowing of the section, in relation to the falling tide. Here, the critical bed shear stress for erosion was exceeded rarely and briefly, during the receding of the ebb tide. This implied that the modelled forcing actions were not intense enough to resuspend the sediments on the seabed and to generate the sediment transport processes. In fact, the modelled sediment suspended concentration (SSC) and sedimentation patterns confirmed that no variation of the bed took place during the simulation (not shown here). Additionally, it was observed that the effect exerted by the wind, from both the NNE and SSE, strongly affected the rotation and the in-tensity of the circulation inside the basin: the NNE winds generated an anticlockwise circulation (left panel of Figure 3.4), while the SSE winds determined a clockwise velocity field (right panel of Figure 3.4).

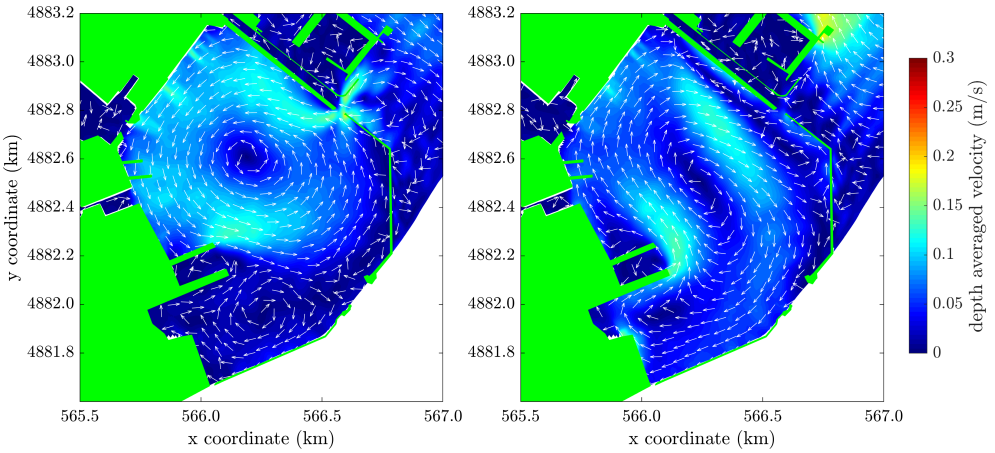


Figure 3.4: Modelled hydrodynamic circulation forced by NNE wind (left panel) and SSE wind (right panel) for the TW scenario. The arrows give the velocity direction, while the intensity is given by the colormap.

#### 3.2.2.2 Scenario 2 (TR): Tide, Rivers' Discharges, and Wind Implementation

In Scenario 2, the effect of the waves is turned off and the effect of the rivers' discharges is included. Comparing the results of the TW and TR scenarios in terms of water levels, the only slight difference was due to the wave contribution, while the freshwater streams did not significantly alter the water level inside the basin. The flow circulation was comparable to that of the TW scenario before the occurrence of the rivers' discharges, underlining the dominant role of the tide and wind. During the rising phase of the rivers' discharges, some differences could be observed due to the wind direction. In the case of the NNE wind, the LR discharge was partially pushed into the Arsenale, generating a clock-wise vortex (left panel of Figure 3.5). This vortex increased in size and moved toward the south as the river discharge increased; then, it reduced and retreated toward the entrance at the fall of the river discharge. Conversely, under the SSE winds, the LR discharge bent toward the NE, only slightly entering the Arsenale (right panel of Figure 3.5). The CR discharge, directly debouching into the Arsenale,

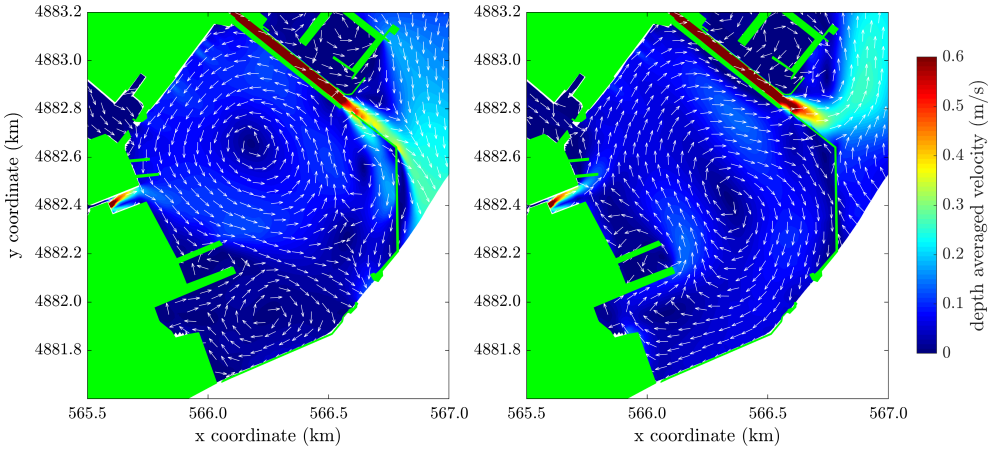


Figure 3.5: Modelled hydrodynamic circulation under NNE wind (left panel) and SSE wind (right panel) at the peak of the rivers' discharges for the TR scenario. The arrows only indicate the velocities' direction, while the intensity is given by the colormap.

followed the wind-forced general circulation and contributed to its intensity.

Figure 3.6 shows that the CR and LR supplied cohesive material into the basin and triggered its suspension when peak discharges were reached. During the discharge fall stage, the input sediment tended to deposit, mainly in the areas of the rivers' mouths. However, despite the large amount of sediment released in the Arsenale, the sedimentation maps, as shown in Figure 3.7, showed very low deposition rates of a maximum of 3 cm near the CR mouth. In addition, the different wind directions affected the sediment spreading, with the SSE wind pushing the sediments more to the northeastern side of the basin than the NNE wind.

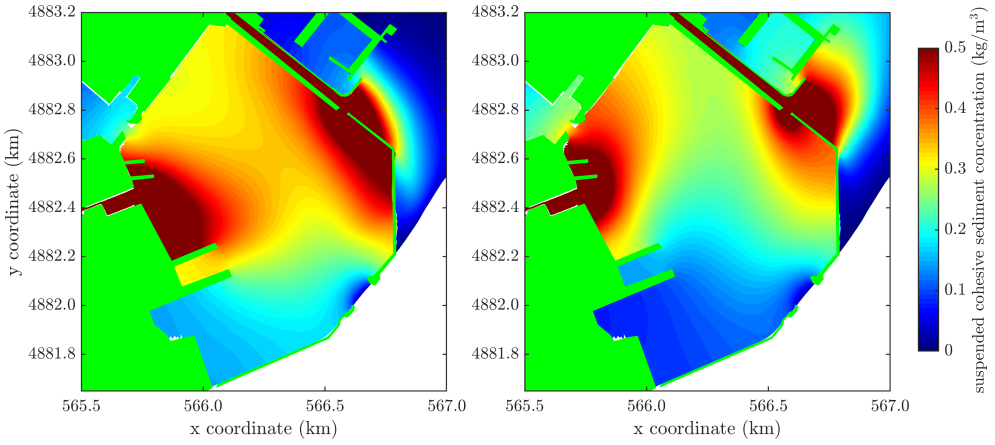


Figure 3.6: Modelled suspended sediment concentration for NNE (left panel) and SSE (right panel) winds at the peak of the rivers' discharges for the TR scenario.

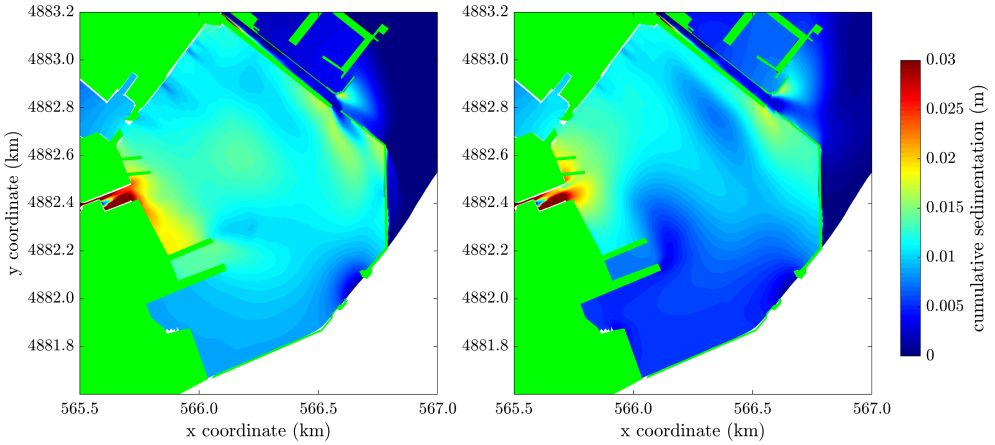


Figure 3.7: Modelled sedimentation patterns for NNE (left panel) and SSE (right panel) winds for the TR scenario.

#### 3.2.2.3 Scenario 3 (TWR): Tide, Rivers' Discharges, Waves and Wind Implementation

The results of the TWR scenario were very similar to those of the TR scenario, confirming that the wave contribution was not very significant for the velocity field (Figure 3.8) and the suspension of the cohesive material (Figure 3.9). Figure 3.8 showed that the circulation patterns were the same as those of the TR scenario, but a weaker velocity was found in the area of the LR entrance, independently of the wind direction and the occurrence of the rivers' discharges.

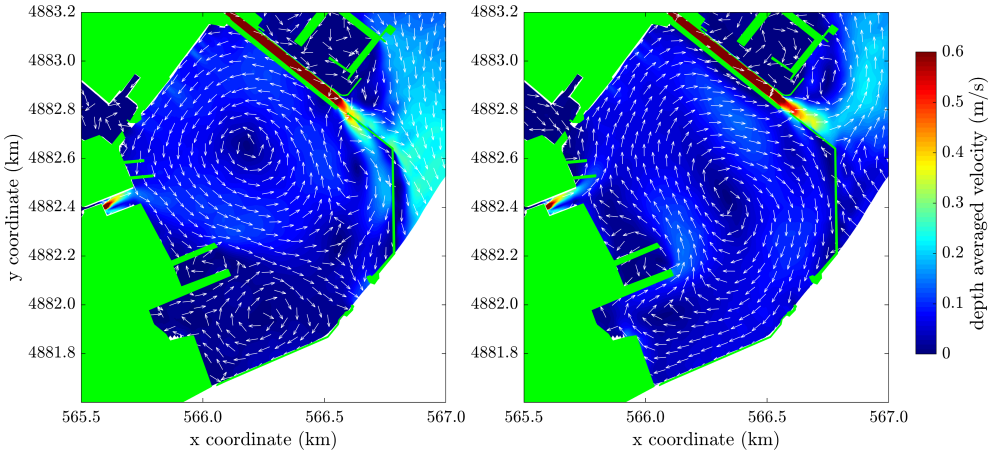


Figure 3.8: Modelled hydrodynamic circulation under NNE wind (left panel) and SSE wind (right panel) at the peak of the rivers' discharges for the TWR scenario. The arrows only indicate the velocities' direction, while the intensity is given by the colormap.

Also either the suspension of the cohesive material (Figure 3.9). Also, the circulation patterns were the same as those of the TR scenario (Figure 3.8), but a weaker velocity was found in the area of the LR entrance, independently of the wind direction and the occurrence of the rivers' discharges. As for the TR scenario, the sedimentation maps, shown in Figure 3.10, highlighted a major deposition close to the rivers' mouths, particularly at the CR mouth, and in the northern part of the Arsenale basin.

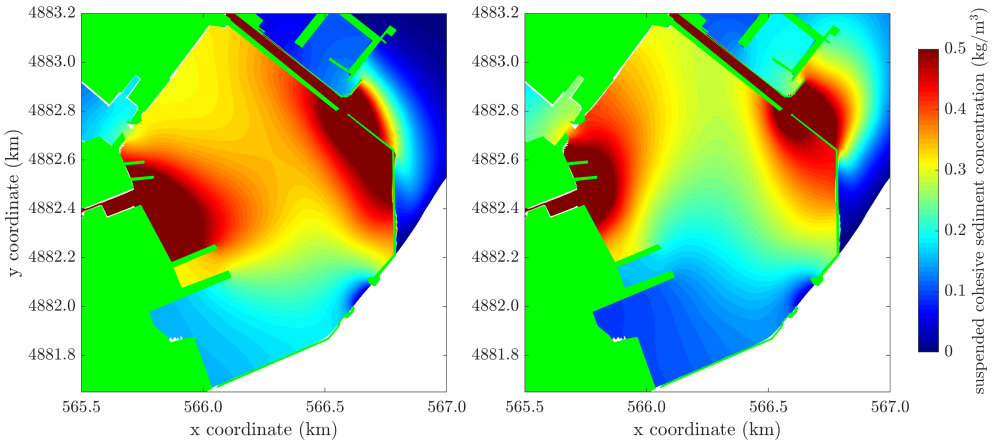


Figure 3.9: Modelled suspended sediment concentration for NNE (left panel) and SSE (right panel) winds at the peak of the rivers' discharges for the TWR scenario.

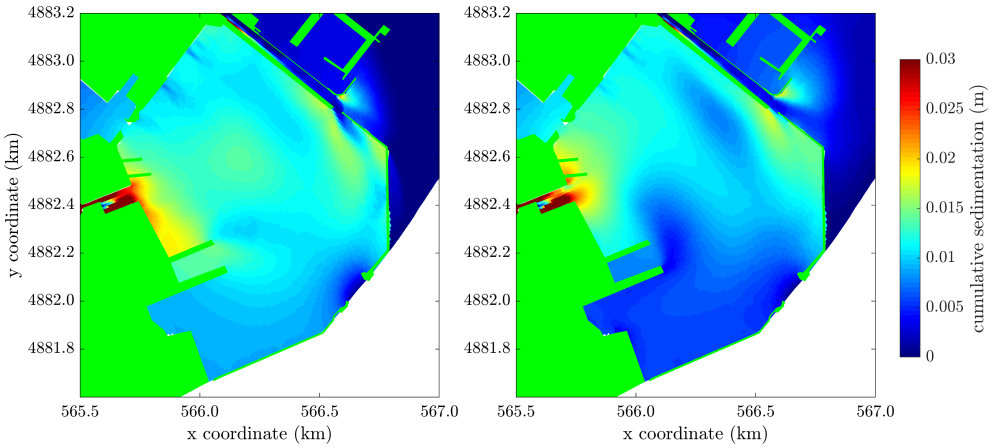


Figure 3.10: Modelled sedimentation patterns for NNE (left panel) and SSE (right panel) winds for the TWR scenario.

# Chapter 4

# Study of the ship-forced sediment transport

## 4.1 Background

In the following, first a brief description of the velocity field induced by a single propeller is presented, giving a general overview of the state-of-the-art research. Then, some expressions in the literature to evaluate the scour caused by the propeller jets are presented.

Several formulations have been proposed to define the magnitude of the efflux velocity, determined applying the axial momentum theory to an ideal propeller. For the application of the momentum theory, the following assumptions had to be taken into account:

- the propeller is taken as an infinitely thin disc, with a negligible thickness in the axial direction;
- the disc has an infinite number of rotating blades, rotating at an infinite speed;
- the disc is submerged in an ideal fluid;
- all elements of fluid passing through the disc undergo an equal increase of pressure;
- the energy supplied to the disc is, in turn, supplied to the fluid without any rotational effects.

In general, it has been demonstrated that the efflux velocity $V_0$ depends on the number of revolutions per unit of time, the propeller diameter and a dimensionless thrust coefficient, typical of the ship. Some of the most widely used formulations are reported here. For example, Fueher and Romisch [20] proposed the following equation, derived from axial momentum theory with the assumption of zero advance speed for the case of a ship manoeuvres:

$$V_0 = nD_p\sqrt{\frac{2D_p^2C_t}{A_p}} \tag{4.1}$$

where $n$ is the number of revolutions per unit of time (rev/s) of the propeller, $D_p$ is the propeller diameter (m), $D_h$ is the hub diameter (m), $C_t$ is a dimensionless thrust coefficient, defined as:

$$C_t = \frac{T}{\rho_w n^2 D_p^4} \tag{4.2}$$

being T (N) the thrust and $\rho_w$ (kg/m$^3$) the water density. By substituting the area of the propeller $A_p = \frac{\pi D_p^2}{4}$, it was obtained

$$V_0 = 1.22n^{1.01}D_p^{0.84}C_t^{0.64} \tag{4.3}$$

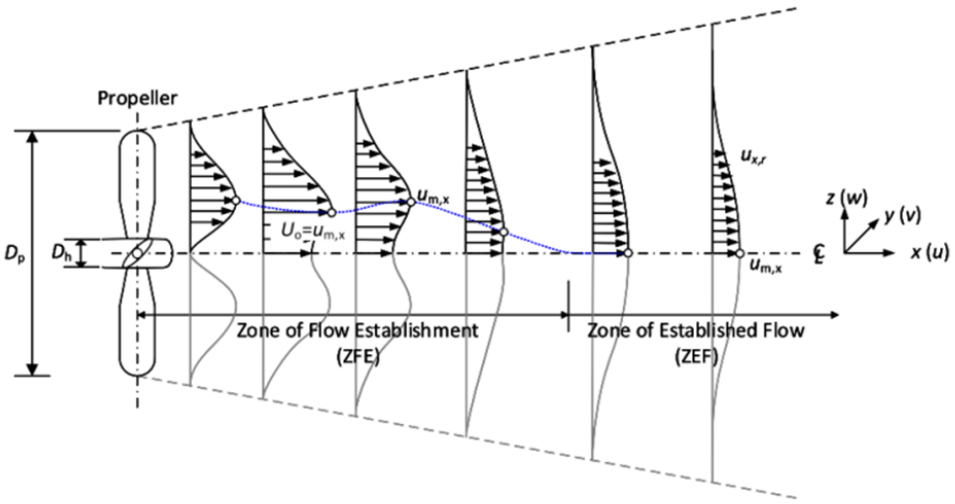


Figure 4.1: Sketch of the propeller's induced axisymmetric flow field.

On the basis of the same parameters, a similar expression has been recently introduced by Hamill et al. [27]:

$$V_0 = 1.59 n D_p \sqrt{C_t} \tag{4.4}$$

Other formulations, as that suggested by Hasmi [30] included additional parameters, like the hub diameter and the Blade Area Ratio (BAR, defined as the ratio of the sum of the face areas of all the blades to the disc area described by the rotation), stating that:

$$V_0 = E_0 n D_p \sqrt{C_t} \tag{4.5}$$

where $E_0$ is the efflux coefficient defined as:

$$E_0 = (\frac{D_p}{D_h})^{-0.403} C_t^{-1.79} BAR^{0.744} \tag{4.6}$$

Due to the unrealistic assumptions of the momentum theory, all the previous expressions of $V_0$ cannot be regarded as accurate, characterized by an error of 20% compared to the experimental data.

For a propeller free jet, in which the diffusion is not bounded, the flow region behind the propeller is conventionally divided in three distinct zones: the efflux zone, the zone of flow establishment (hereinafter ZFE) and a zone of established flow (hereinafter ZEF), each of which is characterized by different expressions of the axial velocity. The efflux zone is the closest area to the propeller, where the axial velocity assumes its maximum, equal to the efflux velocity, from which all the other values are derived from, in relation to the distance to the propeller. The ZFE, where the jet generates and become established, is such that the axisymmetric velocity is lowest at the axis, due to the presence of the propeller hub [28]. Moving from the axis, the influence of the propeller hub decreases, determining an increase of the axial velocity, assuming reaching its maximum value, i.e. the efflux velocity, at a distance of:

$$R_{m0} = 0.67(R_p - R_h) \tag{4.7}$$

depending on both the radius of the propeller $R_p$ and of the hub $R_h$ [3]. Then, the velocity tends to decrease, showing a double-peaked distribution. Regarding the lateral distribution of the axial velocity at a cross sections in the ZEF, a Gaussian normal distribution has been proposed [2] with maximum at the rotation axis. Then, like in typical free jets [7], it decays linearly with the distance x from the efflux plane. A good representation of the distribution of the velocity field induced by the propeller jet is depicted in Figure 4.1.

The flow field induced by a ship propeller is complex, but assuming the ship stationary or moving at low speed, it is possible to neglect the turbulent wake due to the hull and focus only on the propeller jet.

On the basis of work of Albertson et al. [2] regarding the submerged free jet from an orifice into an infinite fluid, PIANC [53] proposed the expression for the computation of the velocity along the axis of the jet $V_{axis}$:

$$V_{axis} = \frac{1}{2C} V_0 (D_p/x) \tag{4.8}$$

From Equation (4.1), also the distribution of the flow velocity in the jet at different locations, valid only in the zone of the flow established, had been presented:

$$\frac{V_{x,r}}{V_{axis}} = \exp\left[-\frac{1}{2C^2} r^2 x^2\right] \tag{4.9}$$

where $C$ is a coefficient, $r$ is the radial distance from the jet axis and $x$ is the horizontal distance from the outflow of the jet.

From the definition of the efflux velocity, it is also possible to estimate the maximum velocity at the seabed caused by propeller jets, which is useful to predict the seabed stresses, sediment mobilization and transport. A largely used expression is that by the German and Dutch methods [32] (PIANC):

$$U_b = C_1 V_0 \left(\frac{h_p}{D_p}\right)^{-1} \tag{4.10}$$

The German and Dutch methods proposed a different value for the $C_1$ parameter. The former method suggested $C_1$ to be equal to 0.42, while the latter advised it to be equal to 0.216. $h_p$ is the bed clearance, i.e. the distance between the rotational axis of the propeller to the seabed (see Figure 4.4). In his work, Maynord [47] suggested to estimate the maximum velocity at the seabed to evaluate the peak bed shear stress induced by the passing-by of a ship. By means of many experimental measurements of the bed shear stress, he defined the friction coefficient as a function of the propeller diameter and the bed clearance:

$$C_f = 0.01 \left(\frac{h_p}{D_p}\right)^{-1} \tag{4.11}$$

This relation is taken as valid with a threshold of $D_p/h_p = 1.2$. This implies that Maynord's model cannot be applied in low bed clearance conditions, less than $1D_p$. With the aim of filling this gap, recently Marroig [50] conducted several laboratory experiments, which led to a new formulation of the friction coefficient, equal to:

$$C_f = 0.0013 \left(\frac{h_p}{D_p}\right)^{-1} \tag{4.12}$$

This model, unlike Maynord's expressions, is suitable to describe also low bed environments and rough bed of sand.

Due to the potential damages made by the propeller jet and the significant role to pratical design and maintenance, a wide number of studies has been devoted to predicting the maximum scour depth, defined $d_s$. Some of the existing formulations for an unconfined propeller jet flow are provided in Table 4.1.

In general, the maximum scour depth at the equilibrium stage can be espressed as a function of:

- the efflux velocity $V_0$
- the diameter of the propeller $D_p$
- the median sediment size $d_{50}$
- the difference between the sediment-grain density $\rho_s$ and the water density $\rho_w$ (i.e., the relative submerged grain density)

– the bed clearance $h_p$

– the gravity acceleration $g$

– the kinematic viscosity of the water $\nu$.

In dimensionless form, normalizing the maximum scour depth to the propeller diameter, such depth depends on:

– the densimetric Froude number $F_0 = \frac{V_0}{\sqrt{g d_{50}(\frac{\rho_s - \rho_w}{\rho_w})}}$

– the ratio between the propeller diameter and the sediment size $\frac{D_p}{d_{50}}$

– the ratio between the clearance and the sediment size $\frac{h_p}{d_{50}}$

assuming that the the effect of the viscosity can be negleted when $Re > 10^4$ (Reynolds number of the propeller flow $Re = \frac{\rho_w V_0 D_p}{\nu}$), condition occuring for most prototypes and experiments [54].

Table 4.1: Recap of the expressions for the prediction of the maximum scour depth.

| Authors | Equations | Range of validity |
|---|---|---|
| Hamill [28] | $\frac{d_s}{h_0} = 0.0467 \left( \frac{F_0}{\frac{h_p}{D_p}} \right)^{1.39}$ | $5.55 \leq F_0 \leq 18.72$ |
| | | $0.81 \leq \frac{h_p}{D_p} \leq 2.87$ |
| Hong, Chiew and Cheng [33] | $\frac{d_s}{D_p} = 0.265[F_0 - 4.114(\frac{h_p}{D_p})]^{0.955}(\frac{h_p}{D_p})^{-0.022}$ | $6.08 \leq F_0 \leq 10.69$ |
| | | $0.5 \leq \frac{h_p}{D_p} \leq 1.5$ |
| Tan and Yuksel [60] | $\frac{d_s}{D_p} = 0.57[F_0 - 2.1(\frac{h_p}{D_p})]^{0.33}(\frac{h_p}{D_p})^{-1.1}$ | $6.08 \leq F_0 \leq 10.69$ |
| | | $0.5 \leq \frac{h_p}{D_p} \leq 1.5$ |
| Penna et al. [52] | $\frac{d_s}{D_p} = 0.06[F_0]^{1.34}$ | $3.65 \leq F_0 \leq 9.54$ |
| | | $0.83 \leq \frac{h_p}{D_p} \leq 1.17$ |
| Curulli, Penna and Gaudio [11] | $\frac{d_s}{D_p} = 0.90 F_0^{1.30}(\frac{d_{50}}{D_p})^{-0.05}(\frac{h_p}{D_p})^{-0.53}$ | $0.40 \leq F_0 \leq 1.04$ |
| | | $0.83 \leq \frac{h_p}{D_p} \leq 3.08$ |
| | | $3.6 \cdot 10^{-3} \leq \frac{d_{50}}{D_p} \leq 8.4 \cdot 10^{-3}$ |

## 4.2 Methodology

### 4.2.1 Description of the sediment transport and ship-wakes modules in FUNWAVE

The main objective of the present work is to show the relevance of including the impact of the propeller jet in calculations of the ship-induced sediment mobilization and transport and in the related seabed morphological evolution. This is done by describing the implementation of a suitable, although simplified, formulation for the propeller jet, applied into the vessel and sediment module of the open-source depth-averaged Boussinesq model FUNWAVE-TVD [58] and to show how affects the hydro-morphodynamics.

#### 4.2.1.1 Description of the sediment transport in FUNWAVE

The FUNWAVE sediment transport module is based on the quasi-steady flow assumption, regarded as appropriate for predicting the sediment transport in depth-limited regions like the swash zone and seabed-ship hull water region. It computes both suspended load and bedload transport, for both cohesive and non-cohesive sediment fractions. In the following the governing equations for the non-cohesive sediments are

summarized. The suspended sediment transport is obtained by solving an advection-diffusion depth-averaged sediment concentration equation (4.13),

$$(\bar{c}H)_t + \nabla_h(\bar{c}H(\mathbf{u}_\alpha + \bar{\mathbf{u}_2})) = \nabla_h(\epsilon_s H(\nabla_h \bar{c})) + E - D \tag{4.13}$$

where $\bar{c}$ is the non-dimensional depth-averaged sediment concentration normalized by the sediment density. $H(\mathbf{u}_\alpha + \bar{\mathbf{u}_2}) = \mathbf{M}$ represents the flow rate per unit width, where $H = h + \eta$ is the total water depth. In the present model, the horizontal velocity is espressed as: $\mathbf{u}_\alpha + \bar{\mathbf{u}_2}$, being $\mathbf{u}_\alpha$ the velocity at the reference level $z = z_\alpha$ and $\bar{\mathbf{u}_2}$ the depth-averaged $O(\mu^2)$ contribution. Moreover, $\epsilon_s$ is the horizontal sediment diffusion coefficient evaluated by the formulation proposed by Elder [18]:

$$\epsilon_s = 5.93 u_{*c} H \tag{4.14}$$

where $u_{*c}$ is the shear velocity, calculated by Van Rjin formulation:

$$u_{*c}(x, y) = \frac{\epsilon_s}{-1 + \ln(30H/k_s)} U_c \tag{4.15}$$

in which $U_c$ is the depth-averaged total velocity, $k_s = 2.5 d_{50}$ is Nikuradse roughness coefficient, and $d_{50}$ is the median grain diameter.
In Equation (4.13) E represents the erosion rate, evaluated by the van Rijn's pickup function [66]:

$$E = 0.015 \frac{d_{50}}{a} \left( \frac{|\tau_b| - \tau_{cr}}{\tau_{cr}} \right)^{1.5} d_*^{-0.3} w_f, |\tau_b| > \tau_{cr} \tag{4.16}$$

where $a$ represents the reference elevation, defined as a function of the total water depth ($a = 0.01H$), $d_*$ is the dimensionless grain size:

$$d_* = d_{50} \left( \frac{(s-1)g}{\nu^2} \right)^{\frac{1}{3}} \tag{4.17}$$

with $s$ representing the specific gravity of the sediment and $\nu$ the kinematic viscosity coefficient. $\tau_b$ and $\tau_{cr}$ are respectevely the the bed shear stress and the critical shear stress, defined as follows:

$$\tau_{cr} = \rho_w (s-1) g d_{50} \theta_{cr} \tag{4.18}$$

$$\tau_b = \rho_w \left( \frac{0.4}{1 + \ln(k_s/30h)} \right)^2 U_c^2 \tag{4.19}$$

with $\theta_{cr}$ is the critical Shields parameter, approximately equal to 0.05.
In Equation (4.13) $D$ represents the sediment deposition rate, calculated by Cao's relation [9]:

$$D = \gamma \bar{c} w_s (1 - \gamma \bar{c})^{m_o} \tag{4.20}$$

where $\gamma = min[2, (1 - (1 - n_s)/\bar{c})]$, $n_s$ is the sediment porosity and $m_o$ is a constant number equal to 2.0. The bedload sediment transport, instead, is calculated with the Meyer-Peter and Muller's formulation (4.21) [48].

$$q_b = \frac{8[(\tau_b - \tau_{cr}^b)/\rho_w]^{3/2}}{g(s-1)} \tag{4.21}$$

The morphological module gives the bed evolution on the basis of the sediment continuity equation and uses a time-averaged pickup and deposition rate to compute the morphological changes (4.22):

$$\frac{dZ_b}{dt} = \frac{1}{1 - n_s} (\bar{D} - \bar{E} - \nabla \cdot \bar{\vec{q}_b}) \tag{4.22}$$

where $dZ_b$ represents the time-averaged depth changes with positive values for erosion and negative values for deposition. $\bar{E}$ and $\bar{D}$ are respectively the time-averaged pickup and deposition rates averaged over $dt_{morph}$ in the suspended load model. $\bar{\vec{q}_b}$ is the bedload flux vector averaged over the same time interval in the bedload model.

The spatial discretization of the advection-diffusion equation is achieved by an implementation of both the upwinding and Monotonic Upwind Scheme for Conservation Laws - Total Variation Diminishing schemes; while third-order Runge-Kutta scheme is used for time-stepping, which is consistent with the existing numerical schemes applied in FUNWAVE-TVD. In addition, an avalanche scheme was considered as the slope limiting method for the bed and coastline erosions, as well as a hard bottom methodology to account for non-erodible regions.

#### 4.2.1.2 FUNWAVE description of the ship wakes and waves

FUNWAVE models ship wakes and waves as a pressure source. In particular, according to the shape of the vessel itself it is possible to choose among four types of source functions. The first and second options implement the pressure disturbance, while the third and fourth types are more suitable to describe slender bodies and introduce the additional volume flux induced by the ship motion, applied in the mass conservation. Currently, the ship propeller effect in FUNWAVE has been implemented only for the first type of source function, better described below. Following the approach suggested by [19], [62] and [76], in the first type of source function, the pressure is defined at a center point by the expression (4.23):

$$p_a(\tilde{x},\tilde{y},t) = Pf(\tilde{x},t)q(\tilde{y},t) \tag{4.23}$$

where:

$$f(\tilde{x},t) = \begin{cases} cos^2[\frac{\pi(\tilde{x}-x^*(t)-\frac{1}{2}\alpha_1 L)}{(1-\alpha_1)L}], \frac{1}{2}\alpha_1 L < \tilde{x}-x^*(t) \leq \frac{1}{2}L \\ cos^2[\frac{\pi(x^*(t)-\tilde{x}-\frac{1}{2}\alpha_2 L)}{(1-\alpha_2)L}], -\frac{1}{2}L \leq \tilde{x}-x^*(t) < -\frac{1}{2}\alpha_2 L \\ 1, -\frac{1}{2}\alpha_2 L \leq \tilde{x}-x^*(t) \leq \frac{1}{2}\alpha_1 L \end{cases} \tag{4.24}$$

$$q(\tilde{x},t) = \begin{cases} cos^2[\frac{\pi(\tilde{y}-y^*(t)-\frac{1}{2}\beta W}{(1-\beta)W)}], \frac{1}{2}\beta W < |\tilde{y}-y^*(t)| \leq \frac{1}{2}W \\ 1, |\tilde{y}-y^*(t)| \leq \frac{1}{2}\beta W \end{cases} \tag{4.25}$$

In the rectangle, $-\frac{L}{2} \leq \tilde{x}-x^*(t) \leq \frac{L}{2}$, and $-\frac{W}{2} \leq \tilde{y}-y^*(t) \leq \frac{W}{2}$ zero outside this region; L and W represent the length and width of the ship (shown in Figure 4.4), i.e., the pressure source, respectively. $(\tilde{x},\tilde{y})$ is the coordinate system for the pressure disturbance which may be rotated by an angle relative to the Boussinesq coordinate system $(x,y)$. The coefficients $\alpha_1$, $\alpha_2$ and $\beta$ are required to define the shape of the draught region ($0 \leq \alpha_1, \alpha_2, \beta \leq 1$). In particular, the $\alpha_1$, $\alpha_2$ coefficients refer to the profile of the vessel's bow and stern respectively, while $\beta$ is related to the profile of the cross section of the hull's vessel. Therefore, $\alpha_1$, $\alpha_2$ are taken into account in the definition of the $p(x,t)$, which is used to describe the longitudinal section of the vessel, while $\beta$ is used in the definition of $q(x,t)$, for the description of the cross section of the vessel. These can be obtained from the displaced volume (static submerged volume of the vessel) and the block coefficient (defined as the ratio of the underwater volume of a ship to the volume of the circumscribing block). P, expressed in meters, is the draught of the vessel and controls the surface displacement, while $p_a$ is the static depression around the vessel.

In the ship-wake module, some instabilities may occur in case of large-size vessels with a draught close to channel depth, corresponding to reduced under-keel clearance (UKC), i.e. the distance between vessel keel and seabed. To handle spurious waves due to reduced UKC, FUNWAVE provides some options: the shock capturing method, the friction method and the viscosity method. The shock capturing method allows one to switch the Boussinesq solver into a Nonlinear Shallow Water Equation (NSWE) solver in the vessel region. This area is masked and here the NSWE are solved. With the friction method, a proper friction coefficient is applied in the mask area to damp waves. The viscosity method is another method of dissipation, used in the eddy-viscosity-type wave breaking, but with a lower dissipation rate compared to the friction method. The combined shock capturing method and friction method was found to be the most effective approach to suppress spurious waves and therefore adopted for our numerical simulations [45].

### 4.2.2 Description of the ship propeller effect in FUNWAVE-TVD

In this work, the effect of the velocity field induced by the ship propeller has been added to bed shear velocity $u_{*c}$, which is used for the computation of the bed shear stress.

For the estimation of the friction velocity on the seabed due to the propeller action, it is important to define the velocity field induced by the propeller. As mentioned before, many formulations have been proposed to describe the flow behind the propeller at the level of the propeller axis, characterized respectively by a low core velocity due to the presence of the propeller hub, generating a double-peak distribution in the zone of flow establishment, converging, at a specific distance from the propeller axis, into a Gaussian shape, with a one-peak ridge trend (see Figure 4.1).

In the implementation of the present study, the velocity field on the bed level (at a very small distance) has been defined. Precisely, in order to follow the same approach used in the computation of the shear velocity in the sediment transport module of FUNWAVE [58], it is possible to assume the distance from the seabed as the Nikuradse roughness coefficient, $k_s = 2.50 d_{50}$. There, the velocity field induced by the propeller has been modelled using to the following expressions:

$$U_p(x,y) = \begin{cases} V_0 \exp(-2\frac{y^2+{h_p}^2}{D_p^2}) & \text{in the ZFE where } x \leq \frac{D_p}{2c_p} \\ V_0 \frac{1}{2c_p}\frac{D_p}{x} \exp(-\frac{1}{2c_p^2}\frac{y^2+{h_p}^2}{x^2}) & \text{in the ZEF where } x \geq \frac{D_p}{2c_p} \end{cases} \tag{4.26}$$

where $x$ and $y$ are the distances in the longitudinal and transversal direction respectively, $V_0$ is the propeller efflux velocity, $h_p$ is the distance between the propeller axis and the seabed, i.e., the bed clearance, $c_p$ is a constant varying for ducted/non-ducted propellers, respectively suggested to be equal to 0.17/0.19 by Blauuw and Kaa's work [4]. The main difference in this parameter depends on the presence of a non-rotating nozzle. In the case of ducted propellers, the propeller is housed within a cylindrical or elliptical duct. This design contributes in improving the efficiency of the propeller, by reducing tip vortex losses and increasing thrust at lower speeds.

The formulation of the nearbed velocity in the zone of flow established, in Equation (4.26), has been partially derived from Equation (4.9) suggested by PIANC [53] and then adapted to the two-dimensional FUNWAVE model. Similarly to Equation (4.9), the proposed nearbed velocity in the ZFE depends, at all location, on the magnitude of the efflux velocity $V_0$, the maximum velocity located at the initial plane of the jet. This term is, then, dumped to take into account all the other parameters involved in the definition of the nearbed velocity. The major role in reducing the efflux velocity is played by the term $D_p/x$. $D_p$, the propeller diameter, is constant, while $x$ represents the longitudinal distance from the propeller, to which the nearbed velocity is inversely proportional. This implies that the effect of the propeller decreases with increasing distance. In the exponential term, from the comparison of the original formulation proposed in PIANC and that proposed in the present work, it can be easily observed that the radial distance $r$, has been substituted by the sum of $y^2 + h_p^2$. The original relation, in fact, is valid for a 3D model. This explains the nearbed velocity dependence on the distance from the propeller along the cross-flow direction, through $y$, and on the bed clearance, through $h_p$, confirming respectively that the smaller is the distance from the propeller, the stronger is the propeller effect on the nearbed velocity. Moreover, the closer is the propeller to the bed level, the higher is its contribution to the nearbedvelocity field. For the ZFE, instead, the expression proposed here is based on the continuity of the velocity field between the two zones. At the intersection of the ZFE and the ZEF, at $x = D_p/2c_p$, the velocity must assume the same value. As a consequence, the equation for the ZFE can be easily obtained by substituting $x = D_p/2c_p$ in the ZEF formulation. It is worth mentioning that, in this work, the so-called efflux zone, located at the propeller face and extending down to a distance of $x = 0.35D_p$, has not been included in the model because the limited length of this zone, about 1.2 m for this test case, would be covered by one single cell of the computational domain, being the spatial discretization in the x-direction of 1 m.

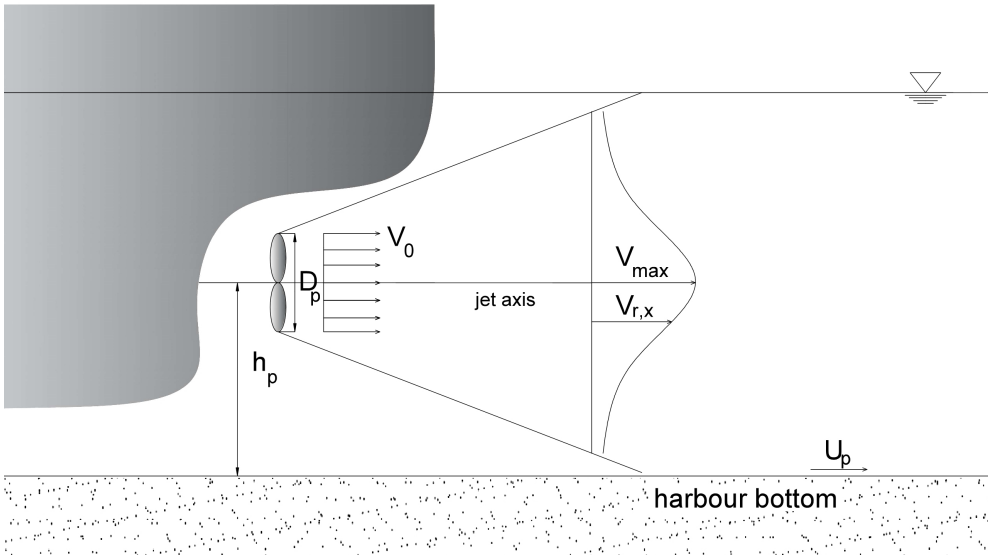


Figure 4.2: View of the velocity distribution of the main propulsion system without rudder.

A typical velocity distribution of the main propulsion system without rudder is shown in Figure 4.2. A 3D simplified sketch of the velocity distribution induced by the propeller on the seabed is depicted in Figure 4.3. The velocity field behind the propeller jet along the propeller axis is given in black, the propeller-induced velocity projected on the bed level is shown in red, as it has been modelled in this work.

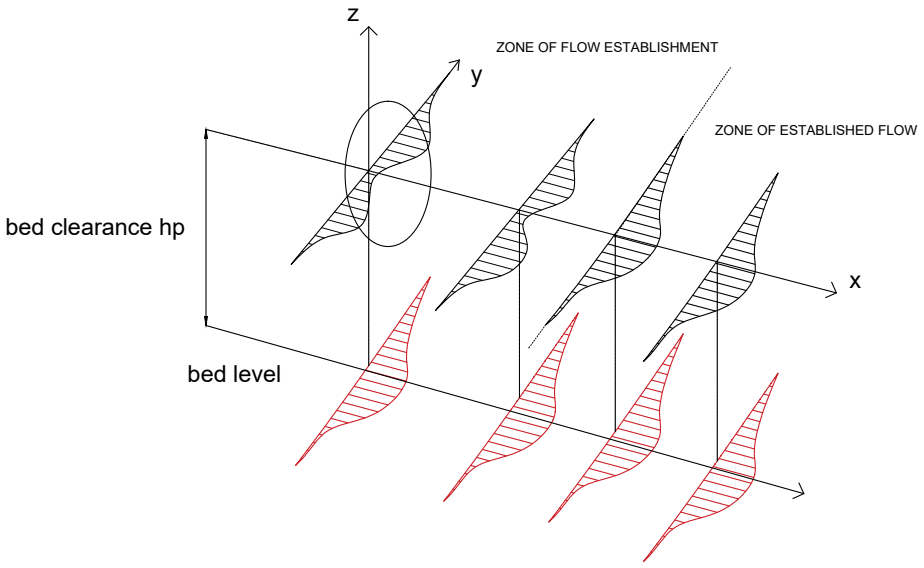


Figure 4.3: 3D sketch of the distribution of the axial velocity induced by the propeller at the propeller axis and on the seabed.

Having defined the propeller-induced velocity field on the seabed, the bed shear stress has been estimated imposing that the mean bed shear stress is proportional to the square of the velocity at the bottom through a friction coefficient $C_f$ [4]. Subsequently, the corresponding friction velocity and bed shear stress are given by:

$$u_{*cp}(x,y) = U_p\sqrt{\frac{C_f}{2}} \tag{4.27}$$

$$\tau_p(x,y) = \rho_w \frac{1}{2} C_f U_p^2 \tag{4.28}$$

Table 4.2: Main stages of the numerical implementation

| | |
|---|---|
| **1** | Computation of both longitudinal and transversal components (defined as vectors) of the axial velocity, induced by the propeller for each single vessel (vessel module). |
| **2** | Computation of the friction velocity induced by ships' propellers (vessel module). |
| **3** | Coupling between the vessel and the sediment module through the definition of the new friction velocity, including also the contribution of the ship propeller (sediment transport module). |
| **4** | Computation of the new bed shear stress, accounting for the ship propeller effect (sediment transport module). |

In this work, the friction coefficient $C_f$ has been expressed as a function of the ratio between the propeller diameter and the bed clearance according to the Maynord approach [47]:

$$C_f = 0.01 \frac{D_p}{h_p} \tag{4.29}$$

Therefore, the total shear velocity is computed from the superposition of the original shear velocity (the right hand side in Equation (4.30)) and the shear velocity from the propeller (the left hand side in Equation (4.30)) :

$$u_{*c}(x,y) = \frac{\epsilon_s}{-1 + \ln\left(\frac{30H}{k_s}\right)} U_c + U_p \sqrt{\frac{C_f}{2}} \tag{4.30}$$

while the new bed shear stress is evaluated as follows:

$$\tau(x,y) = \rho_w \left( \frac{\epsilon_s}{-1 + \ln\left(\frac{30H}{k_s}\right)} \right)^2 + \rho_w \frac{1}{2} C_f U_p^2 \tag{4.31}$$

being the first and the second term in Equation (4.31) respectively the original and the propeller-induced bed shear stress.

The main stages of the numerical implementation in the ship wakes and sediment transport modules of FUNWAVE-TVD are summarized in Table 4.2 and better explained in the following:

- *Step 1:Definition of the ship and propeller characteristics*

  Through the vessel file, recalled in the main input file, it is possible to provide the ship characteristics, like the location, the heading and the speed (these are automatically computed from the time series of the vessel path, expressed by the initial and final position of the centre of the ship), the vessel length, width and draught, specifying the type of pressure and the shape parameters (see section 4.2.1.2). The propeller effect is modelled by activating the appropriate flag in the Makefile. The propeller characteristics should be added in the same file, i.e. the propeller diameter, the revolution speed, the thrust coefficient and the bed clearance. Then, according to equation (4.1), the efflux velocity is evaluated. Therefore, given the efflux velocity, both the longitudinal and transversal components of the axial velocity at the seabed level can be easily computed according to the formulations expressed in Equation (4.26). In particular, if the distance from the propeller, placed at the stern of the vessel, is lower than $D_p/2c_p$, the first relation will be used. On the contrary, if that distance is bigger than

$D_p/2c_p$, then the second formulation are respectively used. Otherwise, when the x distance is negative, e.g. towards the bow, the scheme is not implemented and no contribution is given by the propeller.

- *Step 2: Computation of the propeller-induced friction velocity*

  Consequently, once evaluated the module of the axial velocity on the seabed, it is possible to compute the corresponding friction velocity distribution using Equation (4.27). Therefore, this contribution is passed to the sediment transport module and added to the original shear velocity for the definition of the total shear velocity (4.30).

- *Step 3: Computation of the propeller-induced bed shear stress*

  The additional bed shear stress due to the propeller effect is introduced in the definition of the total bed shear stress, as described by Equation (4.28). The morphological changes of the seabed are computed using Equation (4.13).

In case of multiple vessels, the same procedure would be adopted for each one.
It is important to underline that the model is not yet capable to reach an equilibrium, since the hydrodynamics has not been modified when implementing the propeller effects, causing the erosion of all the sediments on the seabed. Obviously, this is not realistic. Further investigations need to be carried out to couple the hydrodynamic and the propeller modules.

## 4.3 Numerical runs for the ship propeller effect

Numerical simulations with a single vessel in a narrow channel have been perforemed to study the influence of the propeller implementation on the morphodynamics.

The modelled vessel has a length of 116.95 m, a width of 16.96 m and a draught of 4.34 m. A single propeller has been assumed, having a diameter equal to 3.7 m, summarized in Table 4.3. These are typical dimensions of a frigate of the Italian Navy fleet, in particular belonging to the Maestrale class. All the coefficients and technical information explained below and related to this vessel have provided by the Italian Navy. The computational domain has been assumed 1000 m long and 100 m wide, to provide enough free space between the ship and the domain boundaries, with a spatial resolution of 1 m in x and y. A sponge layer of 10 m was applied on the north, east, west and south boundaries to simulate absorbing boundaries. Due to the nature of the focal processes, no waves or external currents have been included in the numerical runs.

The water depth has been uniform and equal to 5.0 m. The bathymetry has been characterized by a flat seabed of coarse sand (non-cohesive) with a medium grain size of 0.5 mm. The values of relevant morphodynamic parameters are: critical bed Shields parameter, $\theta_b = 0.047$, sediment porosity $n_s = 0.47$, settling velocity $w_s = 0.0125\ m/s$, slope of repose angle $\tan\phi = 0.7$ (corresponding to a repose angle of 35°) and density ratio $s = 2.68$. A morphological step (ratio between the morphological updating step to the Boussinesq model time step) of 10 has been applied, recommended for the ship-wake applications [58].

The duration of the numerical runs is 10 minutes, with an output interval of 10 seconds. The adaptive time step has been automatically computed by FUNWAVE, on the basis of the Courante-Friedrichs-Levy (CFL) number restriction, which has been set to 0.1.

The value of the dimensionless thrust coefficient $C_t$ has been derived from the Wageningen B-series [64]. The thrust coefficient has been evaluated on case by case basis, since it depends on the advance speed $v_a$ (espressed as a percentage of the ship speed through the wake fraction coefficient). The advance speed is related to the advance coefficient $J_a$ by the relation:

$$J_a = \frac{v_a}{nD_p} \tag{4.32}$$

Table 4.3: Summary of vessel and propeller characteristics.

| **Property** | **Value** |
|---|---|
| Ship length L | 116.95 (m) |
| Ship beam W | 16.96 (m) |
| Ship draught P | 4.34 (m) |
| Propeller diameter $D_p$ | 3.7 (m) |

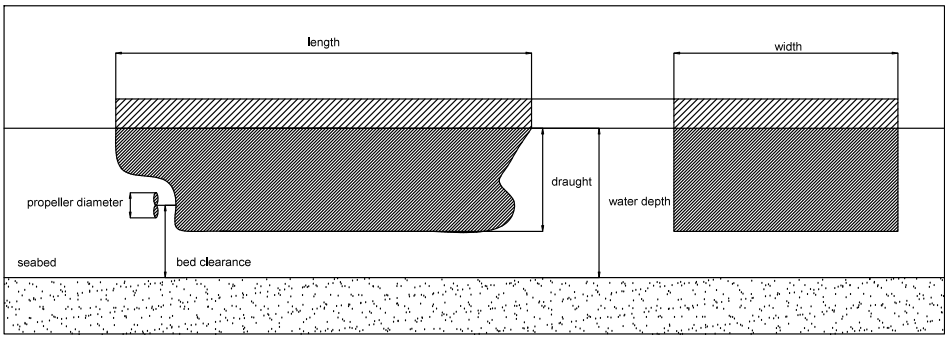


Figure 4.4: Sketch of the principle dimensions of the vessel.

In particular, the Wageningen B-series characterized by $A_e/A_0 = 0.55$ ($A_e$ is the propeller expanded area and $A_0$ the propeller disk area) for a propeller with 5 blades has been considered, although in this model the number of blades is not taken into account.

The bed clearance has been chosen both to reduce the vibrations induced by the propeller on the hull (minimum value suggested equal to $0.3D_p$) and to satisfy the range of validity (maximum ratio $D_p/h_p$ equal to 1.2) of Maynord expression [47] used in the definition of the friction coefficient. Considering the limited under keel clearance, the deep draught option has been activated (see Subsection 4.2.1.2). The combined shock capturing method and friction method has been used, adopting the default values for both the viscosity and friction coefficients.

The performed numerical runs for the steady and the moving vessel are listed full in the following tables, respectevely Table 4.4 for the former and Table 4.5 for the latter. For the steady cases, characterized by zero advance velocity, we have investigated the influence of the revolution number and the bed clearance on the morphology. For the runs related to the moving vessel, instead, the revolution speed has been adequately chosen to obtain the required speeds, between 2 and 4 knots, commonly adopted in most of the navigation channels. As mentioned before, for this preliminary study, any other additional forcings have not been included in the numerical runs. This situation might represent the condition in which the ship is entering/leaving the harbour basin to/from the moorings in still water conditions.

In the literature, the majority of the studies have been traditionally conducted at no speed advance, i.e. in bollard pull conditions, considering that the most relevant velocities at the bottom are reached when the ship is stationary. In addition, the vessel stationary condition will give a more conservative answer in a design context, hence it is preferred. Even though it was confirmed that the propeller jet contribution on the bed topography decreases at the increasing of the speed advance [21], simulating the case of the moving vessel might be of particular interest since it occurs when the ship leaves/approaches the moorings.

Table 4.4: Overview of numerical runs for the steady vessel.

| Case | Vessel speed (kn) | $n$ (rev/s) | $h_p$ (m) | $C_t$ |
|---|---|---|---|---|
| Run0 | 0 | 0.4 | 3.5 | 0.5 |
| Run1 | 0 | 0.8 | 3.5 | 0.5 |
| Run2 | 0 | 1.2 | 3.5 | 0.5 |
| Run3 | 0 | 1.6 | 3.5 | 0.5 |
| Run4 | 0 | 2.0 | 3.5 | 0.5 |
| Run5 | 0 | 1.2 | 3.0 | 0.5 |
| Run6 | 0 | 1.2 | 4.0 | 0.5 |

Table 4.5: Overview of numerical runs for the moving vessel.

| Case | Vessel speed (kn) | $n$ (rev/s) | $h_p$ (m) |
|---|---|---|---|
| Run0m | 1 | 0.4 | 3.5 |
| Run1m | 2 | 0.8 | 3.5 |
| Run2m | 3 | 1.2 | 3.5 |
| Run3m | 4 | 1.6 | 3.5 |

## 4.4 Numerical results on the ship propeller effect

### 4.4.1 Numerical results on the ship propeller effect: the steady vessel case

Figure 4.5 depicts the velocity field on the seabed for a steady vessel for the specific test case *Run3* (see Table 4.4), taken as illustrative of the main features of the flow at hand. The arrows give the velocity direction, while the intensity is given by the colormap. The black rectangle represents the stern area of the vessel, where the propeller is located. It clearly shows the two zones behind the vessel, highlighted by the two black dashed lines, the ZFE and the ZEF. In the zone of flow establishment, located between the two dashed lined of Figure 4.6, close to the propeller face and characterized by a length of $x = D_p/2c_p$, the velocity is constant along the x direction since we have considered that, like for the axial velocity, no decay of the seabed maximum velocity along the x-direction occurred in this area. In the zone of established flow, instead, Figure 4.6 confirms that the maximum velocity, almost twice larger than in the ZFE, is achieved at the central axis. As highlighted by the vectors, the velocity gradually decays moving away from the vessel, linearly in x and exponentially in y.

For the *Run3* case (see Table 4.4), the morphological changes induced, respectively, by the suspended load (top panel), the bedload (middle panel) and by the total load (bottom panel), i.e. the sum of the suspended load and the bedload, at the end of the simulation are depicted in Figure 4.7. The blue and red colors respectively indicate the erosion and accumulation areas from the original depth.

The top panel shows that sediments behind the vessel are progressively stirred up from the seabed by the rotation of propeller, generating erosion. The continuous rotation of the propeller is reflected in the consequent growth of the eroded area due to the dispersion processes, expanded laterally and reflecting the velocity pattern. Also, it develops downstream, up to a maximum length of $D_p$. The morphological evolution due to the bedload contribution is shown in the middle panel. Here, at the end of the simulation, it is clearly visible the presence of two distinct scour regions: a main scour hole (in dark blue) behind the propeller, defined as primary scour hole, approximately at a distance of $2D_p$ from the bow of the vessel (depicted in black in Figure 4.7) and a secondary minor hole (in light blue) directly beneath the propeller. The primary scour hole propagates downstream for almost a lenght of $D_p$, causing

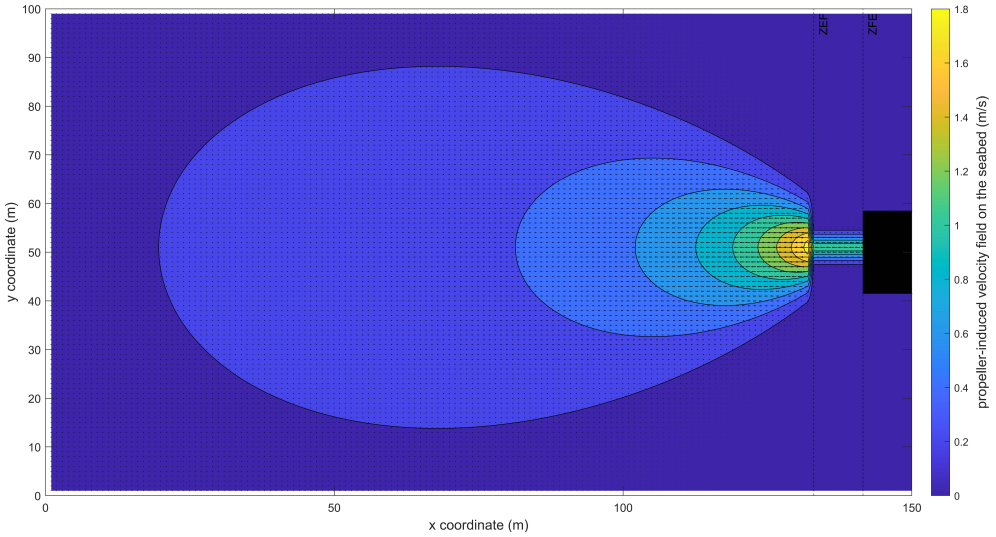


Figure 4.5: Velocity field on the seabed induced by the propeller for the case *Run3*.

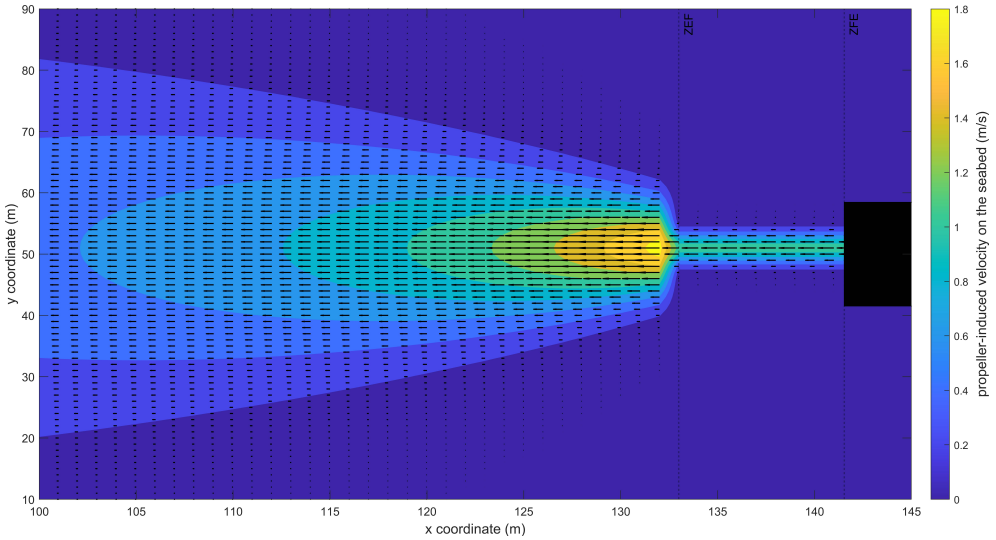


Figure 4.6: Close-up view of the area close to the propeller.

a deposition mound (in red) behind of it. In the bottom panel, the overall effect of the total load, i.e. induced by both the suspended and the bedload, on the seabed variation are illustrated. For this test case, characterized by a sandy bathymetry, it is possible to state that the bedload effect prevailes over the suspended load, governing the morphological evolution of the seabed. As a result, the erosion induced by the former twice bigger than that generated by the latter. However, the suspended load mainly contributes in increasing the main scour hole (slightly the secondary hole) and in eroding the deposition mound behind it, making it less steep. It is important to underline that, in the following, in order to compare our results to the experimental studies in the literature, it has been preferred to focus on the bedload contribution. This is due to the fact that, as pointed out also in [57], the majority of the studies employed sand materials of different median sediment diameters. Consequently, the experimental investigations related the propeller scour could primarly capture the effect of the bedload, rather than the suspended load effects. Moreover, in the following the evolution of the bedload-induced scour progress has been analyzed through the definition of the typical dimensions of the scour holes:

- $l_s$, the length of the main scour hole (extension along the x-axis)
- $d_s$, the depth of the main scour hole

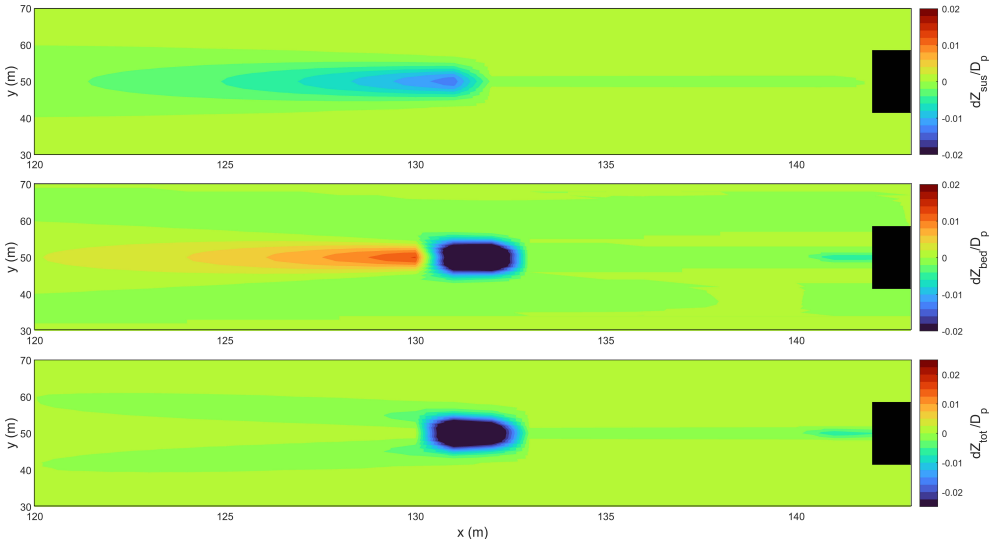


Figure 4.7: Seabed morphological changes in non-dimensional form (dZ/Dp) due to the suspended load (top panel), bedload (middle panel) and the total load (bottom panel) for the steady case.

– $w_s$, the width of the main scour hole (extension along the y-axis)

The length of the scour holes has been normalized with respect to the length of the ship $l_s/D_p$, while the depths and the widths have been scaled to the propeller diameter, getting $d_s/D_p$ and $w_s/D_p$. An additional numerical test, lasting 30 minutes, has been run to observe the temporal evolution of the scour holes and the deposition height downstream. Figure **??** and Figure 4.9 show respectevely the modelled temporal development of the normalized plan scour profile $d_s/D_p$ along the centerline of the propeller, due to the suspended load and the bedload, the main responsible for the morphological evolution of the bottom. In the x axis is represented the longitudinal distance from the propeller, whose location is indicated by the arrow. Each panel represents the growth of the two scour holes and the accumulation zone, respectively depicted in blue and in yellow, every five minutes. For sake of simplicity, in the panels are illustrated only two levels of the non-dimensional scour depth, corresponding to -0.001 (erosion) and 0.001 (accretion). In Figure **??** the eroded area and the consequent lateral accumulation zone increase gradually with time, reaching their maximum sizes after 30 minutes. Similarly, in Figure 4.9 it is possible to observe that the width and the length of the main scour increased progressively during the simulation, reaching its maximum values after 30 minutes. In particular, $w_s$, i.e. the width of the maximum scour, is found to be around $5D_p$ at the end of the simulation. On the contrary, the width of the accumulation seems to slightly extend, while its length is expanding downstream during the whole duration of the numerical run.

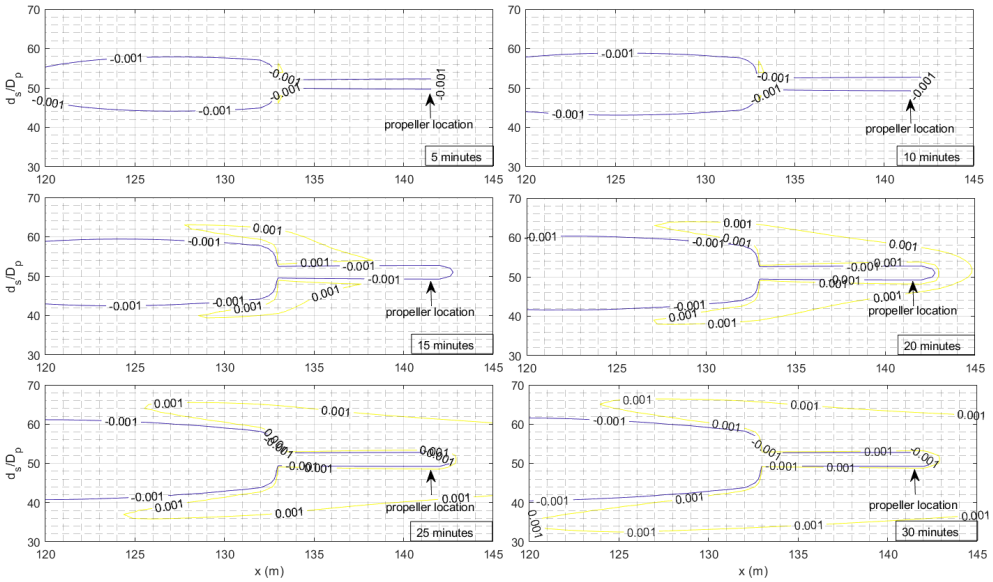


Figure 4.8: Modelled temporal development of the normalized plan scour profiles along the propeller centerline due to the suspended load for the case *Run3*.

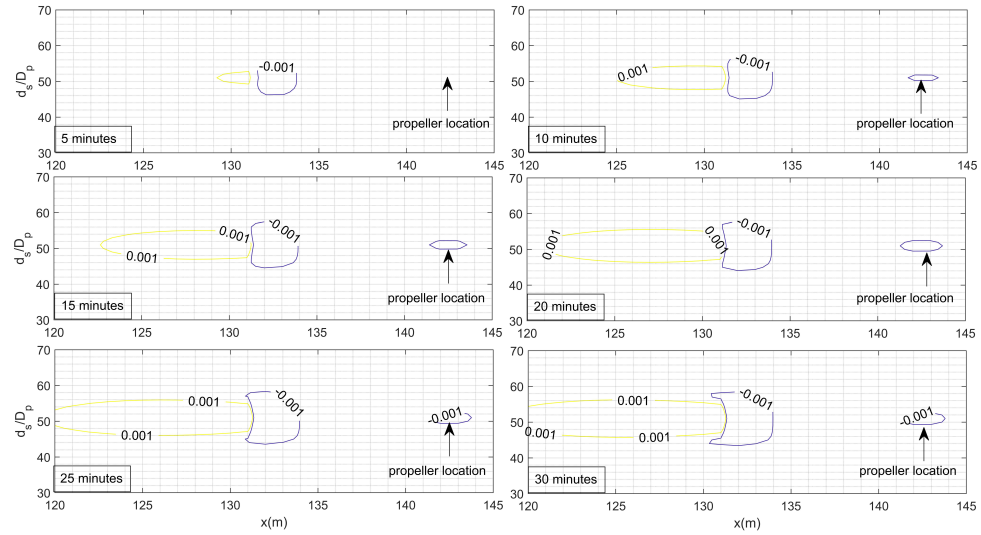


Figure 4.9: Modelled temporal development of the normalized plan scour profiles along the propeller centerline due to the bedload for the case *Run3*.

In Figure 4.8 and Figure 4.11 the suspended load-induced and the bedload-induced scour profile progression during the simulation are given. Figure 4.8 shows that the propeller rotation generates erosion reflecting the nearbed velocity profile. This eroded area tends to grow in time and contributes to enhance the total scour. Additionally, it also plays a role in eroding the deposition mound created by the bedload.

Figure 4.11 reveals that, at the initial stage of the simulation, the first scour to appear is the primary hole, at a distance from the propeller approximately equal to $3D_p$. Also, a small amount of sediment downstream begins to accumulate. Both the depth of the scours and of the deposition mound tends to increase in time. Simultaneously, the dune downstream the main scour hole starts to form, as well as the secondary scour, upstream in proximity to the propeller location.

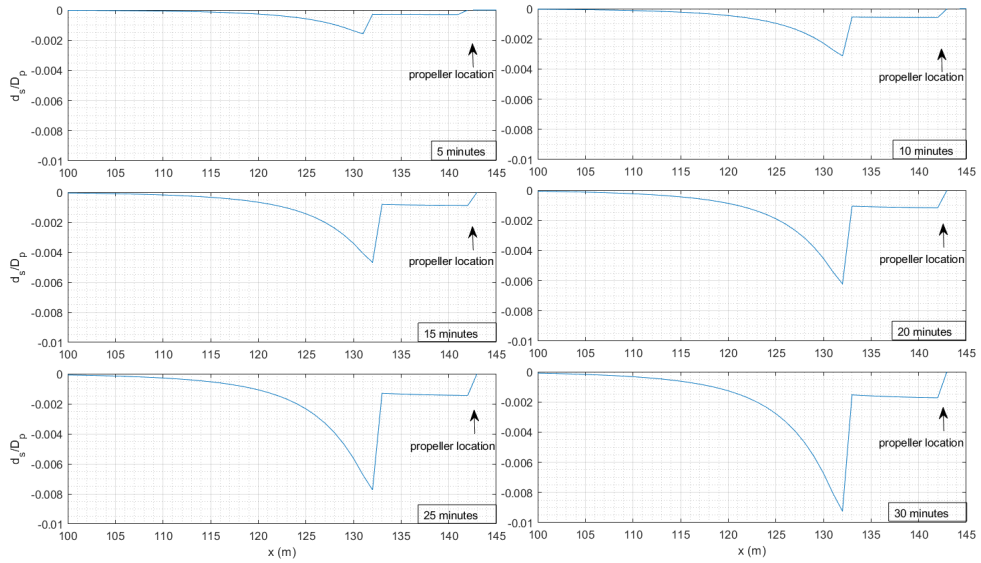


Figure 4.10: Modelled temporal development of the normalized scour profiles progression along the propeller centerline due to the suspended load for the case *Run3*.

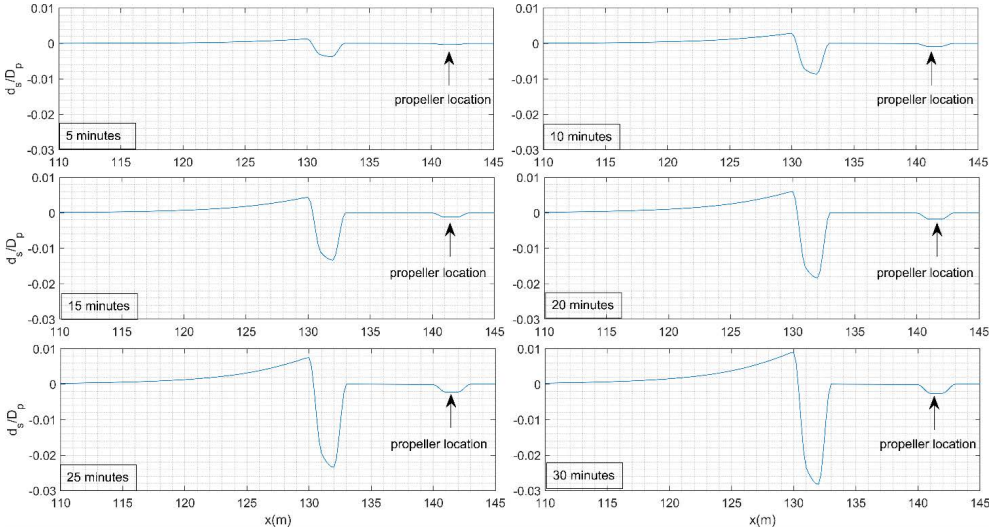


Figure 4.11: Modelled temporal development of the normalized scour profiles progression along the propeller centerline due to the bedload for the case *Run3*.

Finally, it has been evaluated the dependency of the non-dimensional maximum scour depth on the number of revolutions. Figure 4.12 shows the non-dimensional maximum scour depths due to the total load, indicated by the black bullets in y, for increasing number of revolutions, in x. In particular, the modelled values can be interpolated using an exponential function ($f(x) = aexp(bx)$, with a = 0.015 and b = 1.91), with a coefficient of determination $R^2$ equal to 0.98, confirming an exponential law existing between the revolution speed and the scour depths.

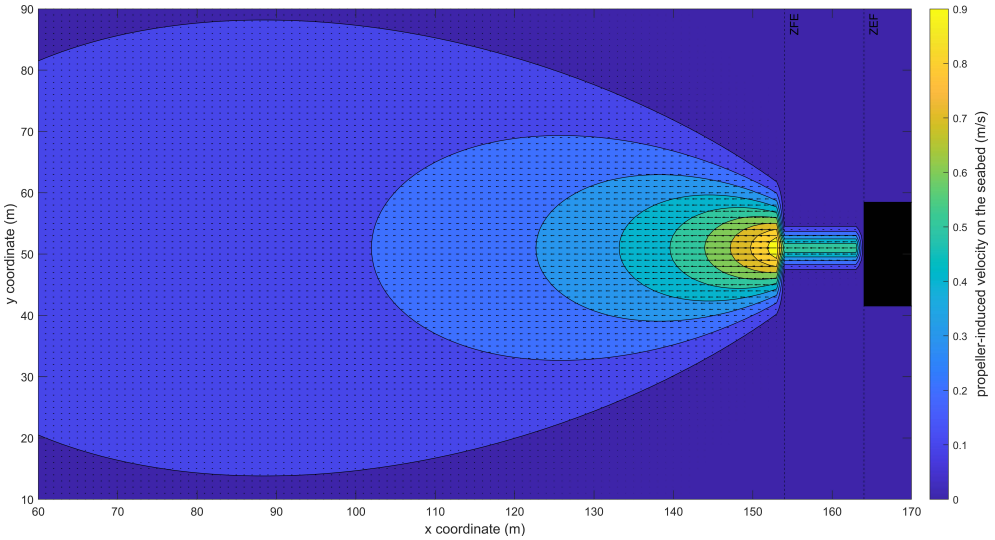


Figure 4.13: Velocity field on the seabed induced by the propeller for the case *Run3m*.

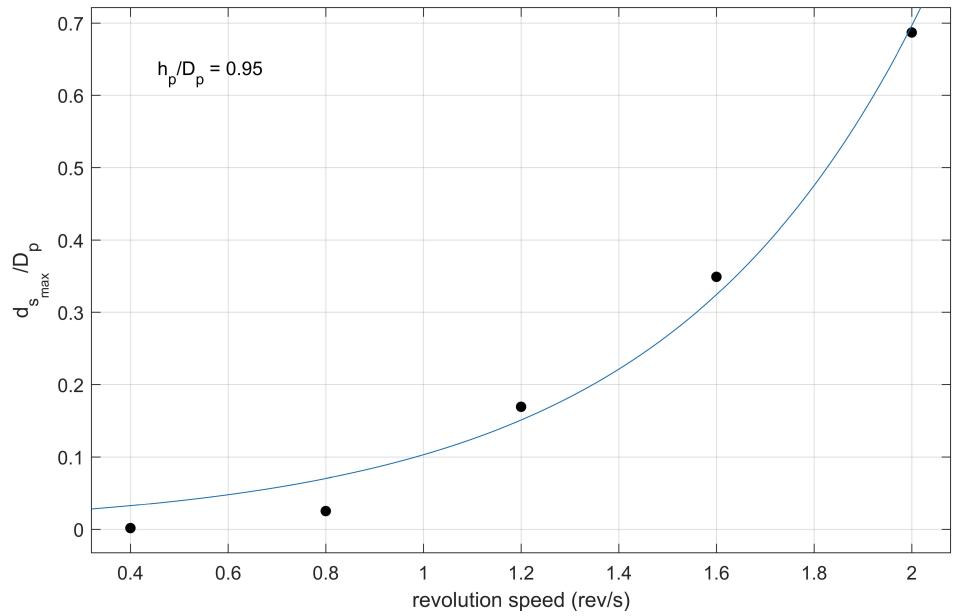


Figure 4.12: Dependency of the total load scour on the revolutions number for the steady vessel cases.

### 4.4.2 Numerical results on the ship propeller effect: the moving vessel case

Figure 4.13 displays the velocity field induced by the propeller when the ship is moving with a speed of 3 knots is similar to the case *Run3m*, depicted in Figure 4.5, characterised by the same revolution speed. The flow pattern is the same, but with lower magnitudes in the ZFE and the ZEF, due to the slightly difference in the thrust coefficient $C_t$.

Figures 4.15 and 4.14 show the morphological evolution of the seabed for the cases *Run0m* and *Run3m*.

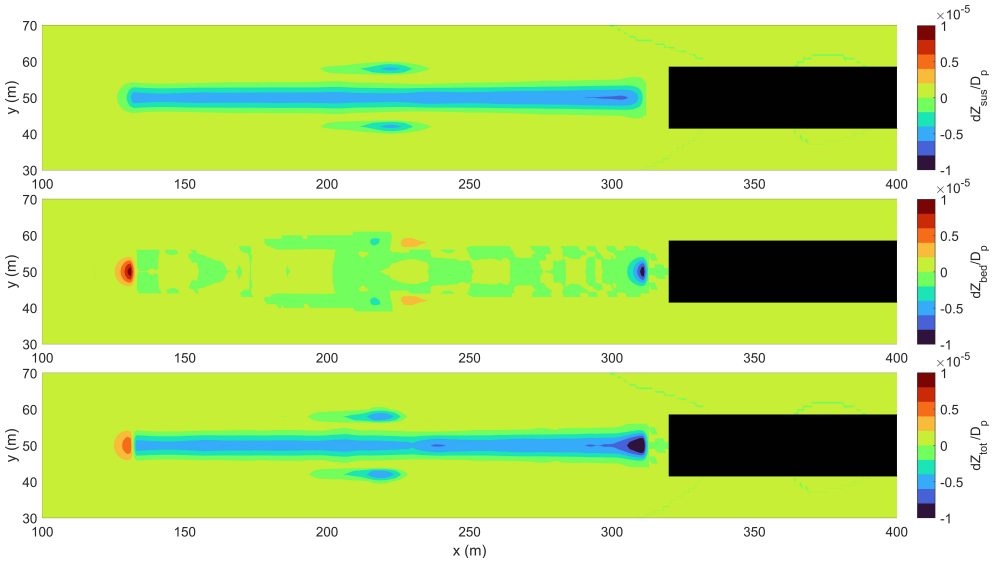


Figure 4.14: Seabed morphological changes in the non-dimensional form (dZ/Dp) due to the suspended load (top panel), bedload (middle panel) and the total load sum (bottom panel) for the case *Run0m*.

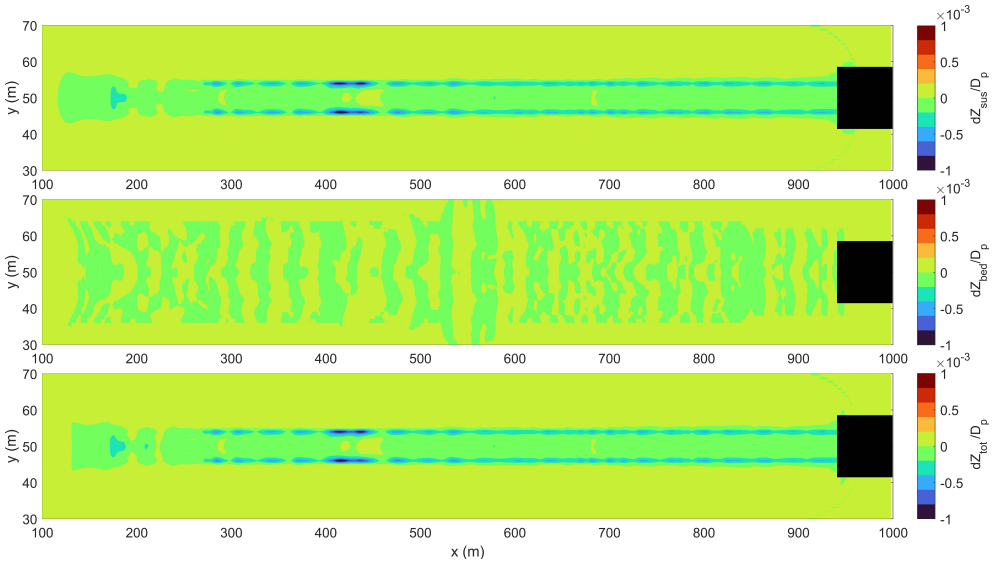


Figure 4.15: Seabed morphological changes in the non-dimensional form (dZ/Dp) due to the suspended load (top panel), bedload (middle panel) and the total load sum (bottom panel) for the case *Run3m*.

Similarly to the steady case, the top, the middle and the bottom panels respectively refer to the suspended-induced, the bedload-induced and the total effect on the seabed elevation at end of the simulation. The initial position of the ship, referred to the middle of the vessel's length, has been fixed at 200 m, while the final position has been computed according to the ship speed after 360 s. In general, it is possible to state that, unlike the steady case, the suspended load prevailes over the bedload, governing the morphological evolution of the seabed when the ship is moving. Results, in fact, have shown small bedload fluxes along the channel, this causing limited bedload-induced changes, mainly occuring at the final position reached by the vessel. A deposition, instead, can be observed when the ship starts moving, balancing the initial scour hole. On the other hand, the contribution of the suspended load is much stronger when the ship reaches its speed of advance.

Figure 4.16 compares the suspended sediment concentration without (top panel) and with (bottom panel) propeller implementation. The concentration is significantly

higher when the propeller effect is included, confirming it plays an important role in the resuspension of the sediments lying on the seabed.

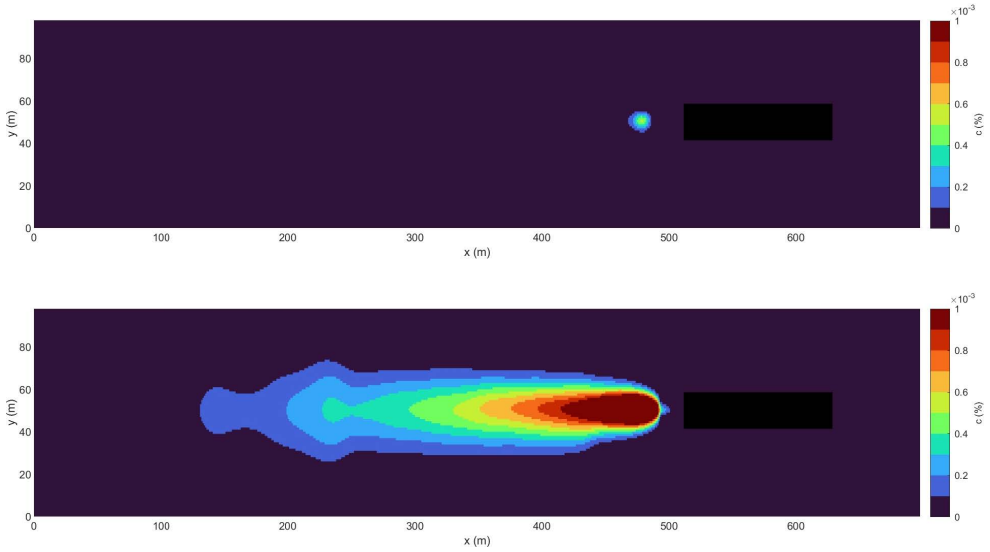


Figure 4.16: Comparison between the concentration without (top panel) and with (bottom panel) the propeller implementation.

As in the stationary cases, the variation of the non-dimensional scour depth with respect to the number of revolutions has been evaluated in Figure 4.17. In Figure 4.17 are depicted the non-dimensional maximum scour depths for the cases *Run0m-Run3m*, in y, and the corresponding number of revolutions, in x. Similarly to the steady cases, the modelled values are well fitted by the exponential curve in blue ($f(x) = aexp(bx)$, with a = $2.7{\cdot}10^{-5}$ and b = 3.09), with a coefficient of determination $R^2$ equal to 0.98. Although the values are strongly lower that the cases *Run0-Run4*, the same relation has been identified between the revolution speed and the scour depth quantities for tests perfomed with moving vessel.

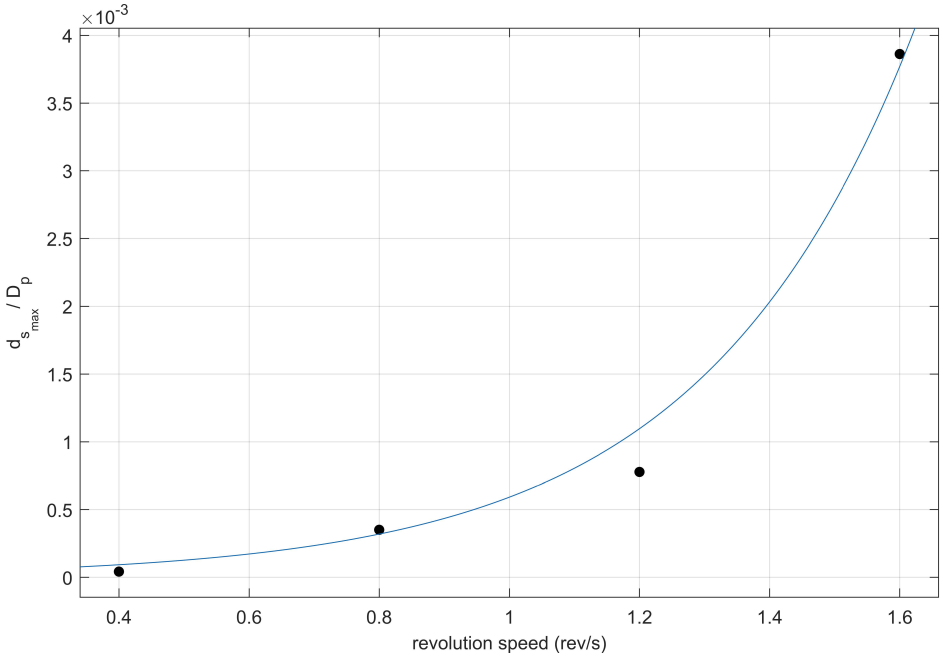


Figure 4.17: Dependency of the scour on the revolutions number for the moving vessel case.

# Chapter 5

# Discussion on the sediment transport induced by natural forcings

The Arsenale represents a unique case study for many reasons. Firstly, it is located in the La Spezia gulf, an area sheltered by its natural shape and also protected by the outer breakwater. In addition, some breakwaters separate the military area of the Arsenale from the commercial and touristic zone, delimiting a closed basin. Secondly, another peculiarity of this site is the presence of two freshwater inlets, i.e., the LR, flowing close to the northern gate, and the CR, debouching directly into the basin; these ensure the water exchange between the sea and the basin. Thirdly, it is characterized by deep waters. For all these reasons, the water system the Arsenale harbour is placed in cannot be easily placed into the existing literature classification **??**. Hence, this work was addressed at comprehending the interaction of the different mechanisms induced by all the forcings occurring in such a complex environment.

Numerical simulations have revealed that the main forcings responsible for the water and sediment circulation and exchanges at the Arsenale inlets are: (1) the wind, (2) the freshwater stream-induced flows, and (3) the tidal filling and emptying.

## 5.1 Wave effect

The FUNWAVE simulations clearly showed that, despite the fact that the outer domain was forced by extreme wind waves associated with a 100-year return period, the wave heights in the Arsenale were very low due to the natural shape of the gulf of La Spezia and the breakwaters, which sheltered the area. Therefore, as expected, the influence of the waves was very weak compared to the other forcing analysed. The effect exerted by the waves could be clearly distinguished by comparing the TR and TWR scenarios, which differed only with regard to the wave implementation (which was neglected in the TR scenario). The flow patterns revealed that the velocities around the LR entrance and that of the LR jet were smaller in the TWR scenario (compare Figure 3.5 with Figure 3.8). The waves, albeit minimally, tended to oppose the LR discharge, slowing down its offshore spreading and favouring its propagation into the Arsenale.

Although the Arsenale configuration might be similar to that of an enclosed basin, and thus unlike that of stagnant waters or shallow lakes, here the effect of wind waves was found to be very weak. In shallow lakes, like the two marinas in Lake Loosdrecth studied by Winterwerp [75], or lagoons, like the Marano and Grado Lagoon [6] or the Venice Lagoon, which are characterized by stagnant and shallow waters, waves can resuspend sediments on the seabed in calm weather conditions. Conversely, in the Arsenale the sed-iment transport, in terms of resuspension and deposition, was not affected by the waves. This is due to the evolution of very small waves inside the basin as a result of the limited fetch of La Spezia Bay and of the Arsenale itself,

which is constrained by the presence of the breakwaters, and also to the higher water depths characterizing the area. In fact, the TW scenario showed how the critical bed shear stress for erosion, due to tidal and wave forcing, was exceeded rarely and briefly, following the maximum velocities induced by the narrowing of the section of the LR entrance, in relation to the ebb tide. This implied that the forcing was not intense enough to stir up sediments on the seabed and to induce sediment transport processes.

## 5.2 Wind effect

The results of the TW scenario plainly highlighted the role of the tide and the wind in a microtidal environment that is sheltered and characterized by a weak wave agitation. In closed basins, like shallow lakes or a lagoon harbour, the wind strongly affects the hydrodynamics [77], [65]. We also observed that a semi-enclosed basin, protected by breakwaters like the Arsenale and characterized by higher water depths, had similar behaviour. To further confirm this, we ran an additional numerical simulation with no wind, forced only by the rivers' discharges and tide. We did not include the waves since they had a secondary role in the observed processes. The results of this additional scenario confirmed the primary role of the wind: when no wind was blowing into the basin, no circulation cell appeared (third column of Figure 5.1). Moreover, the wind direction influenced the rotation of the main circulation: northeasterly winds generated a counterclockwise eddy, whilst a clockwise eddy developed under southeasterly winds (in first and second columns of Figure 5.1, respectively). As expected, the velocities inside the basin were one order of magnitude stronger in the presence of the wind forcing with a return period of 100 years. Neglecting it, the flow pattern was only influenced by the tide, with velocities directed toward the WSW/ESE, respectively, when the tide entered/exited the Arsenale. The top row of Figure 5.1 shows the circulation inside the Arsenale during the tidal filling. The tide entering the basin tended to create an anticlockwise vortex. As the circulation was already counter-clockwise, as forced by the NNE wind, the vortex did not develop. When the tide decreased (bottom row of Figure 5.1), the water flowed out of the basin and the velocities increased, reaching maximum values at the LR entrance. Similar findings were also observed by De Marchis et al. [14] in the Augusta harbour (Sicily), which has a configuration very similar to that of the Arsenale, being sheltered by three breakwaters and connected to the open sea through two entrances.

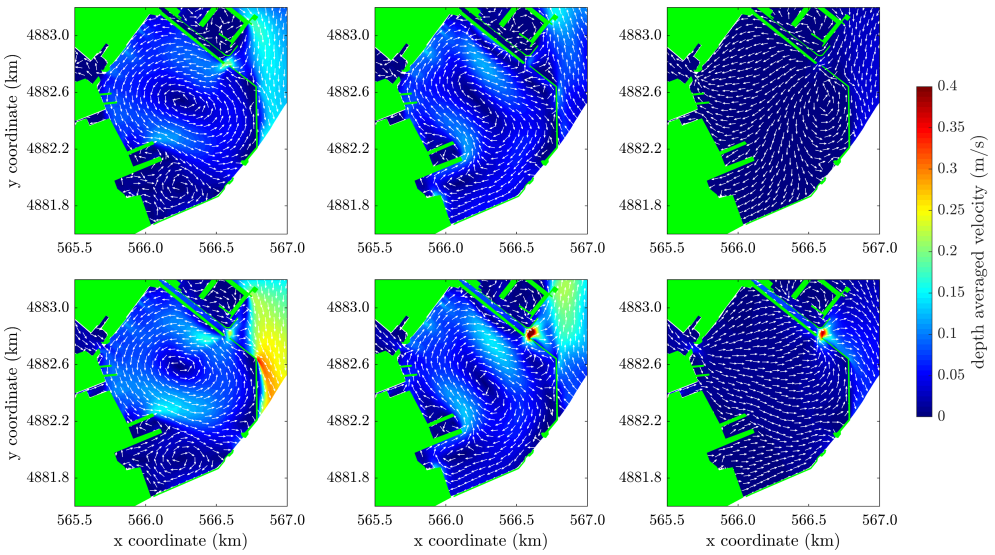


Figure 5.1: Modelled depth-averaged velocities for NNE wind (first column), SSE wind (second column), and no wind (third column) at tidal filling (top row) and emptying (bottom row)

The mean suspended sediment transport, as shown in Figure 5.2, generally matched

the hydrodynamic patterns triggered by the wind, i.e., the circulation cell (first and second panels). In addition, the influence of the two freshwater streams was clear and caused the largest sediment transport intensities. The NNE wind pushed the LR discharge inside the Arsenale more than the SSE wind, thus causing a larger sediment transport. For the case without wind, the sediments either flowed out of the main entrance of the Arsenale or deposited just outside of the CR (third panel of Figure 5.2). Moreover, all the panels of Figure 5.2 show that at the southern mouth of the Arsenale the sediment transport was large and directed toward the sea. This means that part of the sediment escaped the Arsenale, and this is the likely reason for the reduced amount of sedimentation. The deposition patterns were affected by the direction, with the SSE winds causing larger sediment accumulation in the northeastern part of the basin (compare, for example, the right and left panels of Figure 3.10). The water level range was also affected by the wind forcing. Figure 5.3 shows the water level difference between the scenarios carried out with and without wind, after 8 h of simulations, when the wind field was fully developed. Depending on the wind direction, an increase in water level was noticed in different areas of the Arsenale: a surge in the southwestern and northeastern part of the Arsenale was observed for the wind blowing from the NNE and SSE, respectively. The surge was larger for the SSE wind, both because of the higher wind speed and because the water was pushed to the northeast area of the Arsenale, where it tended to accumulate. Conversely, the NNE wind gave a smaller surge because the water could flow out of the main Arsenale mouth. Similar findings were also observed in the Venice Lagoon, which presented set-up and set-down values of 0.55 m and -0.45 m, respectively, under a strong northeast wind [77]. The surge amount for the Venice Lagoon was large because the wind blew along the major axis of the basin, which extends for around 50 km. Conversely, the Arsenale extends for about 1.5 km and 1.2 km in the north and east directions, respectively, thus limiting the fetch and wind effects. Moreover, the Lagoon is shallower than the Arsenale, with water depths of around 1 m, thus making the environment more subject to the wind action. Even though it was small, the surge created by the wind inside the Arsenale contributed to the global circulation cell, which was continuously fed by the steady wind action.

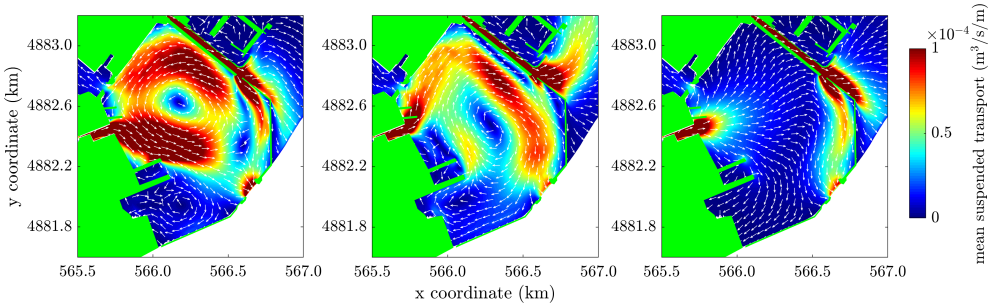


Figure 5.2: Mean suspended sediment transport for the TR scenario in case of NNE wind (first panel), SSE wind (second panel), and no wind (third panel). The intensity is given by the colour bar, while the direction is represented by the arrows.

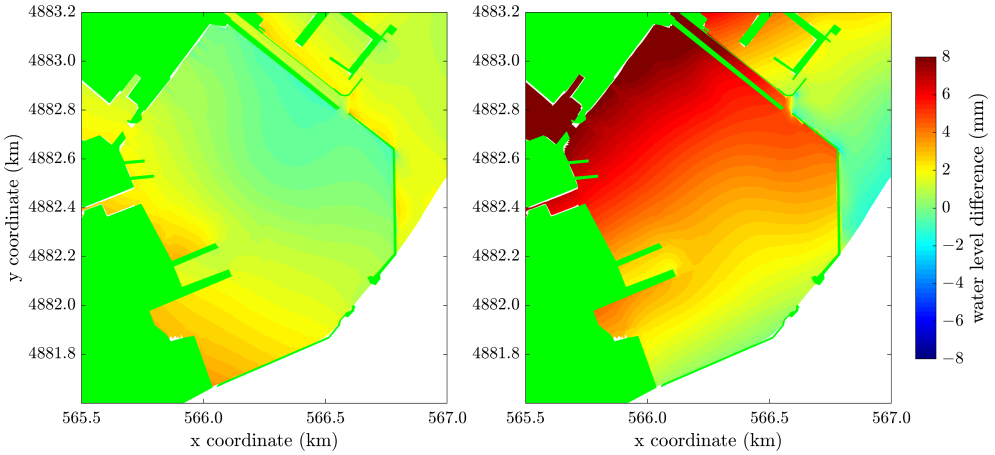


Figure 5.3: Water level differences between the cases with NNE wind and with no wind (left panel) and the cases with SSE wind and no wind (right panel).

## 5.3 Tide effect

When neglecting the contribution of external sources, i.e., the LR and CR freshwater discharges, the water exchange between the sea and the Arsenale was due mainly to the tidal cyclic pumping. During the flood flow, the water entered the Arsenale basin due to rising of the water level. Conversely, during the ebb flow, the water left the Arsenale basin because of the lowering of the water level. When the contribution of the freshwater streams was included, the tidal currents interacted with the discharges, particularly with the LR. The simulations showed that the tidal filling of the basin enhanced the development of the LR-generated eddy at the entrance, while, conversely, the emptying of the basin retarded or impeded its generation. This behaviour was also observed in some laboratory experiments performed by Langedoen et al. [38]. The tide also determined the velocity oscillations, reflecting the tidal ebb and flood. After the tidal filling, the ebb phase forced the water inside the Arsenale basin to pass through the LR entrance, where, as a result of the section width reduction, maximum velocities were reached. At the LR entrance, even before the increasing of the rivers' discharges, i.e., when the tide was the main forcing action, the bed shear stress exceeded the critical value for erosion, but for very short periods of time. This was not enough to force seabed sediment resuspension; therefore, the tide did not generate any sediment transport, probably due to the large ratio between the water depth in the Arsenale and the tidal excursion. Conversely, in very shallow microtidal environments, like that of the Venice Lagoon, where such a ratio is smaller, Carniello et al. [10] observed that the tide action caused sediment resuspension, with turbidity peaks occurring simultaneously with the ebb tide. Moreover, the author pointed out that the sediment that left the lagoon during the ebb phase of the tide did not enter again during the flood phase. Such tidal asymmetry was also observed in tidally dominated embayments, like that of the Boston harbour [59]: the velocity with which water and sediment leave the basin during the ebb phase is larger than the speed with which they enter at the flood phase, causing the flushing of the harbour. We also observed some "flushing", but it was caused by the geometrical characteristics of the Arsenale: some of the sediment, released inside the basin by the rivers, escapes from the main entrance; this is probably one of the reasons for the small sedimentation rate modelled by the simulations.

## 5.4 Freshwater Stream Effect

The results of the TR and TWR scenarios were very similar and highlighted the contribution of the rivers' discharges to the exchange mechanisms that characterize the Arsenale hydrodynamics. The LR significantly contributed to the horizontal

entrainment process. The inflow angle between the river and the LR entrance is 90°. As already observed, before the occurrence of the river discharge, the NNE wind forced a large counterclockwise, quasi-steady eddy in the domain (upper left panel of Figure 5.4). During the LR discharge rise phase, which is a result of the shearing between the Arsenale and the LR flow (thus giving a clear mixing layer), a recirculating flow was driven. An eddy was generated at the upstream corner of the LR entrance, growing in size in the direction parallel to the river flow, reaching its maximum dimension at the discharge peak, while its centre was pushed to the southwestern part of the harbour. There, part of the flux was dispersed, flowing out through the southwestern mouth (red lines in bottom left panel of Figure 5.4). A similar evolution of the eddy was also observed in the work of Langedoen et al. [38] for a square closed basin, characterized by a ratio between the width of the harbour mouth and the harbour length of 2, with the river flowing along the harbour entrance. Then, the fall of the river discharge restored the initial situation. The CR, however, flowing directly into the Arsenale, contributed to the wind-induced circulation (green lines in the bottom left panel of Figure 5.4). The SSE wind, on the other hand, induced a clockwise quasi-steady vortex extending to the whole domain (upper right panel of Figure 5.4). In contrast to the previous case, the increase in the rivers' discharges did not generate eddies. In fact, both the LR and the CR joined the general circulation cell, contributing to its intensity (bottom right panel of Figure 5.4). Moreover, the SSE wind limited the entrance of LR flow into the Arsenale.

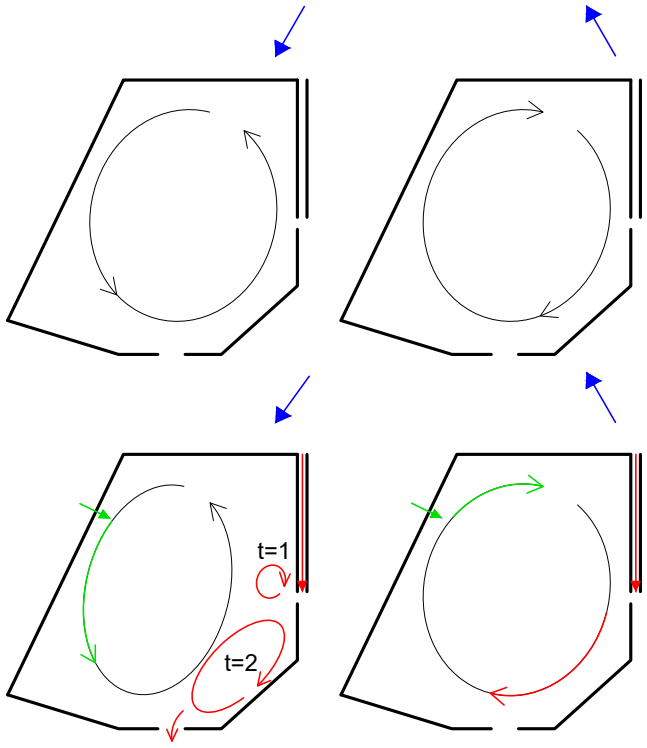


Figure 5.4: Sketch of the circulation for NNE wind (left panels) and for SSE wind (right panels), before and after the occurrence of the river discharges (upper and bottom rows, respectively. The blue, green, and red arrows indicate the wind direction, the CR flow, and the LR flow, respectively.

Our numerical simulations proved that the sediments were carried into the Arsenale by the rivers and advected by the rivers' flows. Therefore, we can safely claim that the riverine inlets were mainly responsible for the supply of fine, cohesive material within the Arsenale basin. This trend was also confirmed in the work on the siltation of the Nowshahr port [44]. Here, the wind-driven circulation was so intense that it carried the sediments from the rivers' mouths towards the entrance of Nowshahr

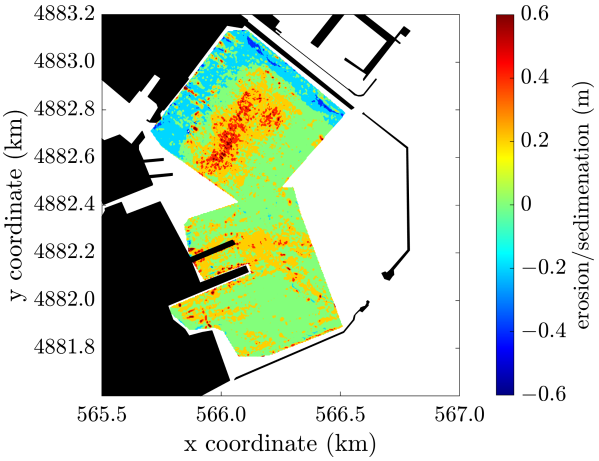


Figure 5.5: Difference between the surveys performed within the Arsenale in 2013 and 2016. Negative and positive values represent erosion and deposition, respectively.

port. Unlike macrotidal harbour settings, where the largest amount of sediment could be brought into the basin by the flood tide [40], or wave-dominated environments, where wave-driven currents may cause sediment resuspension [12] and transport inside the harbour [49] in the Arsenale microtidal basin protected from waves, neither the tide nor the waves are capable of triggering sediment resuspension. The only forcing that erodes the riverbed and mobilizes the sediments is the river discharge. In fact, along the LR channel and in the area of the CR mouth, the critical bed shear stress for erosion progressively increased in response to the intensification of the rivers' discharges. Despite the supply of sediment from the rivers, we found that the maximum sedimentation in the Arsenale was not significant, reaching 3 cm at the most during the events ana-lysed because a considerable portion of suspended sediments left the basin through the southern, main entrance. The comparison between two surveys carried out in 2013 and 2016 (Figure 5.5) confirmed that the deposition inside the Arsenale area is not so large, reaching 50 cm only at some locations in the innermost part of the basin, where the modelled sedimentation also occurred. The amount of accumulation that occurred in three years corresponds to an average of 15 cm per year, which is reasonably consistent with our simulation results, which showed a 3 cm deposition following a 100-year return period event.

# Chapter 6

# Discussion on the sediment transport induced by ship propellers

## 6.1 Discussion on the hydro-morphodynamics induced by the propeller: the steady vessel case

### 6.1.1 Velocity field induced by the propeller jet for the steady vessel case

As shown in Figure 4.5, the propeller-induced velocities decrease moving away from the propeller, resulting in a Gaussian distribution. The same distribution of the flow velocities at the bed has been also assumed in the Dutch method [53] for the estimation of the maximum velocities at the bed. In addition, the magnitude of the maximum velocity derived from our numerical implementation has been found to be between the values proposed by the German and the Dutch methods. In particular, the modelled maximum velocity on the seabed has resulted slighly smaller than the value suggested by the German method, which however tends to overestimate the bed velocities, but higher than the values recommended by the Dutch approach. Also, it occurres at a distance comparable to that indicated by Verheij for a propeller jet flow [72], equal to $h_p/x = 0.12 - 0.22$.

### 6.1.2 Morphological evolution of the bed: the steady vessel case

For the case of the steady vessel, the propeller-induced effect was clearly evident, especially if compared to the implementation without the propeller. Basically, the main difference is due to the flow field behind the ship generated by the propeller, responsible for modifying the bed shear stress and causing the bottom evolution. On the contrary, when the propeller is not implemented, no changes on the seabed occur.

Focusing on the top panel of Figure 4.7, it can be seen that the suspended load-induced bed evolution patterns fairly reflect the propeller-induced velocity of Figure 4.5. This is due to the fact that the bed evolution equation is evaluated from the sediment continuity equation, in which the time-averaged pickup and deposition rates are used. In particular, as indicated in Equation (4.16), the former term directly depends on the bed shear stress, related to the velocity through the friction coefficient.

In the middle panel of Figure 4.7 the bedload-induced effect is illustrated. Comparing this to the velocity field caused by the propeller on the bed, it can be noticed that the generation of the scour holes matches the velocities gradients. In fact, moving from the propeller downstream, the first scour hole, i.e. the secondary hole, is formed where the velocity behind the vessel increases from very low values (around zero) to 0.4 m/s. Another jump of about 0.4 m/s in the bottom velocities is found to be

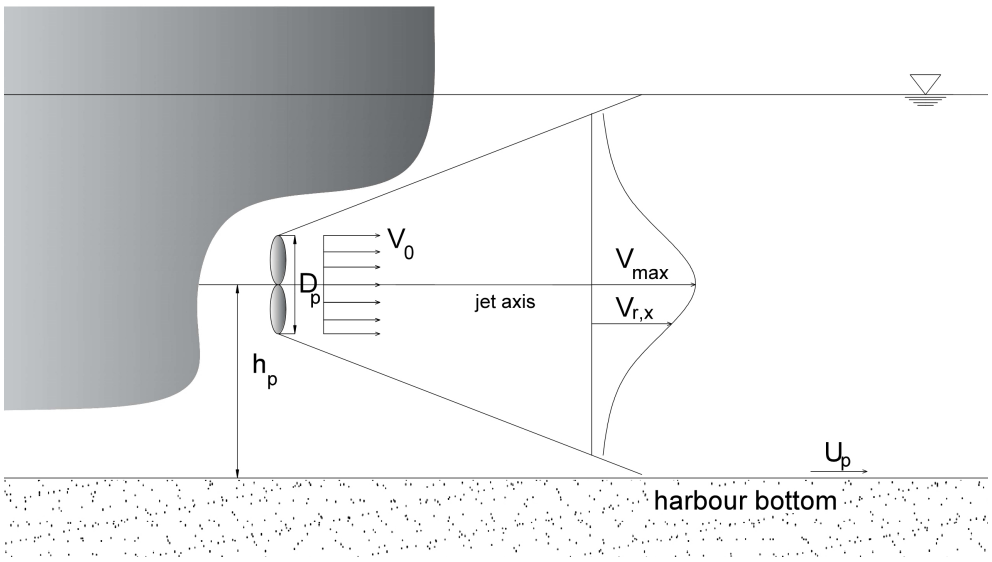


Figure 6.1: Typical scour profile due to a propeller jet.

close to the transition area between the zone of flow establishment and the zone of established flow. The velocities shift from 0.4 m/s in the ZFE to 0.7 m/s in the ZEF, originating the second and main scour hole. Such trend might be explained by the governing equation of the seabed morphological evolution, in which the bedload fluxes contribute through the gradient, as reported in Equation (4.21).

In the following, results are presented, also providing a qualitative comparisons to the main relevant literature findings to better understand the numerical model behaviour. However, it is important to remark that large differences exist between the model and the laboratory experiments (largely affected by scale issues), which can partially justify some of the discrepancies observed in the related results. Firstly, the majority of the laboratory experiments is characterized by a length scale of the order of centimeters, both for the propeller and the propeller gap. For the sediment beds, instead, the typical median grain size is of sand materials, with a wide range of order of millimeters, from 0.5 to a maximum of 10 mm. With regards to the velocities scale, like the efflux velocity and the revolution speed, the Froude scaling law is used. The number of revolutions assumed in the experiments is significantly higher than those practically used in reality. Refer, for example, to the works of [33] or [60]. As explained before, the ratios between these parameters are fundamental in determing the maximum scour depth, depending on the densimetric Froude number, the ratio between the propeller diameter and the sediment size and the ratio between the clearance and the sediment size. Our numerical runs, on the other hand, have been set up using the real geometrical and velocity scale, this resulting in $F_0$, $D_p/d_{50}$ and $h_p/d_{50}$ extremely different from the experiments.

The longitudinal profile of the bottom has been compared to the typical longitudinal profile due to a propeller jet shown in Figure 6.1.

Despite of the differences in the scale between the experiments and our numerical tests, we can state that the qualitative behaviour of the bottom is fairly well captured by the model. Referring to the bedload-induced seabed changes, in general, from the numerical runs it is possible to observe a minor scour hole in the area directly beneath the propeller, confirming a satisfactory consistency with what observed in many experimental tests, a.o. [33] [60]. On the contrary, while from the experiments the main scour starts to generate immediately downstream the secondary scour hole, following a rounded shape and reaching the maximum value at a distance from the propeller around $4D_p$, in the modelled streamwise section a plateau appears before the primary scour hole, exhibiting its peak in proximity of $3D_p$. Then, a deposion mound occurs in both the cases. From the laboratory experiments, a more peaked shape, with

a steeper slope can be noticed for the accumulation mound. From the modelled results, instead, the decay of the deposit is milder, resulting in a more elongated shape. This different trend could be explained by considering the sediment materials employed for the seabed in the two cases. In laboratory experiments, the sediment could not be scaled appropriately according to the scale of the propeller. As mentioned before, laboratory tests were conducted mainly in sandy environments, characterized by a ratio between the propeller and the sediment diameter varying from 50 to $10^3$ (see, for example, [60] or [33]). Conversely, the scale in the numerical test run in the present work is based on real values. Therefore, it is not possible to apply the same scaling factor in numerical and experimental tests, especially when scaling large propellers in the experiments. This clearly explains why, in the numerical tests, the ratio between the propeller and the sediment diameters is ten times larger that in the laboratory experiments. As a consequence, it is possible to state that the suspended load is negligible in the experiments, while has a huge impact in the numerical tests, due to the scaling effect. Referring to the work of [57], in case of silt materials, it was observed that the longitudinal profile is characterized by a deposit height much lower than that occured in sand, mainly due to water turbidity in the experiments with silt. Analyzing the temporal development of the scour profile, with reference to Figure 4.9 and Figure 4.11, it has been already observed that first generates the so-called primary scour hole, which grows with time until the end of the simulation, causing at the same time a deposition downstream. Then, also a secondary scour hole at the proximity of the propeller face occurs. A similar trend can also be recognized in Hong at al. [33]. In this work, through some experimental laboratory tests, the four stages of the scour evolution have been identified:

- the initial stage, in which the main scour hole is formed downstream the propeller, while no scour hole beneath the propeller occurs. A deposition mound is present downstream the main scour hole.
- the developing stage, in which the main scour hole increases in size. In addition, due to the entrainment of the fluid behind the propeller caused by the jet flow, also a small scour hole can be noticed directly beneath the propeller. The holes, however, remain separated.
- the stabilization stage, in which the growth of both the holes occurs.
- the asymptotic stage, during which the scour holes merged together. This stage is also referred as equilibrium stage, in which the maximum scour is reached.

In our model the equilibrium and the stabilization stages cannot be reached since the hydrodynamics has not been modified when implementing the propeller effects. However, the results from our numerical runs show significant similarities in the scour profile progress for the initial and the developing stages.

Figure 6.2 and Figure 6.3 show the longitudinal scour profiles for tests conducted respectively with different propeller speeds and different gaps from the propeller axis to the seabed. In Figure 6.2, the x and y axis represent respectively the horizontal distance (in m) and the dimensionless scour depth ($d_s/D_p$), for the test cases *Run0, Run1, Run2, Run3, Run4*.

Each revolution speed is indicated by the legend. It can be easily noticed that, given an offset height ratio $h_p/D_p$, smaller revolution speed corresponds to smaller scour depths and deposition as well, as also shown in the many other works, a.o. [60] (compare, for example, the cases 1 and 3) and [33]. Conversely, assumed the same revolution speed of 1.2 rev/s, Figure 6.3 shows the dependency of the nondimensional maximum scour depth, in y, on the offset height ratio, in x. As expected, the higher is the distance from the propeller axis to the seabed, the lower is the overall effect on the bathymetry. However, the reduction of the bed clearance seems to mainly increase the secondary scour hole, developing in the proximity of the propeller location. This tendency has been also observed in [33]. Referring to Figure 7 of Hong's work, the authors have shown the dimensionless scour profiles respectively for an offset ratio ($h_p/D_p$) equal to 0.5 and to 1 for different number of revolutions. The principle

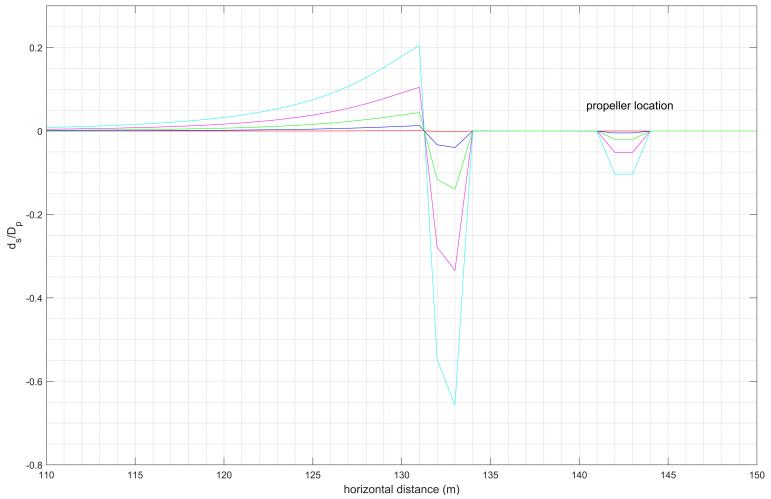


Figure 6.2: Longitudinal seabed profile due to the bedload for different revolutions number for the steady vessel case.

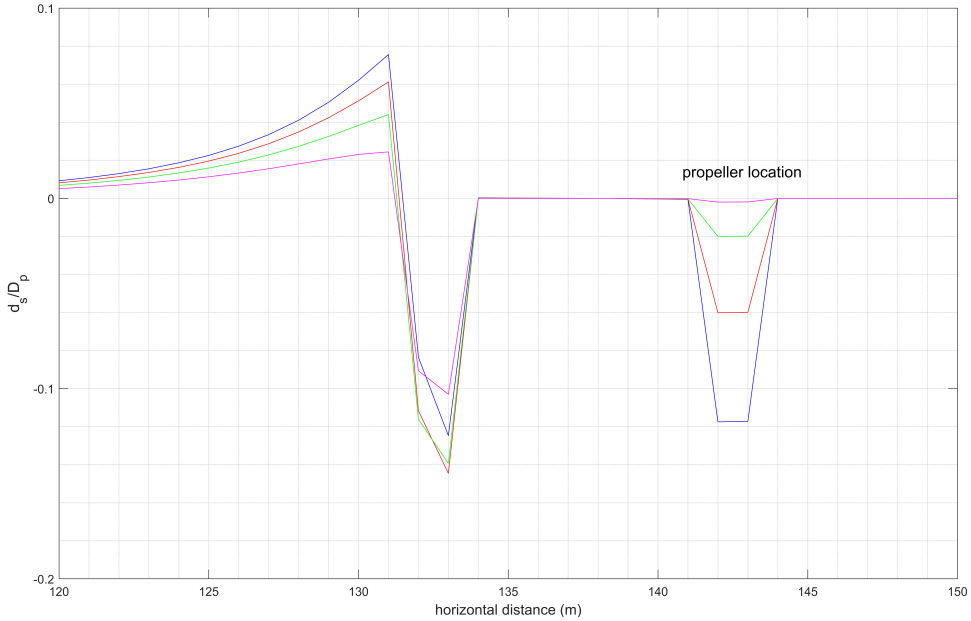


Figure 6.3: Longitudinal seabed profile due to the bedload for different bed clearances for the steady vessel case.

distinction is identified in the entity of the secondary scour depth. Comparing the values obtained, it can be seen that the adimensional scour depth of the secondary scour hole for $h_p/D_p = 0.5$ is almost double than that obtained for $h_p/D_p = 1$.

## 6.2 Discussion on the hydro-morphodynamics induced by the propeller: the moving vessel case

Similarly to the stationary cases, the same pattern of the seabed propeller-induced velocities has been found also for the moving ship. Slight differences in the magnitudes are mainly due to a lower value of $C_t$, depending this latter on the advance speed.

Fundamentally, the results have pointed out that the propeller jet effect on the bathymetry is considerably minor than the steady case, as already noticed by BAW [21]. However, the presence of the propeller can significantly increase the sediment transport, in particular in terms of concentration, since the propeller rotation tends to resuspend the sediments lying on the seabed, as shown in Figure 4.13. This has been confirmed comparing Figure 4.16, representing concentration without (top panel) and with (bottom panel) the propeller implementation. It is interesting to notice that, although the propeller can not increase the net sediment transport inside an harbour basin, it plays and important role in mobilizing and resuspending sediments. This effect might be stronger in case of fine and less compacted sediments. If characterized by low settling velocities, they tends to remain in suspension for longer periods, generating sediment plumes. In the middle panel, related to the bedload-induced morphological effects, a deposition is found at the beginning of the simulation: when the ship starts moving from the initial position, its speed suddenly increases from zero to a certain value. This, together with the rotation of the propeller, determines the generation of an accumulation behind the propeller, in red. The scour holes subsequently generated by the propeller along the channel can not be clearly identified because it is progressively balanced by the deposition occuring subsequently. Conversely, when the ship stops, the propeller continues digging until the end of the simulation, generating the last scour hole, depicted in blue in Figure 4.13.

## 6.3 Sensitivity analysis

As mentioned before, the model shows a plateau between the two scour holes, which, instead, is not present in the experimental tests. Therefore, several attempts have been made to improve the modelled longitudinal scour profile, modifying Equation (4.26) for the definition of the propeller-induced seabed velocity field. It might be useful to remember that the constant $c_p$ can be vary accordingly to the propeller type, in particular assumed equal to 0.17 for ducted propellers and equal to 0.19 for non-ducted propellers, like in the present case study. It is observed that slightly manipulating the formulation of the bottom velocity flow in the ZEF Equation (4.26)

$$U_p(x,y) = \begin{cases} V_0 \exp(-2\frac{y^2+{h_p}^2}{D_p^2}) & \text{in the ZFE where } x \leq \frac{D_p}{2c_{p1}} \\ V_0 \frac{1}{2c_{p1}} \frac{D_p}{x} \exp(-\frac{k_1}{2c_{p1}^2} \frac{y^2+{h_p}^2}{x^2}) & \text{in the ZEF where } x \geq \frac{D_p}{2c_{p1}} \end{cases} \tag{6.1}$$

Comparing Equation (4.26) (left panel) and Equation (6.3), it can be easily noticed that an additional constant, $k_1 = 16$, has been added in the exponential term.

Figure 6.4 shows the comparison between the streamwise view of the bedload-induced seabed evolution, obtained respectively by Equation (4.26), on the left panel, and Equation (6.3), on the right panel. In the x and y axis are respectively depicted the horizontal distance and the dimensionless scour depth.

In the right panel of Figure 6.4, it can be noticed that the qualitative representation of the scour profile seems more consistent with what has been observed in the experiments: the main scour hole occurs immediately downstream the secondary scour hole, developing beneath the propeller. Large differences in the magnitudes of the

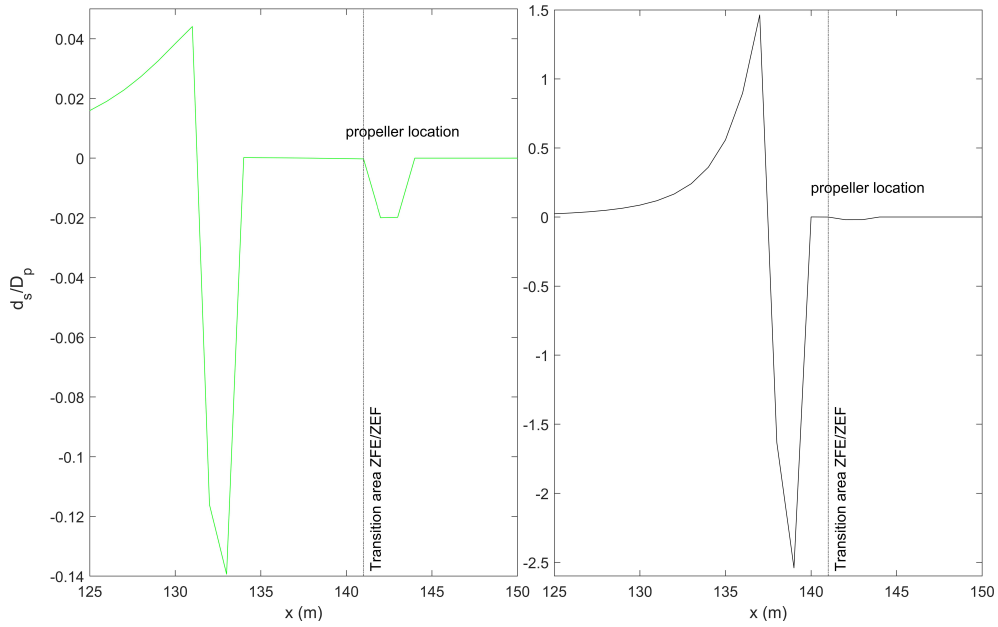


Figure 6.4: Longitudinal bed profile from equation (4.26) (left panel) and (6.3) (right panel) for the steady vessel case.

main scour holes and the deposition have been found between the two test cases, with values strongly higher in the right panel. Nonetheless, it is worth mentioning that this study constitutes the initial stage of the propeller implementation in the FUNWAVE model, during which it has been preferred to focus on the proper representation of the scour phenomenon, giving less importance to the values assumed by the scour holes and the deposition mound. Further investigations need to be conducted on all the other parameters involved in Equation (4.26) to modify the amplitude of the scour holes and for the quantitative calibration of the model.

## 6.4 Limitations and future works

First, it must be considered that FUNWAVE is a two-dimensional depth-averaged model. Therefore, it is not fully suitable to reproduce all the three-dimensional (3D) characteristics typically occurring during the scouring process induced by the ship propeller [52], although is able to capture the qualitative behaviour of the bottom, as shown by the results presented in Figures 6.2 and 6.3. Secondly, in this numerical implementation several assumptions have been made to simplify the modelling of the effect of the propeller jet flow using mathematical equations. Specifically, the choice of different equations for the estimation of the efflux velocity equation used in the model certainly affects the simulation results. The equation here, for instance, refers to a single propeller without a rudder or bow thruster and does not take into account the number of the blades. For sake of simplicity, we preferred not to include some propeller characteristics in the implementation, like the number of blades or the sense of rotation of the propeller, clockwise or counterclockwise (trivial in still water condition).

From the comparison of the numerical and the experimental tests, it has been detected that the main differences are found in the location, shape and magnitude of the morphological changes of the seabed, briefly discussed and analyzed in the following. A number of experimental tests [60], have confirmed that, at the equilibrium stage, the seabed longitudinal profile is characterized by the presence of two scour holes. A minor scour hole is found to evolve directly underneath the propeller, while the major one, also known as main or primary hole, generates and fully develops at a varying distance from the propeller according to multiple factors, such as the revolution speed, the clearance between the propeller and the seabed, the propeller

diameter and the median sediment size of the bed material. In general, it is possible to state that the numerical model proposed in this work fairly represents the secondary scour hole, in terms of position and also shape, although the not perfectly round shape (probably also due to the spatial discretization required by FUNWAVE). Referring to the magnitude, field data are not currently available to validate or better calibrate the model. With this aim, it must be noticed that the scale used in the laboratory tests is too small to be unaffected by scale issues, and be suitably compared with our numerical calculations run by FUNWAVE, which is a Boussinesq model mainly used in coastal applications, then suitable to represent large scales. Whilst it has be seen from the laboratory test that the main scour started developing directly downstream the secondary scour hole, our results have shown a plateau between these two areas. Moreover, in contrast to the experimental scour profile, the modelled profile displays a more peaked shape, then suddenly followed by the deposition mound. Regarding this latter, conversely, its decay is slower. This might be justified by the fact that the propeller-induced contribution to the sediment transport has been only included as an additional velocity field on the seabed, neglecting its contribution to the momentum equation. For a better representation of the propeller wash, the propeller contribution should be included in the hydrodynamic equations as an additional momentum flux, correspondingly to the propeller location. This additional contribution might be fix the discrepancy between the In addition, not only the morphodynamic, but also hydrodynamic computation should be affected by the propeller jet. Finally, another aspect to be improved in the future is the coupling of the hydrodynamics and the morphodynamics, although the effect on the latter might be negligible for the case of the steady vessel. To conclude, further numerical and experimental works will be fundamental to properly validate the present model.

## 6.5 Discussion on the combined impact of the sediment transport processes and the ship propellers

The La Spezia Arsenale is one the most important harbours of the Italian Navy, characterized by an intense ship traffic. Different investigations have proved that the ship traffic might induce a growth of the turbidity, due to the resuspension of a significant amount of fine materials from the seabed to the upper layers of the water column induced by ships propellers. The resuspended sediments could gradually tend to settle and accumulate, modifying the bathymetry and, in particular cases of low keel-bed clearance, reducing the navigational safety. Moreover, during the berthing/unberthing processes, i.e. when the ship speed gradually increases/decreases, the ship propeller could deeply affect the seabed, driving scour holes whose size depends on multiple factors, like the propeller revolution speed, the clearance between the hull and the seabed, the propeller diameter and the bed composition. On the other hand, from the first part of the present study, devoted to understand the hydro-morphodynamics of the area, numerical simulations have revealed that, unexpectedly, the freshwater discharges play a major role in governing the sediment transport processes, representing the main source of fine materials within the Arsenale. In fact, the LR and CR supply sediments within the basin, then mobilized by the wind forcing, according to its blowing direction. Accordingly, the deposition is found to be in proximity to the rivers' mouths. In light of the previous considerations, an important aspect to be addressed for the correct management and maintenance of the harbour in relation to the sediment transport processes, is the potential interaction between the rivers' and the traffic of the vessels and their combined impact within the Arsenale. While the former mainly contribute in supplying sediments inside basin, the ship traffic, i.e. the ship propellers, could affect the movement or displacement of the sediments, inducing their resuspension or redistribution in different areas. A promptly assessed investigation has been carried out to verify that the plumes from the LR and CR could be intersected by the main traffic routes traveled by the vessels moving towards the mooring quays withing the Arsenale. Figure 6.5 shows two typical routes of vessels entering the Arsenale. The typical route (306°) to reach the dry docks is given in green,

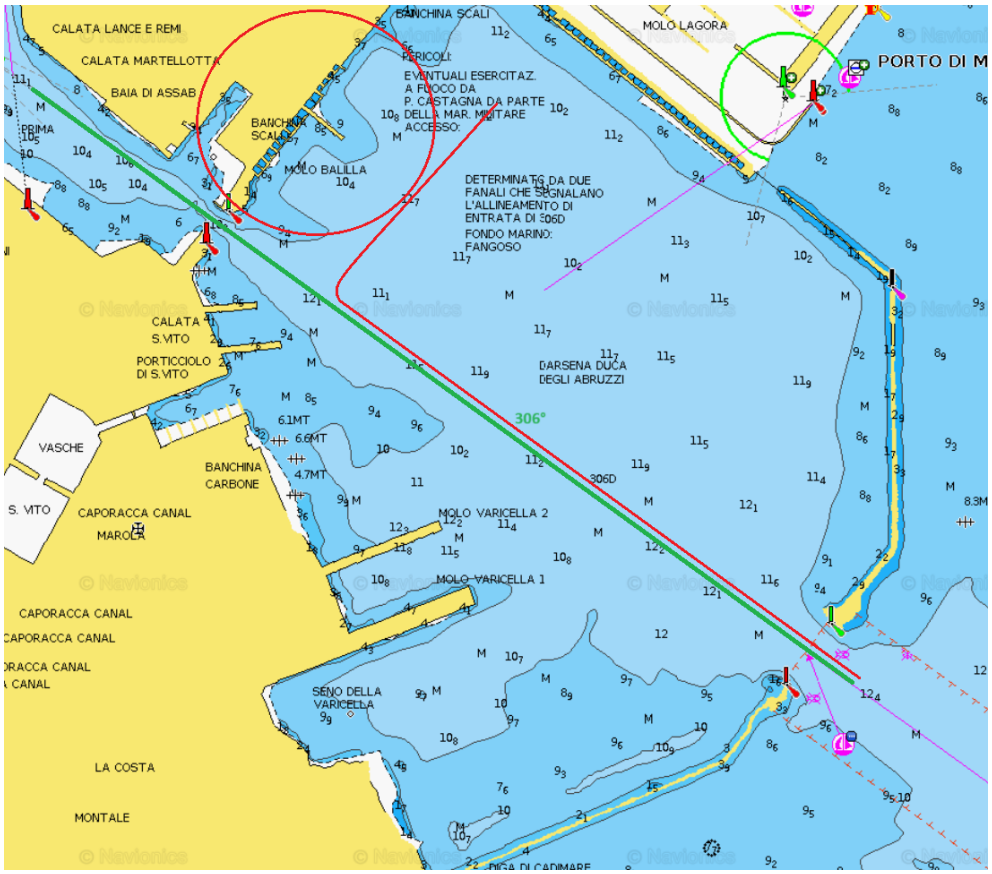


Figure 6.5: Potential interaction between the freshwater streams CR and LR and the typical vessels' routes inside the Arsenale.

while the red line and circle indicates respectively the route and the ship evolution to berth/unberth. In both cases, the vessel might interact with the CR stream and sediments, debouching in the west area of the basin. This simple analysis might be useful for optimizing the harbour management, for example regulating the marine traffic identifing the most suitable schedule and routing to minimize the generation of plumes and accumulation. Further numerical simulations, with the superposition of both these contributions, should be adequately run to quantitatively evaluate their consequences on the sediment transport mechanisms inside the Arsenale.

# Chapter 7

# Conclusions

## 7.1 Conclusion on the hydro-morphodynamics induced by natural forcings

We investigated the hydro-morphodynamic processes inside the Arsenale of La Spezia, one the most important military bases of the Italian Navy, by means of dedicated numerical simulations. The primary objective of this work was to assess how the physical processes evolving in the such an area, i.e., waves, tide, wind, and rivers' discharges, could affect the hydro-morphodynamics of the Arsenale. In view of the strategic importance of the site, the results of this work are also useful in evaluating the risk of harbour siltation, which reduces the appropriate depth of the navigation channels and could affect the required full operativity of the harbour.

FUNWAVE and Delft3D numerical models were used, respectively, to describe the wave propagation from offshore to the Arsenale and for the study of the internal circulation and the sediment transport. The FUNWAVE results showed that extreme waves, characterized by a 100-year return period, were strongly damped by the concurrent presence of coastal islands and the large breakwater at the entrance of the gulf. Both of them were effective in sheltering the harbour area. As a result, the maximum modelled wave height inside the Arsenale was approximately around 0.03 m. We then analysed three different scenarios to parametrically inspect the roles played by the different physical forcings, i.e., waves, the rivers' actions, and their concurrent role. All the cases were forced by the tide and the typical winds occurring in this area, from the NNE and SSE. The results revealed that the main forcing affecting the hydrodynamics inside the Arsenale was the wind, which generated some water surges in the northwestern or south-western areas of the Arsenale for the NNE or SSE winds, respectively. This contributed to the formation of a circulation cell, whose sense of rotation depended on the wind direction. The discharges of the LR and CR modified the wind-induced velocity. The CR, debouching directly in the Arsenale, helped to increase the wind-driven eddy. On the other hand, the mixing layer at the LR entrance, triggered by the difference in the velocities inside the Arsenale and the LR current, determined the generation of an eddy, whose evolution matched the increase in and decay of the freshwater discharge. Moreover, its development was enhanced by the flood tide, whereas it was retarded during the ebb phase. Hence, the tide modulated the velocity field forced by the wind. Instead, the short waves had a very modest influence on the hydrodynamics. In addition, this work enlighted that the morphodynamics were largely controlled by the freshwater streams, which were fundamental in supplying sediments to the Arsenale, while the waves and tide were not strong enough to resuspend the seabed sediments. As for the hydrodynamic circulation, the sediment transport was also affected by the wind forcing, resulting in different deposition patterns according to the wind blowing directions, NNE and SSE. Finally, the waves and the tide played a marginal role in both sediment transport and deposition.

In conclusion, it has been demonstrated that even when considering the combination of all the extreme forcings acting within the military basin, the Arsenale might not be

affected by significant siltation. Nonetheless, it has provided support in defining the basin areas more prone to sedimentation over a time scale of a storm. The accumulation of sediments can reduce the required water depth, affecting the port functionality. Consequently, periodic maintenance dredging must be planned in order to guarantee safe navigation. Considering the high cost of dredging, it might be preferable to find alternative solutions to prevent the entering of the sediments inside the harbour. In light of these considerations, some effective measures to reduce potential harbour siltation or, however, to mitigate the rivers' contribution in providing sediments in the Arsenale, are described in the following. Current deflecting walls (CWD) is one the most widespread means to minimise the sedimentation rate, especially when the density currents are not particularly strong. This consists of a vertical wall, supported in the middle by a sill and by piles at the edges, placed at the upstream corner of the harbour. In general, the use of CWD could alter the flow direction at the harbour entrance so that the transport of the sediments inside the harbour is reduced. By means of the sill at the base of the wall, the part of the water column highly laden with sediments would be deflected away from the harbour basin and towards the main watercourse, causing less suspended sediments to fill the basin. Moreover, it might contribute in reducing/weakening the circulation cell at the harbour entrance, consequently decreasing the sediment entrainment and deposition. Alternatively, sediment traps might represent a simpler and also effective tool to capture sediments. These are essentially pools, usually placed along waterways or rivers, which tend to significantly slow the flow, allowing the suspended fine material to be trapped and deposited at the bottom of the trap, retaining the sediments in the channel and preventing their immission in the harbour.

To the best of the authors' knowledge, the present study is one of the first to be specifically devoted to investigating the dynamics of flow and sediments in a unique semi-enclosed basin in an embayed, microtidal setting, and to also consider the role of freshwater streams. As embayed coastlines are rather common features in coastal microtidal contexts where marine actions (tide, waves) have moderate to low energy, the findings presented and discussed here may be applicable to harbours or sheltered coasts with similar environmental conditions.

A more complete characterization of the exchange processes between the basin and its surrounding features, moreover, can be achieved by considering the physical and chemical processes that were neglected here due to the lack of data on for example, salinity-driven currents and the related sedimentation processes.

## 7.2 Conclusion on the hydro-morphodynamics induced by anthropogenic forcings and future work

In the present work, the implementation of the propeller contribution in the Boussinesq numerical model FUNWAVE is presented and evaluated. The propeller-induced effect on the sediment transport has been implemented as a velocity field on the seabed, resulting in an additional contribution to the shear velocity and the consequent bed shear stress. The bottom velocity, computed in the ship-wake module, has been expressed as a function of the efflux velocity, inherently depending on the propeller characteristics, such as the revolution speed, the propeller diameter and thrust coefficient, and on geometrical parameters, as the radial distance from the propeller location and the clearance between the propeller axis and seabed. Numerical tests for a stationary and a moving vessel, have been carried out, varying some parameters to investigate the model behaviour.

Results have evidenced qualitative significant similarities to the literature findings, mainly in the development of the scour process and in the longitudinal profile, confirming the ability of the model to capture complex morphodynamics. More precisely, both the numerical and the experimental scour profiles, in fact, have evidenced the presence of two scour holes, followed by a deposition mound downstream. However, some adjustments need to be considered to improve the representation of the propeller wash in the model. First, an additional momentum flux due to the propeller wash

should be included in the hydrodynamic equations. In addition, the propeller jet should also affect the hydrodynamic computation, to be coupled with the morphodynamics. Hence, further numerical and experimental tests need to be performed to better calibrate and validate this present model, with the aim of providing a useful tool in predicting scour processes, crucial issues in the design process and management of ports, navigation channels and maritime structures. Additionally, it will help the authorities to evaluate multiple factors, as the potential impact of increased traffic on the seabed, the maximum draught of vessels entering the basin without causing severe consequences for its operativity. Moreover, it will be useful to plan aware dredging operations to prevent siltation issues. Further studies on local phenomena caused by anthropological factors, such as structural consolidation on the quays or vessel actions in low bed clearance conditions, in terms of propeller-induced scour, should be conducted to guarantee that the operativity of the basin is completely preserved.

# Appendix A

# Extreme event analysis

An extreme value analysis was conducted for the definition of the waves associated to a return period of 100 years. In the following, the main stages of the analysis are summarized and presented. For the statistical analysis, the so-called reanalyzed Copernicus Marine Service wave data, relating to the period 1993-2019, for the coordinate point 43.98° N, 9.85° E are used (see Figure 2.1).

## A.1 Detection of storm surges

First, the storm surges were defined as the events that exceeded a given threshold, chosen to be equal to $H_s = 0.5$ m. Among all these events, only the independent ones, i.e. spaced at least 12 hours apart, were selected. Of each event, the significant wave height $H_s$, the peak period $T_p$, and the peak direction $\theta_p$ were, then, considered for the analysis. In total, a number of 1.918 events were selected and, then, divided into the various directional sectors, of 30° each, as follows:

Table A.1: Storm surges in the La Spezia gulf from 1993-2019 for different directional sectors.

| ***Threshold*: $H_s > 0.5m$** | |
|---|---|
| **Sector** | **Number of events** |
| 0°-30° | 17 |
| 30°-60° | 78 |
| 60°-90° | 49 |
| 90°-120° | 34 |
| 120°-150° | 82 |
| 150°-180° | 265 |
| 180°-210° | 201 |
| 210°-240° | 1033 |
| 240°-270° | 137 |
| 270°-300° | 9 |
| 300°-330° | 4 |
| 330°-360° | 9 |

It was observed that the principle sector was that between 210° N and 240° N. To define the extreme events, the sectors for which the highest number of storm surges occurs were analyzed, namely 150°-180°, 180°-210°, 210°-240°, 240°-270°.

## A.2 Detection of the extreme events

For each sector, the events with significant wave height larger than 2 m have been identified. Then it has been verified that these events were equally distributed over all the years of the analysis. Note that, for example, from the 240°-270° sector, only 12 events exceeded the 2 m threshold, resulting in some years characterized by zero events. Therefore, this sector has been discarded. For the other three sectors, the analysis led to the following values:

Table A.2: Number of extreme events in the La Spezia gulf from 1993-2019 for different directional sectors.

| **Extreme events $H_s$>2m** | | |
|---|---|---|
| **150°-180°** | **180°-210°** | **210°-240°** |
| 50 | 32 | 291 |

## A.3 Gumbel and Weibull distributions

To perform the statistical analysis and to define the truncated series for the main three directional sectors mentioned before, the most common distributions are those proposed by Gumbel [26] and Weibull [74]. In both cases, the distribution parameters were calculated with the least squares method. For the Weibull distribution, we performed the analysis, varying the third parameter from time to time. Finally, the distribution that best suited the data was selected, as shown below:

| Directional sector: Weibull (k=1) | 150°-180° RMSE = 0.9924 |
|---|---|
| $T_R$ | $H$ |
| 10 | 3.84 |
| 20 | 4.29 |
| 50 | 4.89 |
| 100 | 5.34 |
| 150 | 5.60 |

| Direction sector Weibull (k=2) | 210°-240° RMSE = 0.9912 |
|---|---|
| $T_R$ | $H$ |
| 10 | 5.71 |
| 20 | 6.10 |
| 50 | 6.58 |
| 100 | 6.93 |
| 150 | 7.12 |

| Direction sector: Gumbell | 180°-210° RMSE = 0.9574 |
|---|---|
| $T_R$ | $H$ |
| 10 | 4.29 |
| 20 | 4.95 |
| 50 | 5.80 |
| 100 | 6.45 |
| 150 | 6.83 |

Table A.3: Statistical analysis results

## A.4 Determination of $T_p$ associated to $H_s$

Also in this case, a data truncation threshold was used. Similarly to the definition of the significant wave height, also for the peak period a threshold of 2 m was used to define the storm surges. To relate the wave significant height to the the peak period, the following relation was used:

$$T_p = a\sqrt{H_s} \tag{A.1}$$

By fitting the data with Equation (A.4), it was obtained:

| | |
|---|---|
| Sector 150°-180° | $T_p = 4.196\sqrt{H_s}$ |
| Sector 180°-210° | $T_p = 3.858\sqrt{H_s}$ |
| Sector 210°-240° | $T_p = 4.989\sqrt{H_s}$ |

# Bibliography


[1] Coastal Engineering Research Center (US). *Shore protection manual*. Vol. 1. Department of the Army, Waterways Experiment Station, Corps of Engineers . . ., 1984.

[2] ML Albertson et al. "Diffusion of submerged jets". In: *Transactions of the American Society of Civil Engineers* 115.1 (1950), pp. 639–664.

[3] W Berger et al. "Courant provoque par les bateaux protection des berges et solution pour eviter l'erosion du lit du haut rhin". In: *PIANC, 25th Congress, Section I-1. Edinburgh*. 1981.

[4] HG Blaauw and EJ van de Kaa. "Erosion of bottom and sloping banks caused by the screw race of manoeuvring ships. Publ. no. 202, Delft Hydraulics Laboratory, The Netherlands". In: (1978).

[5] R Booij. "Metingen van uitwisselingen tussen rivier en haven". In: *Rapport 9-86 voor Gemeentewerken Rotterdam.* (1986).

[6] Silvia Bosa, Marco Petti, and Sara Pascolo. "Improvement in the sediment management of a lagoon harbor: The case of Marano lagunare, Italy". In: *Water* 13.21 (2021), p. 3074. DOI: https://doi.org/10.3390/w13213074.

[7] M Brocchini. "An analytical description of the energy balance in turbulent, round, free jets". In: *AIP Advances* 10.7 (2020).

[8] Maurizio Brocchini. "A reasoned overview on Boussinesq-type models: the interplay between physics, mathematics and numerics". In: *Proceedings of the Royal Society A: Mathematical, Physical and Engineering Sciences* 469.2160 (2013), p. 20130496.

[9] Zhixian Cao. "Equilibrium near-bed concentration of suspended sediment". In: *Journal of Hydraulic Engineering* 125.12 (1999), pp. 1270–1278.

[10] Luca Carniello, Andrea Defina, and Luigi D'Alpaos. "Modeling sand-mud transport induced by tidal currents and wind waves in shallow microtidal basins: Application to the Venice Lagoon (Italy)". In: *Estuarine, Coastal and Shelf Science* 102 (2012), pp. 105–115. DOI: https://doi.org/10.1016/j.ecss.2012.03.016.

[11] Giuseppe Curulli, Nadia Penna, and Roberto Gaudio. "Improved formulation for the geometric characteristics of the scour hole and deposition mound caused by a rotating propeller jet on a mobile bed". In: *Ocean Engineering* 267 (2023), p. 113175.

[12] Andrea D'Alpaos, Luca Carniello, and Andrea Rinaldo. "Statistical mechanics of wind wave-induced erosion in shallow tidal basins: Inferences from the Venice Lagoon". In: *Geophysical Research Letters* 40.13 (2013), pp. 3402–3407. DOI: https://doi.org/10.1002/grl.50666.

[13] Erik D De Goede. "Historical overview of 2D and 3D hydrodynamic modelling of shallow water flows in the Netherlands". In: *Ocean Dynamics* 70.4 (2020), pp. 521–539. DOI: https://doi.org/10.1007/s10236-019-01336-5.

[14] Mauro De Marchis, Gabriele Freni, and Enrico Napoli. "Three-dimensional numerical simulations on wind-and tide-induced currents: The case of Augusta Harbour (Italy)". In: *Computers & geosciences* 72 (2014), pp. 65–75. DOI: https://doi.org/10.1016/j.cageo.2014.07.003.

[15] Deltares. *Delft3D-Flow. Simulation of multi-dimensional hydrodynamic flows and transport phenomena, including sediments. User Manual*. 2022.

[16] Deltares. *Delft3D-Wave. Simulation of short-crested waves with SWAN. User Manual*. 2023.

[17] Consorzio Intecno - DHI. *Studi di Idrodinamica nel Golfo di La Spezia - Studio idrodinamico e dei processi diffusivi e dispersivi nello specchio acqueo interno al Golgo di La Spezia*. Tech. rep. DHI and Intecno, 2015. DOI: `https://va.mite.gov.it/File/Documento/139154`.

[18] JW104430 Elder. "The dispersion of marked fluid in turbulent shear flow". In: *Journal of fluid mechanics* 5.4 (1959), pp. 544–560.

[19] RC Ertekin, WC Webster, and JV Wehausen. "Waves caused by a moving disturbance in a shallow channel of finite width". In: *Journal of Fluid Mechanics* 169 (1986), pp. 275–292.

[20] M Fuehrer, H Pohl, and K Romisch. "Propeller jet erosion and stability criteria for bottom protection of various constructions". In: *Bulletin of the Permanent International Association of Navigation Congresses [PIANC]* 58 (1987).

[21] Bundesanstalt für Wasserbau. "Principles for the design of bank and bottom protection for inland waterways (GBB)". In: *BAW Codes of Practice and Guidelines* (2010).

[22] G Galappatti and CB Vreugdenhil. "A depth-integrated model for suspended sediment transport". In: *Journal of Hydraulic Research* 23.4 (1985), pp. 359–377.

[23] Kathleen A Garland. "The San Jacinto River Waste Pits superfund site: An assessment of remedial options for sites with dioxin-contaminated sediments with implications for remedy selection at the San Jacinto Site". In: *Texans together* (2015).

[24] Wei-Bing Guan, Eric Wolanski, and Li-Xian Dong. "Cohesive sediment transport in the Jiaojiang River estuary, China". In: *Estuarine, Coastal and Shelf Science* 46.6 (1998), pp. 861–871. DOI: `https://doi.org/10.1006/ecss.1998.0336`.

[25] Antonio Guarnieri et al. "Effects of marine traffic on sediment erosion and accumulation in ports: a new model-based methodology". In: *Ocean Science* 17.2 (2021), pp. 411–430.

[26] Emil Julius Gumbel. *Statistics of extremes*. Columbia university press, 1958.

[27] Gerard Hamill, Charmaine Kee, and Dona Ryan. "Three-dimension efflux velocity characteristics of marine propeller jets". In: *Proceedings of the Institution of Civil Engineers-Maritime Engineering*. Vol. 168. 2. Thomas Telford Ltd. 2015, pp. 62–75.

[28] Gerard Alphonsus Hamill. "Characteristics of the screw wash of a manoeuvring ship and the resulting bed scour." In: (1989).

[29] E Allen Hammack et al. *Three-dimensional Numerical Model Study of Flow Near a Scour Hole in Isle of Wight Bay Near Ocean City, Maryland*. US Army Engineer Research, Development Center, Coastal, and Hydraulics . . ., 2022.

[30] Hashim Nisar Hashmi. "Erosion of a granular bed at a quay wall by a ship's screw wash." In: (1995).

[31] Klaus Hasselmann et al. "Measurements of wind-wave growth and swell decay during the Joint North Sea Wave Project (JONSWAP)." In: *Ergaenzungsheft zur Deutschen Hydrographischen Zeitschrift, Reihe A* (1973).

[32] MG Hawkswood et al. "Propeller Action and Berth Scour Protection". In: *PIANC-COPEDEC IX, Rio de Janeiro, Brasil* (2016).

[33] Jian-Hao Hong, Yee-Meng Chiew, and Nian-Sheng Cheng. "Scour caused by a propeller jet". In: *Journal of Hydraulic Engineering* 139.9 (2013), pp. 1003–1012.

[34] James T Kirby et al. "FUNWAVE 1.0: fully nonlinear Boussinesq wave model-Documentation and user's manual". In: *research report NO. CACR-98-06* (1998).

[35] G. Korres, M. Ravdas, and A. Zacharioudaki. "Mediterranean sea waves analysis and forecast (CMEMS MED-Waves)". In: (2019). DOI: https://doi.org/10.25423/CMCC/MEDSEA_ANALYSIS_FORECAST_WAV_006_017.

[36] W-H Lam et al. "A review of the equations used to predict the velocity distribution within a ship's propeller jet". In: *Ocean Engineering* 38.1 (2011), pp. 1–10.

[37] WH Lam et al. "An effective method for comparing the turbulence intensity from LDA measurements and CFD predictions within a ship propeller jet". In: *Ocean engineering* 52 (2012), pp. 105–124.

[38] EJ Langendoen, C Kranenburg, and R Booij. "Flow patterns and exchange of matter in tidal harbours". In: *Journal of Hydraulic Research* 32.2 (1994), pp. 259–270. DOI: https://doi.org/10.1080/00221686.1994.10750040.

[39] G.R. Lesser et al. "Development and validation of a three-dimensional morphological model". In: *Coastal engineering* 51.8-9 (2004), pp. 883–915. DOI: https://doi.org/10.1016/j.coastaleng.2004.07.014.

[40] Vincent Leys. "3D flow and sediment transport modelling at the reversing falls-Saint John Harbour, New Brunswick". In: *OCEANS 2007*. IEEE. 2007, pp. 1–16. DOI: https://doi.org/10.1109/OCEANS.2007.4449139.

[41] Oliver Lojek, Nils Goseberg, and Torsten Schlurmann. "Projecting Hydro-Morphodynamic Impacts of Planned Layout Changes for a Coastal Harbor". In: *Journal of Waterway, Port, Coastal, and Ocean Engineering* 147.6 (2021), p. 05021013. DOI: https://doi.org/10.1061/(ASCE)WW.1943-5460.0000666.

[42] José Fortes Lopes, João Miguel Dias, and Ivan Dekeyser. "Numerical modelling of cohesive sediments transport in the Ria de Aveiro lagoon, Portugal". In: *Journal of Hydrology* 319.1-4 (2006), pp. 176–198. DOI: https://doi.org/10.1016/j.jhydrol.2005.07.019.

[43] Ulrik Lumborg and Morten Pejrup. "Modelling of cohesive sediment transport in a tidal lagoon—An annual budget". In: *Marine Geology* 218.1-4 (2005), pp. 1–16. DOI: https://doi.org/10.1016/j.margeo.2005.03.015.

[44] Ayyuob Mahmoodi et al. "Study of current-and wave-induced sediment transport in the Nowshahr Port entrance channel by using numerical modeling and field measurements". In: *Journal of Marine Science and Engineering* 8.4 (2020), p. 284. DOI: https://doi.org/10.3390/jmse8040284.

[45] Matt Malej and Fengyan Shi. "Suppressing the pressure-source instability in modeling deep-draft vessels with low under-keel clearance in FUNWAVE-TVD". In: (2021).

[46] UDF Manual. "ANSYS FLUENT 12.0". In: *Theory Guide* (2009), p. 67.

[47] Stephen T Maynord. "Physical forces near commercial tows". In: (2000).

[48] Eugen Meyer-Peter and Robert Müller. "Formulas for bed-load transport". In: *IAHSR 2nd meeting, Stockholm, appendix 2*. IAHR. 1948.

[49] E Isaie Moghaddam et al. "Wave-induced currents in the northern Gulf of Oman: a numerical study for Ramin Port along the Iranian coast". In: *American Journal of Fluid Dynamics* 8.1 (2018), pp. 30–39. DOI: https://doi.org/10.5923/j.ajfd.20180801.04.

[50] Anna Mujal Colilles et al. "Ship manoeuvring effects on propeller induced erosion". In: (2018).

[51] E. Partheniades. "Erosion and deposition of cohesive soils". In: *Journal of the Hydraulics Division* 91.1 (1965), pp. 105–139. DOI: https://doi.org/10.1061/JYCEAJ.0001165.

[52] Nadia Penna et al. "Three-dimensional analysis of local scouring induced by a rotating ship propeller". In: *Ocean Engineering* 188 (2019), p. 106294.

[53] PIANC. "Guidelines for protecting berthing structures from scour caused by ships". In: *Marcom Rep. 180* (2015).

[54] N Rajaratnam. "Erosion by plane turbulent jets". In: *Journal of hydraulic Research* 19.4 (1981), pp. 339–358.

[55] Hydrodata S.p.A. *Studio Idrologico e Idraulico per la Definizione delle Fasce di Esondazione dei Principali Torrenti, Fossi e Canali Ricadenti nel Comune della Spezia*. Tech. rep. Hydrodata S.p.A., 2021.

[56] Biochemie Lab S.r.L., PH S.r.L., and Polaris S.r.L. *Intervento di Caratterizzazione Ambientale dei fondali presso Specchi Acquei in uso alla Marina Militare di La Spezia*. Tech. rep. Biochemie Lab S.r.L., Polaris S.r.L. and PH S.r.L., 2002.

[57] Cansu Schmunk, Mustafa Dogan, and Selim Altun. "Predicting propeller jet scour in silty and sandy marine environments". In: *Ocean Engineering* 286 (2023), p. 115558.

[58] Fengyan Shi et al. "FUNWAVE-TVD Fully Nonlinear Boussinesq Wave Model with TVD Solver Documentation and User's Manual". In: *Center Appl. Coastal Res., Univ. Delaware, Newark, DE, USA, Res. Rep. No CACR-11-04* 2 (2011), p. 1.

[59] Richard P Signell and Bradford Butman. "Modeling tidal exchange and dispersion in Boston Harbor". In: *Journal of Geophysical Research: Oceans* 97.C10 (1992), pp. 15591–15606.

[60] Remziye Ilayda Tan and Yalçın Yüksel. "Seabed scour induced by a propeller jet". In: *Ocean Engineering* 160 (2018), pp. 132–142.

[61] Nicholas S Tavouktsoglou et al. "Application of two phase Eulerian CFD model to simulate high velocity jet induced scour". In: *International Conference on Offshore Mechanics and Arctic Engineering*. Vol. 84409. American Society of Mechanical Engineers. 2020, V008T08A003.

[62] Tomas Torsvik, Geir Pedersen, and Kristian Dysthe. "Waves generated by a pressure disturbance moving in a channel with a variable cross-sectional topography". In: *Journal of waterway, port, coastal, and ocean engineering* 135.3 (2009), pp. 120–123.

[63] Mick van der Wegen. *Modeling morphodynamic evolution in alluvial estuaries*. CRC Press, 2010.

[64] WPA Van Lammeren, JD van van Manen, and MWC Oosterveld. "The Wageningen B-screw series". In: (1969).

[65] LC Van Rijn. *Harbour siltation and control measures*. 2016.

[66] Leo C Van Rijn. "Sediment pick-up functions". In: *Journal of Hydraulic engineering* 110.10 (1984), pp. 1494–1502.

[67] Leo C Van Rijn, JA Roelvink, and W ter Horst. "Approximation formulae for sand transport by currents and waves and implementation in DELFT-MOR". In: *Z3054* (2001).

[68] Simone AH Van Schijndel and C Kranenburg. "Reducing the siltation of a river harbour". In: *Journal of Hydraulic Research* 36.5 (1998), pp. 803–814. DOI: https://doi.org/10.1080/00221689809498604.

[69] L.C. van Rijn et al. *Principles of sediment transport in rivers, estuaries and coastal seas*. Aqua publications Amsterdam, 1993.

[70] L.C. van Rijn et al. "The predictability of cross-shore bed evolution of sandy beaches at the time scale of storms and seasons using process-based profile models". In: *Coastal Engineering* 47.3 (2003), pp. 295–327. DOI: https://doi.org/10.1016/S0378-3839(02)00120-5.

[71] Leo C van Rijn. "Literature review of critical bed-shear stresses for mud-sand mixtures". In: *Technical Note. www. leovanrijn-sediment. com* (2020).

[72] H Verhey. "The stability of bottom and banks subjected to the velocities in the propeller jet behind ships". In: *International harbour congress, 8th*. 1983.

[73] Pei-Fang Wang et al. "Evaluation of resuspension from propeller wash in DoD harbors". In: *Project ER-201031* (2016), p. 325.

[74] Waloddi Weibull. “A statistical distribution function of wide applicability”. In: *Journal of applied mechanics* (1951).

[75] JC Winterwerp. “Reducing harbor siltation. I: Methodology”. In: *Journal of waterway, port, coastal, and ocean engineering* 131.6 (2005), pp. 258–266. DOI: https://doi.org/10.1061/(ASCE)0733-950X(2005)131:6(258).

[76] T Yao-Tsu Wu. “Generation of upstream advancing solitons by moving disturbances”. In: *Journal of fluid mechanics* 184 (1987), pp. 75–99.

[77] S Zecchetto, G Umgiesser, and M Brocchini. “Hindcast of a storm surge induced by local real wind fields in the Venice Lagoon”. In: *Continental Shelf Research* 17.12 (1997), pp. 1513–1538.